



Karlsruhe Institute of Technology  
Faculty for Mechanical Engineering  
Institute for Thermal Turbomachines

Siemens AG  
Power and Gas Division  
Large Gas Turbines, Generators  
Combustion

KARLSRUHE INSTITUTE OF TECHNOLOGY

MASTER THESIS

---

# Evaluation of StarCCM+ to predict Thermoacoustic Instabilities using Large Eddy Simulation

---

*Author:*

Thomas Indlekofer

*Supervisor:*

Dipl.-Ing. Behdad Ariatabar

ITS

Prof. Dr.-Ing. Hans-Jörg Bauer

ITS

Dr.-Ing. Sebastian Hermeth

Siemens AG

Faculty for Mechanical Engineering

October 12, 2017

# *Abstract*

## **Evaluation of STARCCM+ to predict Thermoacoustic Instabilities using Large Eddy Simulation**

Self-sustained pressure and heat-release oscillations yielded by thermoacoustic coupling are a major problem of gas turbine operation and methods to predict them are needed. This work investigates the capabilities of Large Eddy Simulation (LES) in StarCCM+ to predict these instabilities in the academic Volvo bluff-body combustor. First, simplified cases are studied to assess boundary condition treatment and numerical accuracy of the methods available. The non-reactive operating point is predicted accurately, showing good agreement for velocity fields as well as the ability to predict the vortex shedding frequency in the intrinsically unsteady region of the recirculation zone. For a reacting-stable operating point the acceleration downstream of the bluff body is overpredicted and the flow fields are not predicted accurately. Low frequency oscillations of the unstable operating points are evidenced coinciding with experimental results and an acoustic analysis based on Comsol Multiphysics. Up to  $\phi = 1.0$  the coherence of the equivalence ratio and the magnitude of the instabilities is predicted qualitatively.

## **Evaluación de StarCCM+ para predecir inestabilidades termo acústicas usando Large Eddy Simulation**

Las oscilaciones de presión y de liberación de calor auto excitados producida por el acoplamiento termo acústico son problemas importantes en la operación de turbina de gas y métodos para predecirlas son necesarios. Este trabajo investiga las capacidades de Large Eddy Simulation (LES) en StarCCM + para predecir estas inestabilidades en la cámara de combustión académica de Volvo Flygmotor. En primer lugar, se estudian los casos simplificados para evaluar el tratamiento de las condiciones límite y la precisión numérica de los métodos disponibles. El punto de funcionamiento no reactivo se predice con precisión, mostrando un buen ajuste para los campos de velocidad, así como la capacidad de predecir la frecuencia de desprendimiento de vórtices en la región intrínsecamente inestable de la zona de recirculación. Para un punto de operación estable en reacción, la aceleración corriente abajo del cuerpo del bluff está sobre predispuesta y los campos de flujo no se predicen con precisión. Las oscilaciones de baja frecuencia de los puntos de funcionamiento inestables se evidencian coincidiendo con resultados experimentales y un análisis acústico basado en Comsol Multiphysics. Hasta  $\phi = 1.0$  la coherencia de la relación de equivalencia y la magnitud de las inestabilidades se predice cualitativamente.

## Declaration of Authorship

Ich, Thomas Indlekofer, erkläre hiermit an Eides statt, dass ich die vorstehende Masterthesis selbstständig angefertigt und die benutzten Hilfsmittel, Quellen sowie die befragten Personen und Institutionen vollständig angegeben habe. Darüber hinaus versichere ich, dass ich die Regeln zur Sicherung guter wissenschaftlicher Praxis im Karlsruher Institut für Technologie (KIT) in der gültigen Fassung beachtet habe.

Signed:

---

Date:

---





## *Acknowledgements*

This thesis represents the final piece of my Master studies at the Karlsruhe Institute of Technology. The work was done at the Institute for Thermal Turbomachines in cooperation with Siemens AG in Berlin.

I would like to thank Prof. Bauer for giving me the possibility to write this thesis at the ITS. In particular, I would like to thank Dipl.-Ing Behdad Ariatabar for the supervision and the valuable input during this work.

Thanks to Dr. Nakul Prasad who recruited me as an intern at Siemens October 2016, but unfortunately left our department shortly afterwards. I hope it wasn't me who forced you to flee from CFD.

Thereby the burden of my supervision had to be carried by Dr. Sebastian Hermeth, who was always available if I needed any support. Same goes for Dr. Lukasz Panek. Thanks to the both of you for never-ending help, guidance, knowledge and especially for spending countless lunch breaks with 12s, 15s, M1s&2s + extra rice. Even though we never made it to the fish shop, the time here was the best I had foodwise so far. It sounds weird to say that you expanded my horizons, however, I probably would not follow the path towards Norway without your support.

I also want to thank the whole team of PG GT EN LGT SC COMB MFEU for the nice atmosphere in the office. You made the working time really enjoyable.

Thanks to all the friends and my family who accompanied me during my studies,

Thomas Indlekofer

Berlin 2017

# Contents

<b>Declaration of Authorship</b>	<b>iii</b>
<b>Acknowledgements</b>	<b>v</b>
<b>I Introduction and Theoretical Background</b>	<b>1</b>
<b>1 Introduction and Context</b>	<b>3</b>
1.1 Motivation . . . . .	3
Objective of this thesis . . . . .	4
1.2 Introduction . . . . .	5
1.2.1 Combustion Instabilities . . . . .	5
1.2.2 Driving Mechanisms for Combustion Instabilities . . . . .	7
1.2.3 Damping Mechanisms for Combustion Instabilities . . . . .	8
1.3 Approaches to study combustion instabilities . . . . .	9
<b>2 Theoretical Background</b>	<b>11</b>
2.1 Computational Fluid Dynamics . . . . .	11
2.1.1 Governing Equations of Fluid Mechanics . . . . .	11
2.1.2 Approaches to compute turbulent flows . . . . .	13
2.1.3 Species Transport and Reacting Flow . . . . .	16
2.1.4 Solution Methods . . . . .	19
Discretization . . . . .	20
Spatial Discretization . . . . .	20
Temporal Discretization . . . . .	21
Pressure-Velocity Coupling . . . . .	21
2.1.5 Boundary Conditions . . . . .	24
2.1.6 Numerical modeling errors . . . . .	24
2.2 3D Helmholtz Methods . . . . .	25
2.3 Postprocessing . . . . .	26
2.3.1 Two-microphone Method . . . . .	26
<b>II Assessment of Numerical Accuracy and Boundary Conditions</b>	<b>29</b>
<b>3 Vortex Preservation</b>	<b>33</b>

3.1	Case Description	33
3.2	Numerical Accuracy	34
3.2.1	Numerical accuracy in comparison to other codes	37
3.3	Computational Time	38
<b>4</b>	<b>Acoustic Wave Propagation</b>	<b>41</b>
4.1	Case Description	41
4.2	Numerical Accuracy	42
4.3	Computational Time	44
4.4	Boundary Condition Treatment	44
4.5	Two-microphone method	46
<b>5</b>	<b>Performance</b>	<b>49</b>
<b>6</b>	<b>Conclusion of the test cases</b>	<b>51</b>
<b>III</b>	<b>The Volvo Validation Rig</b>	<b>53</b>
<b>7</b>	<b>Introduction</b>	<b>55</b>
7.1	Experimental Setup	55
7.2	Literature Review	57
<b>8</b>	<b>Reynolds-Averaged Simulations</b>	<b>63</b>
8.1	Numerical Settings	63
8.2	Coldflow Results	67
8.3	Reacting Stable Results	68
8.4	Conclusion of the RANS approach	72
<b>9</b>	<b>Acoustic Analysis with Comsol Multiphysics</b>	<b>73</b>
9.1	Settings	73
9.2	Chamber modes derived by Comsol Multiphysics	73
<b>10</b>	<b>Large Eddy Simulations</b>	<b>77</b>
10.1	Numerical Settings	77
10.2	Analysis of the non reacting operating point C	81
10.2.1	Settings and Mesh Validation	81
10.2.2	Averaged cold flow fields	81
10.2.3	Unsteady flow field	83
10.3	Analysis of the reacting flow at low inlet velocity (Buzz mode)	85
10.3.1	Settings and Mesh Validation	85
10.3.2	Influence of boundary condition treatment	86
10.3.3	Averaged reacting flow fields	88
10.3.4	Dynamic behaviour for varying equivalence ratios	92
10.4	Analysis of the reacting flow at high inlet velocity (Screech mode)	96

10.4.1 Numerical Settings . . . . .	96
10.4.2 Dynamical behaviour for varying equivalence ratios . . . . .	97
10.4.3 Scalability of StarCCM+ on JURECA . . . . .	97
<b>11 Conclusion and Outlook</b>	<b>99</b>
11.1 Conclusion . . . . .	99
11.2 Outlook . . . . .	100
<b>Bibliography</b>	<b>101</b>

# List of Figures

1.1	Estimated shares of GHG emissions by sector [Age17]	3
1.2	Rijke Tube [Rij59]	5
1.3	Circumstances enabling the occurrence of combustion instabilities	6
1.4	Growing combustion instability that leads a limit cycle [PV05]	7
1.5	Feedback loop for a confined combustor	8
1.6	Possibilities to study thermoacoustic instabilities [Gha15]	9
2.1	Comparison of RANS, LES and DNS simulations [PV05]	13
2.2	Solution procedure for the PISO (Red) and the SIMPLE algorithm (Blue)	23
2.3	Visualization of discretization errors due to numerical dissipation (a) and numerical dispersion (b). Dashed Line: Original signal. Solid line: Convected signal [Toe17]	25
2.4	Schematic of the setup for the two-microphone test	27
3.1	Computational domain of the vortex preservation test (left) and the initialized vortex (right) displayed as $u - u_0$	33
3.2	a) - f): Contour plots for different settings of $u - u_0$ for the initial flow field and after 1, 3, 5 and 10 flow through times. Notation: Algorithm - Spatial Discretization - Temporal Discretization	36
3.3	Velocity $v$ of the exact result (blue), the PISO algorithm (red) and the Unsteady Implicit algorithm (black) for $y = 0$ after 1, 3, 5, 10 flow through times. The order specifies the spatial discretization, the parenthesis the time levels of the BWD scheme	37
3.4	Velocity $v$ of the exact result (blue), the Unsteady Implicit algorithm in StarCCM+ (black), Open Foam (magenta), AVBP (red dashed) and YALES (green) for $y = 0$ after 20 and 40 flow through times [Vor]	38
4.1	Computational domain of the acoustic perturbation test	41
4.2	Wave propagation through the domain	42
4.3	Min. and max. pressure and velocity for Unsteady Implicit (black) and PISO (red) in the computational domain	43
4.4	Comparison of the acoustic perturbation for PISO and Unsteady Implicit after 40 reflections	44
4.5	Velocity and pressure after 0, 40, 160 and 320 timesteps in the domain for $M = 0.0288$	45

4.6	Velocity and pressure after 0, 40, 160, 320, 480 and 720 timesteps in the domain for $M = 0.3$ . . . . .	46
4.7	Exemplary pressure perturbation travelling in the duct . . . . .	46
4.8	Pressure signal of M1 ( $x = 0.1$ m) and M2 ( $x = 0.2$ m) and the reflection coefficient magnitude and phase for the velocity inlet . . . . .	47
4.9	Pressure signal of M5 ( $x = 0.8$ m) and M6 ( $x = 0.9$ m) and the reflection coefficient magnitude and phase for the pressure outlet . . . . .	48
4.10	Pressure signal of M1 ( $x = 0.75$ m) and M2 ( $x = 0.9$ m) and the reflection coefficient magnitude and phase for the freestream boundary condition . . . . .	48
5.1	Calculation time, Speedup factor and the linear Speedup factor over the number of processors using the Unsteady Implicit algorithm . . .	50
7.1	Experimental setup of the Volvo validation rig . . . . .	56
7.2	LDA measurements for the Volvo validation rig. [JE10] . . . . .	56
7.3	Measurement planes M1-M7 for the determination of flow field profiles . . . . .	57
7.4	RMS value of the pressure for different equivalence ratios and inlet velocities [SOS91] . . . . .	57
8.1	Computational domain of the Volvo case . . . . .	64
8.2	Refinement zone near the bluff body . . . . .	65
8.3	Mean x-velocities on M2-M5 for case C . . . . .	67
8.4	Mean velocity on the centeraxis for four different mesh densities using operating conditions of case C . . . . .	68
8.5	Residuals for case C using the $k - \epsilon$ closure with 2.2 million cells . . .	68
8.6	Flame shape for case R using the $k - \epsilon$ closure with 2.2 million cells .	69
8.7	Mean x-velocities on M2-M5 and mean x-velocity on M2 for case R . .	69
8.8	Mean velocity on the centeraxis for four different mesh densities using operating conditions of case R . . . . .	70
8.9	Temperature profiles on M5-M7 for case R . . . . .	70
8.10	Comparison between the kinetic rate and the turbulent flame speed closure for $k - \epsilon$ and the 2.2 Mio mesh . . . . .	71
8.11	Residuals for case R with 2.2 million cells . . . . .	72
9.1	Computational domain for the calculation of the mode shapes. H1, H2 and H3 indicate the the line probes for evaluation. . . . .	74
9.2	Absolute pressure amplitude of the 1L-0Ty-0Tz, 2L-0Ty-0Tz, 1L-1Ty-0Tz and 1L-0Ty-2Tz mode . . . . .	75
9.3	Modeshape of the 1L-0Ty-0Tz, 2L-0Ty-0Tz, 1L-1Ty-0Tz and 1L-0Ty-2Tz mode . . . . .	76
10.1	Short (Left) and long (Right) discharge duct . . . . .	78

10.2	Trend of $kg(x)$ in the domain of the Volvo case . . . . .	79
10.3	Fraction of the SGS Turbulent Kinetic Energy for case C . . . . .	81
10.4	Mean axial velocity on the centerline M1 behind the bluff body for case C . . . . .	82
10.5	Velocity profiles for case C. Left: Mean axial velocity on M2-M5. Right: Mean transverse velocity on M2-M5. . . . .	83
10.6	Evolution of the pressure contour for the non reacting case . . . . .	83
10.7	Location of the velocity probe . . . . .	84
10.8	Shedding frequency analysis for case C. Top right: Transverse velocity signal behind the bluff body. Bottom right: DWT of the signal. Bottom left: FFT transform of the signal . . . . .	84
10.9	Fraction of the SGS Turbulent Kinetic Energy for case R . . . . .	85
10.10	Case R: Pressure evolution for different boundary conditions. Left: Short domain. Right: Long domain . . . . .	87
10.11	Case R: Pressure evolution for different mach numbers of the freestream condition . . . . .	87
10.12	Mean axial velocity on the centerline M1 behind the bluff body for case R . . . . .	88
10.13	Velocity profiles for case R. Left: Mean axial velocity on M2-M5. Right: Mean transverse velocity on M2-M5 . . . . .	89
10.14	Temperature profiles on M5-M7 for case R . . . . .	89
10.15	Flame shape for the LES simulation with the long domain and a freestream outlet . . . . .	90
10.16	Case R, TFC: Blowoff of the flame . . . . .	90
10.17	Case R: Mean axial velocity on M1 for WALE and Dynamic Smagorinsky SGS modeling . . . . .	91
10.18	Case R, $B_1$ and $B_2$ : FFT's for different equivalence ratios $\phi$ at $x = 0.1$ m . . . . .	93
10.19	Case R, $B_1$ and $B_2$ : FFT's for different equivalence ratios $\phi$ at $x = 0.85$ m . . . . .	93
10.20	Comparison of the modeshapes of the LES for $\phi = 0.95$ and Comsol . . . . .	94
10.21	Surface FFT for the 1L mode (top) and the 2L mode (bottom) . . . . .	94
10.22	Case $B_1$ : Left: Mass fraction of OH indicating heat release. Right: FFT of mass fraction OH. . . . .	95
10.23	Visualized flame fronts of the experiments and the simulations . . . . .	95
10.24	RMS value of the pressure for different equivalence ratios and inlet velocities and results obtained by the LES simulations for $u_{in} = 17.3 \text{ m s}^{-1}$ . . . . .	96
10.25	3D image of an isosurface for $Y_{OH} = 0.01$ with the color indicating the axial velocity for case S . . . . .	97
10.26	Case S: FFT of a pressure signal at P $[0.1, 0, 0 \text{ m}]$ . . . . .	98
10.27	Speedup and Efficiency of StarCCM+ on JURECA . . . . .	98

# List of Tables

3.1	Initial conditions of the vortex and the flow field . . . . .	34
3.2	Numerical settings for the vortex preservation test case . . . . .	34
3.3	Settings of AVBP, YALES and OpenFOAM . . . . .	37
3.4	Computational time for the Vortex Preservation test case. Notation: Algorithm, segregated or coupled solver, spatial discretization, temporal discretization and computational time $[\frac{s}{\Delta t}]$ . . . . .	39
4.1	Flow variables of the wave propagation test . . . . .	42
4.2	Completed calculations for the numerical accuracy of the wave propagation . . . . .	42
4.3	Computational time for the wave propagation test case. Notation: Algorithm, spatial discretization, temporal discretization and computational time $[\frac{s}{\Delta t}]$ . . . . .	44
4.4	Completed calculations for the assessment of the boundary condition treatment . . . . .	45
4.5	Analytically derived reflection magnitude and phase [PV05] . . . . .	47
7.1	Operating points for the Volvo case . . . . .	58
7.2	Investigations on the Volvo validation rig of different research groups . . . . .	59
8.1	Smallest cell sizes in region around bluff body . . . . .	65
9.1	Frequencies and mode shapes obtained by the Helmholtz solver and LES in comparison with the experimental results [SOS91]. The mode name consists of the number of pressure nodes in x-direction (nLx), y-direction (pTy) and z-direction (qTz). . . . .	74
10.1	Outlet boundary conditions . . . . .	79
10.2	Vortex shedding frequencies for the experiment and LES simulations . . . . .	84
10.3	Case B: Investigated operating points with $p_{RMS}$ reported from the experiments for $x = 0.85$ m . . . . .	92
10.4	Case S: Investigated operating points with $p_{RMS}$ reported from the experiments for $x = 0.85$ m . . . . .	96



# List of Abbreviations

<b>Symbol</b>	<b>Definition</b>
<b>ACFL</b>	<b>A</b> coustic <b>CFL</b>
<b>BC</b>	<b>B</b> oundary <b>C</b> ondition
<b>BDS</b>	<b>B</b> ounded <b>C</b> entral <b>D</b> ifferencing
<b>BWD</b>	<b>B</b> ackward <b>D</b> ifferentiation
<b>CARS</b>	<b>C</b> oherent <b>A</b> nti- <b>S</b> tokes <b>R</b> aman <b>S</b> cattering
<b>CD</b>	<b>C</b> entral <b>D</b> ifferencing
<b>CFD</b>	<b>C</b> omputational <b>F</b> luid <b>D</b> ynamics
<b>CFL</b>	<b>C</b> ourant- <b>F</b> riedrichs- <b>L</b> evi- <b>N</b> umber
<b>CV</b>	<b>C</b> ontrol <b>V</b> olume
<b>DNS</b>	<b>D</b> irect <b>N</b> umerical <b>S</b> imulation
<b>DWT</b>	<b>D</b> iscrete <b>W</b> avelet <b>T</b> ransform
<b>FD</b>	<b>F</b> inite <b>D</b> ifferences <b>M</b> ethod
<b>FE</b>	<b>F</b> inite <b>E</b> lements <b>M</b> ethod
<b>FOU</b>	<b>F</b> irst <b>O</b> der <b>U</b> pwind
<b>FFT</b>	<b>F</b> ast <b>F</b> ourier <b>T</b> ransformation
<b>FTF</b>	<b>F</b> lame <b>T</b> ransfer <b>F</b> unction
<b>FV</b>	<b>F</b> inite <b>V</b> olumes <b>M</b> ethod
<b>GHG</b>	<b>G</b> reen <b>H</b> ouse <b>G</b> ases
<b>KR</b>	<b>K</b> inetic <b>R</b> ate
<b>LDA</b>	<b>L</b> aser <b>D</b> oppler <b>A</b> nemometry
<b>LES</b>	<b>L</b> arge <b>E</b> ddy <b>S</b> imulation
<b>NO<sub>x</sub></b>	<b>N</b> itrogen <b>O</b> xides
<b>NSCBC</b>	<b>N</b> avier- <b>S</b> tokes <b>C</b> haracteristics <b>B</b> oundary <b>C</b> onditions
<b>NSE</b>	<b>N</b> avier- <b>S</b> tokes <b>E</b> quations
<b>PISO</b>	<b>P</b> ressure <b>I</b> mplicit <b>S</b> plitting of <b>O</b> perators
<b>RANS</b>	<b>R</b> eynolds- <b>a</b> veraged <b>N</b> avier- <b>S</b> tokes
<b>SGS</b>	<b>S</b> ubgrid <b>S</b> cale
<b>SIMPLE</b>	<b>S</b> emi- <b>I</b> mplicit <b>M</b> ethod of <b>P</b> ressure- <b>L</b> inked <b>E</b> quations
<b>SOU</b>	<b>S</b> econd <b>O</b> der <b>U</b> pwind
<b>TFC</b>	<b>T</b> urbulent <b>F</b> lame <b>C</b> losure
<b>TKE</b>	<b>T</b> urbulent <b>K</b> inetic <b>E</b> nergy
<b>UI</b>	<b>U</b> nsteady <b>I</b> mplicit



# List of Symbols

Symbol	Definition	Unit
$L_0$	Integral turbulent length scale	m
$c_n$	Normalized reaction progress variable	-
$q$	Heat flux	$\text{W m}^{-2}$
$q'$	Heat flux fluctuation	$\text{W m}^{-2}$
$p$	Pressure	Pa
$p'$	Pressure fluctuation	Pa
$T$	Temperature	K
$u$	Velocity	$\text{m s}^{-1}$
$V$	Volume	m
$t$	Time	s
$g$	Growth rate of the instabilities	
$R_1$	Acoustic driving term	
$F_1$	Acoustic damping term	
$E_1$	Acoustic energy	
$u_i$	Velocity in i-direction	$\text{m s}^{-1}$
$Y_k$	Species mass fraction	-
$J_{j,k}$	Molecular diffusion flux	
$E$	Energy	J
$q_i$	Heat diffusion flux	
$R_0$	Universal gas constant	$\text{J kg}^{-1} \text{K}^{-1}$
$S_{ij}$	Strain tensor	
$M$	Molar mass	$\text{g mol}^{-1}$
$Ma$	Mach number	-
$J_k$	Scalar diffusivity	
$k$	Turbulent kinetic energy	
$k_{SGS}$	Fraction of the TKE that is modeled by the SGS mode	-1
$k_{Res}$	Fraction of the TKE that is resolved	-
$v'$	Stoichiometric coefficient	-
$k$	Rate constant	-
$Q_i$	Reaction rate	
$\dot{w}_k$	Production rate of species k	
$\dot{w}_t$	Source term of the heat release	
$\delta h_{f,k}^0$	Formation enthalpy of species k	$\text{J mol}^{-1}$
$z$	Mixture fraction	-

$y$	Un-normalized progress variable	-
$c$	Progress variable	-
$J_f^\phi$	Convective flux over face $f$	-
$R_\infty$	Riemann invariant for the incoming wave	-
$R_e$	Riemann invariant for the outgoing wave	-
$r$	Residual	-
$Su$	Speed Up Factor	-
$t_0$	Execution time for 24 processors	s
$t_N$	Execution time for N processors	s
$u_\infty$	Far field velocity	$\text{m s}^{-1}$
$c$	Speed of Sound	$\text{m s}^{-1}$
$f$	Frequency	$\text{s}^{-1}$
$\omega$	Angular frequency	$\text{s}^{-1}$
$H_{12}$	Transfer function for the microphone method	-
$y^+$	Dimensionless wall distance	-

---

$\rho$	Density	$\text{kg m}^{-3}$
$\tau_{ij}$	Stress Tensor	$\text{N m}^{-1}$
$T_{ij}$	Subgrid tensor	
$\eta$	Kolmogorov length scale	m
$\epsilon$	Dissipation rate	$\text{J kg}^{-1} \text{s}^{-1}$
$\Phi$	LES filter function	-
$\Delta$	LES filter	m
$\phi$	Generic variable	-
$\beta$	Temperature coefficient	-
$\Psi$	Potential	$\text{m s}^{-2}$
$\mu$	Viscosity	$\text{Pa s}$

---

$\nabla x$	Gradient of the vector field $x$	
$\delta_{ij}$	Kronecker delta	

## **Part I**

# **Introduction and Theoretical Background**



## Chapter 1

# Introduction and Context

### 1.1 Motivation

Human influence on the climate system has been documented by several publications including the Assessment Reports of the Intergovernmental Panel on Climate Change [CC13]. However, despite the continuous growth of renewable energies, the advent of carbon trading and various policy support mechanisms, Green House Gas emissions (GHG) are still increasing year by year [Age17]. The emissions are predicted to rise by over 50% to 2030 if no effective governmental policy actions are introduced.

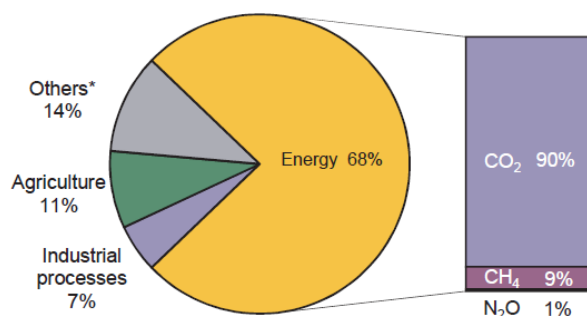


**Figure 1.1:** Estimated shares of GHG emissions by sector [Age17]

About 70 % of the emissions are produced by the energy sector, which is heavily dominated by combustion (Fig. 1.1). Even though, alternatives are available today, there are reasons that humanity still relies heavily on combustion. Energy sources have to be affordable, have a minimal impact on the environment and offer long-term security of supply at the same time [CC13]. Obviously these goals are always competing.

The major reason to use fossil fuels is an economic one. Unfortunately, in general, energies based on fossil fuels are still very cheap compared to renewable energies as wind, sun and hydro [ISE13]. Another problem is the security of supply. The exemplary renewable energies can only be used if wind blows, sun shines and water is available. This limits their reliability. The only missing alternative to fossil combustion based fuels is nuclear power. Being a possible contribution to a low

GHG emission electricity, nuclear power faces other barriers like recycling, safety and public image.

There are other sectors where combustion today is indispensable. While transport on the ground slowly starts to shift towards electric propulsion [BAS15], commercial aircrafts will rely on combustion for decades [Hep09]. This is due to the high energy density of liquid (nowadays kerosene-type) fuels.

As combustion will be present in the future, it is crucial to make its use as efficient as possible and thereby decrease the resulting pollutants and GHG emissions.

For propulsion of aircraft and helicopter, as well as for electricity generation, Gas Turbines are used. In the air, they offer the only possible option due to their ratio of power output to volume or mass respectively. For electricity generation they constitute a promising method, as they can react flexibly on fluctuating energy demands and thereby represent a good combination with renewable energies. In combined cycle with a steam turbine their electrical efficiency exceeds 60% [AG16].

Lean premix combustors are state of the art for stationary Gas Turbines. The goal is to reduce the  $NO_x$  emissions by burning in the under stoichiometric fuel/air mixtures. Able to reduce emissions, this mode is sensible to combustion instabilities [HY09]. These combustion instabilities are not desired, as they produce noise (environmental aspects) and limit operating range of the system.

### Objective of this thesis

Computational Fluid Dynamics is a powerful method in the field of fluid dynamics and combustion. Especially Large Eddy Simulations (LES) have proven numerous, that they are a promising tool to predict thermoacoustic instabilities [Gha+15] [ZNB16] [Fur17].

Offering the possibility for LES, the software package StarCCM+ has never been used to study thermoacoustics until now. This thesis aims to evaluate the capabilities of StarCCM+ to handle this phenomenon. Generic test cases and a validation case are investigated. Boundary conditions, numerical schemes and different settings are tested to gain insight into combustion instabilities and answer the question if StarCCM+ is able to predict thermoacoustics reliably.



## 1.2 Introduction

For centuries thermoacoustic instabilities have been known to humanity. One of the famous examples of these oscillations is the so called Rijke tube [Rij59]. It was introduced by the dutch professor in 1859. The simple experiment is shown in Fig. 1.2. It has to be noted, that the pipe is orientated horizontally here for reasons of clarity. In the experimental setup it is orientated vertically. The cylindrical tube is open at both ends and the wired mesh inside the tube is heated by a flame. When the flame is removed a loud sound is audible until the mesh cooles down again.

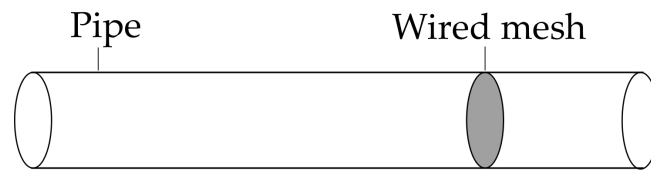


Figure 1.2: Rijke Tube [Rij59]

The mechanism that leads to the oscillations was already explained 1878 by Lord Rayleigh [Ray78]. Two different motions are formed inside the tube. A standing acoustic wave and the constant buoyant motion due to the heating at the mesh. This superposition creates fluctuations of the velocity at the mesh. Subsequently the heat tranfer fluctuates. According to the gas law this leads to pressure oscillations, which are responsible for the generated sound.

For modern combustion devices as Gas Turbines combustion instabilities are more severe. The instabilities are characterized by large amplitudes and are spontaneously excited through a feedback loop between acoustics, flow and combustion [Lie12]. Compared to the mentioned Rijke tube the heat release from combustion is higher by magnitudes. Thereby the instabilities lead to major problems for the combustion system. Pressure and velocity oscillations generate high mechanical loads resulting in fatigue of components. Increased heat transfer leads to thermal stress of the combustor walls and even flashbacks or blowoff of the flame is possible [ZL05].

As a consequence research and development in this field has gained importance over the last decades with the goal to derive methods to predict and subsequently suppress these instabilities. This chapter is meant as an introduction about the occurence of thermoacoustics. Afterwards the methods to study them will be introduced.

### 1.2.1 Combustion Instabilities

Zinn et al. [ZL05] summarized the circumstances under which thermoacoustic instabilities occur (Fig. 1.3). On the top, a simplified combustor is displayed. Reactants are entering the combustor from the left and are discharged on the right as products. The prevalent unsteady heat release interacts with the acoustic modes of the confined combustor.

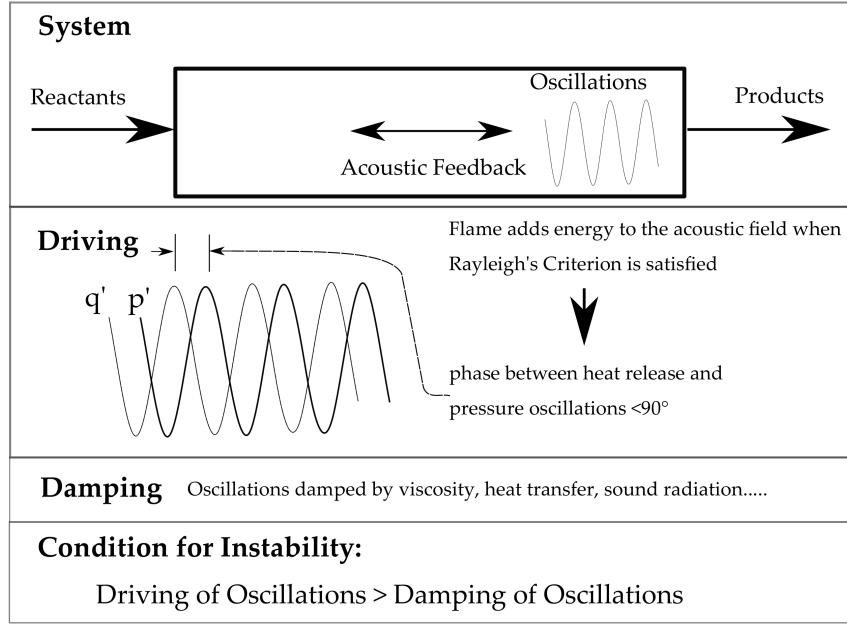


**Figure 1.3:** Circumstances enabling the occurrence of combustion instabilities

However, to excite combustion instabilities spontaneously, two conditions have to be fulfilled. First, the Rayleigh criterion, which writes

$$\int_{\tau} \int_V p'(x, t) q'(x, t) dt dV \geq 0 \quad (1.1)$$

has to be satisfied [Ray78].  $p'$  and  $q'$  are the pressure and heat release fluctuations respectively.  $V$  represents the volume of the domain and  $t$  the time. The instability is fed if  $p'$  and  $q'$  are in phase. In other words, the pressure and heat release fluctuations have to increase or decrease at the same time. This is the case if the phase difference is smaller than  $90^\circ$  [Lie+01b]. However, transferring energy does not necessarily imply instability. Extending the Rayleigh criteria by including the damping of the oscillations the equation takes the form

$$\int_{\tau} \int_V p'(x, t) q'(x, t) dt dV \geq \int_{\tau} \int_V \sum_i L_i(x, t) dt dV. \quad (1.2)$$

As second condition the driving of the thermoacoustics has to exceed the energy losses  $L_i$  of the damping term. Damping of the oscillations is present due to different reasons. E.g. the oscillations can leave the domain through the boundaries and viscosity or heat transfer are able to dissipate the fluctuations [ZL05].

In form of a generalized Rayleigh Criterion, equation 1.2 can be stated as [Poi15]

$$g = \frac{(R_1 - F_1)}{2E_1}. \quad (1.3)$$

The growth rate  $g$  represents the difference between the driving and the damping term  $R_1$  and  $F_1$  respectively.  $E_1$  represents the period-averaged acoustic energy of

the combustor.

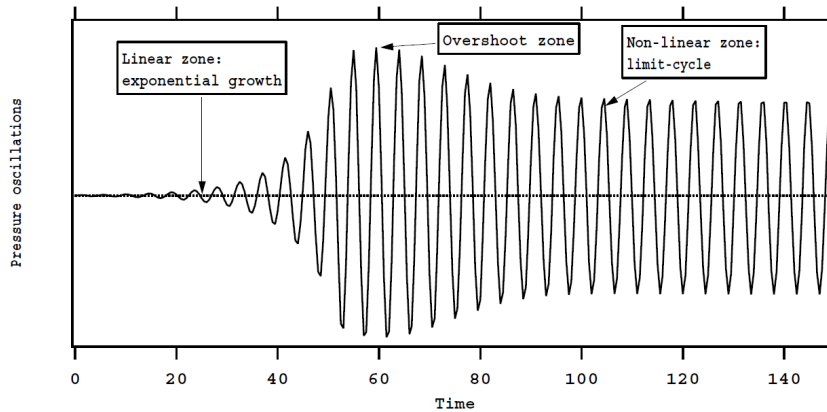


**Figure 1.4:** Growing combustion instability that leads a limit cycle [PV05]

As long as the condition for instability is fulfilled, the growth rate is positive and the oscillations grow with time. Then, either the combustor gets destroyed or, at a certain point, the damping terms equal the driving terms and no energy is added to the oscillating mode. Then a limit cycle, as shown in figure 1.4 [PV05] is reached. After a linear growth zone the amplitudes of the instability overshoot and eventually saturate in a non-linear limit-cycle.

Predominantly the instabilities correspond to natural acoustic modes of the combustor. They can be calculated using the Helmholtz equation (see section 2.2) giving an infinite set of eigenmodes [Ehr03]. In general three different forms of modes can be distinguished. Modes can have longitudinal, transversal and azimuthal shapes or consist of superspositions of them. A closer look on the determination of these modes will be taken in section 2.2.

The next sections provide insight into the processes responsible for driving and damping.

### 1.2.2 Driving Mechanisms for Combustion Instabilities

In the previous section, the combustion instabilities controlling feedback cycle has already been introduced. Following Poinso's work [Poi15] an exemplary feedback cycle can be displayed as in figure 1.5. The graph is subdivided in an acoustic and a convective world. This differentiation will be of value when the methods to study thermoacoustics are introduced.

The driving mechanisms of the acoustic feedback loop can be summarized according to [ZL05]:

- **Inlet Flow Rate Change**

Pressure fluctuations in the combustor influence the pressure drop at the inlets. This results in unsteady inlet flows for both fuel and air. Mixing processes

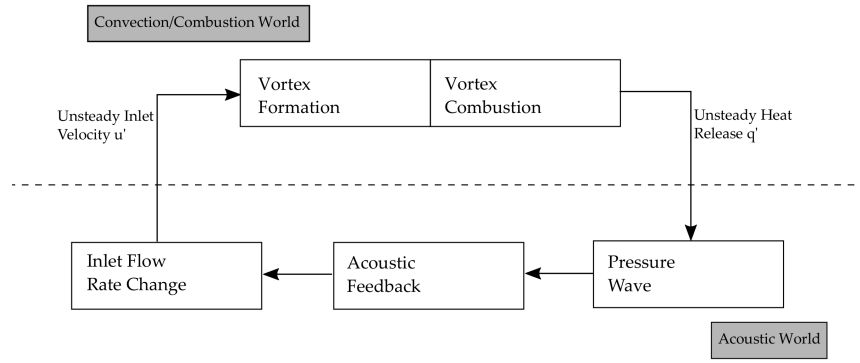


**Figure 1.5:** Feedback loop for a confined combustor

are modulated as well. The oscillating mass flow and mixture composition produces unsteady heat release in the combustion zone and drive the instability [Lie+01a].

- **Flame Area Variation**

Pressure and Velocity oscillations interact with the flame front. The variation of the flame front leads to an unsteady heat release [S.02].

- **Vortex Shedding**

Vortex shedding is a common flow feature in fluids. It takes place when a flow passes a bluff body and creates vortices periodically [FOM86]. In reacting flows bluff bodies are frequently used to create recirculation zones that anchor the flame. The combustion of the vortex and the breakdown of the vortical structures create unsteady heat release driving the acoustic field [ZL05].

In few words, the fluctuations of  $u$  and the mixture fraction induce fluctuations of the heat release. The resulting unsteady gas expansion leads to pressure fluctuations. The confinement of the combustion provides the ability for an acoustic feedback and the loop is closed. But still, to add energy to the acoustic field, the Rayleigh criterion (Eq. 1.1) has to be satisfied.

### 1.2.3 Damping Mechanisms for Combustion Instabilities

On the other side, the damping terms reduce the acoustic energy inside the combustor. They represent a key parameter to determine the instability of a combustor. Three processes of damping can be distinguished [ZL05]:

- **Viscous Dissipation and Heat Transfer**

The mechanisms are dominated by the conversion of acoustic energy into vorticity. They can be subdivided in the regions in which they occur, boundary layer losses and flow separation losses. Hereby the fluctuations partially are converted into entropy and vorticity fluctuations.

- **Convection and Radiation**

Combustion instabilities are considered in confined geometries as those create the fundamentals for an acoustic feedback. However fluctuations can be convected or radiated out of the domain. The level of reflection at the exit depends on numerous factors like the geometry, frequency, mean flow velocity and the characteristics of the system connected to the investigated chamber [PV05].

- **Transfer between modes**

Generally combustors respond to disturbances over a very narrow frequency range leading to a nearly pure tone at specific frequencies. Therefore, mechanisms transferring energy from the excited frequencies to others which are either not amplified or at which the energy is more readily dissipated, constitute to the damping [Lie05].

### 1.3 Approaches to study combustion instabilities

The statements of the last section showed the complexity of mechanisms which play a role in the field of thermoacoustics. Limiting them is of major interest in the design phase of every combustion component. Therefore appropriate methods had to be derived.

Describing the movement of fluids and gases, fluid mechanics became a large discipline in the field of physics. The Navier-Stokes equations have been derived to offer a full description for this motion. They also include all the information needed to study thermoacoustic instabilities.

The technological progress in the field of computation during the last decades made the application of Computational Fluid Dynamics possible. But even with the growing resources we have today, solving the full NSE for realistic applications is and probably will stay impossible for the near future.

To compute the flow features of real systems, simplifications have to be made. Therefore, starting from the reacting, compressible form of the NSE the mathematical models behind the different methods will be derived and explained.

Depending on the simplifications we can derive two main classes for the computation of combustion instabilities as shown in figure 2.1 [PV05].

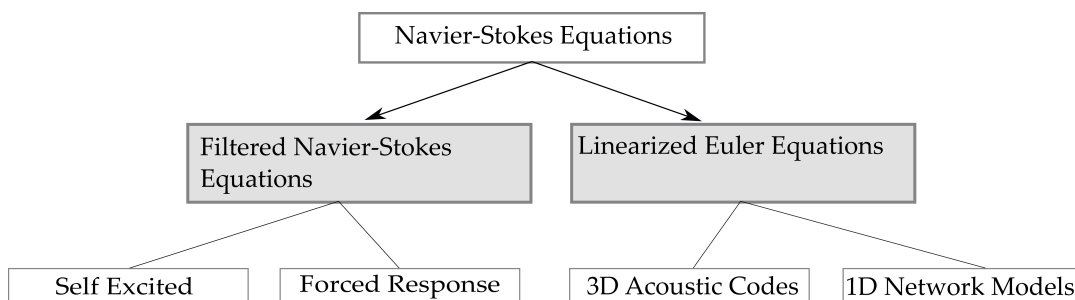


**Figure 1.6:** Possibilities to study thermoacoustic instabilities [Gha15]

The first part are the Filtered Navier-Stokes equations, more specifically Large Eddy Simulations. Per definition, they are intrinsically unsteady while large scale turbulence is computed and small scale turbulence is modeled.

LES methods can further be subdivided into self excited and forced response method [PV05]. In the latter a perturbation is introduced into the flow and the response is observed. Thereby a flame transfer function (FTF), which relates the heat release to the acoustic fluctuations [Toe17], can be derived. In self-excited methods the flow develops instabilities without forcing. This is the method that will be used during this work with StarCCM+.

On the other side the linearized Euler equations can be derived from the NSE by introducing further simplifications. The equations are simplified drastically by linearizing around a stationary mean flow, resulting in an immensely lower computational effort. This is not the only reason that makes this method attractive. The use of FTF's in acoustic solvers enables also the investigations of growth rates that lead to instabilities [DSG14]. 1-D network models facilitate the computation of full combustion chambers [Wer+06] which are only rarely computed in LES up to now [P.+10] [EC11].

In the following an introduction into CFD is done with the NSE and from them the different models are derived. As this work is done with StarCCM+ emphasis is put on models and methods used in this program.

## Chapter 2

# Theoretical Background

## 2.1 Computational Fluid Dynamics

### 2.1.1 Governing Equations of Fluid Mechanics

The governing equations of fluid flows are represented by the conservation equations [PV05]. The momentum equation writes

$$\frac{\partial \rho u_j}{\partial t} + \frac{\partial \rho u_i u_j}{\partial x_j} = -\frac{\partial}{\partial x_j} (p \delta_{ij} - \tau_{ij}), \quad (2.1)$$

where  $\frac{\partial}{\partial t}$  and  $\frac{\partial}{\partial x_j}$  indicate the temporal and spatial derivative in j-direction.  $\rho$  represents the density,  $u_j$  the velocity component in j-direction,  $p$  the pressure and  $\tau$  the viscous stress tensor. Volume forces acting on the flow are neglected. It has to be noted that the Einstein summation convention is adopted.

With  $Y_k$  as the mass fraction of species  $k$ ,  $\dot{w}_k$  representing the production rate and  $J_{j,k}$  the molecular diffusion flux, the mass conservation equation for each species  $k$  is given by

$$\frac{\partial \rho Y_k}{\partial t} + \frac{\partial \rho u_j Y_k}{\partial x_j} = -\frac{\partial}{\partial x_j} J_{j,k} + \dot{w}_k \quad \text{for } k = 1, N. \quad (2.2)$$

The global mass conservation equation without the differentiation of species reads

$$\frac{\partial \rho}{\partial t} + \frac{\partial \rho u_i}{\partial x_i} = 0. \quad (2.3)$$

The set of the conservation equations is completed by the energy equation

$$\frac{\partial \rho Y_k}{\partial t} + \frac{\partial \rho E u_j}{\partial x_j} = -\frac{\partial}{\partial x_j} (u_i (p \delta_{ij} - \tau_{ij}) + q_i) + \dot{w}_t, \quad (2.4)$$

where  $E$  describes the energy per mass unit (specific internal and kinetic energy),  $\dot{w}_t$  the source term for the heat release,  $q_j$  the heat diffusion fluxes

Further on, the assumption of a Newtonian fluid can be done characterizing the fluid in such way that the viscous stress tensor is linearly dependent on the velocity

gradients within the flow [F08]. Expressed with the Kronecker delta function  $\delta_{ij}$  the stress tensor writes is

$$\tau_{ij} = 2\mu \left( S_{ij} - \frac{1}{3} \delta_{ij} S_u \right) \quad (2.5)$$

while the strain rate tensor is defined as [Pop]

$$S_{ij} = \frac{1}{2} \left( \frac{\partial u_i}{\partial x_j} + \frac{\partial u_j}{\partial x_i} \right). \quad (2.6)$$

To relate pressure, volume/density and temperature the equation of state is introduced following the ideal gas law [WMD06]. With  $R_0$  as the specific gas constant and  $\bar{M}$  the molar weight of the mixture the ideal gas law is defined as

$$p = \rho T \frac{R_0}{\bar{M}}. \quad (2.7)$$



### 2.1.2 Approaches to compute turbulent flows

To distinguish between the methods of computational fluid dynamics, the features of fluid motion have to be considered. Flows in industrial applications are almost always turbulent. In turbulent flows the fluid velocity field varies irregularly in time and space and develops a chaotic flow pattern [Pop].

Visually, the unsteady flow pattern can be described by eddies. Hereby the integral length scale  $L_0$  denotes the size of largest eddies in the flow and the Kolmogorov length scale  $\eta$  the smallest ones. Following the energy cascade the large eddies break up into smaller eddies until  $\eta$  is reached and the energy is dissipated by viscous forces [Pop].

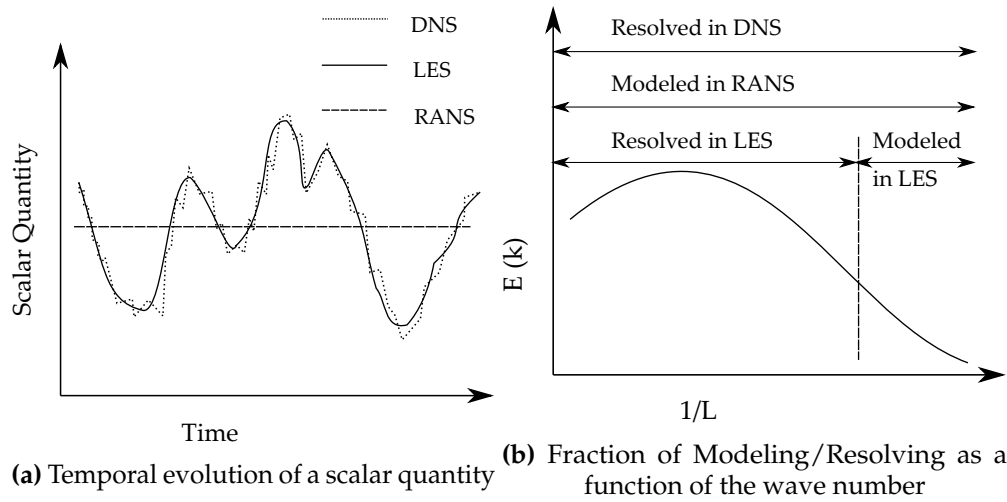


**Figure 2.1:** Comparison of RANS, LES and DNS simulations [PV05]

Introducing the energy spectrum in Fig. 2.1b allows to distinguish the approaches to compute turbulent flows based on the length scale  $L$ .

To solve the equations, that were presented in the previous section, three main approaches exist [PV05]:

- **Direct Numerical Simulation (DNS)**

Solving the full set of NSE without the introduction of turbulence models, the discretization step has to be smaller than the length scales of the smallest scales of the exact solution. Therefore DNS is computationally very expensive and still limited to academic cases [ZyB14] [LC89]. However, its ability to study complex phenomena at maximum detail puts this method into a leading position for the validation of models.

- **Reynolds-Averaged Navier-Stokes (RANS)**

Due to the low computational effort RANS calculations were the first feasible approach and are nowadays still the standard technique to solve the NSE [PV05]. The use of ensemble averaging leads to mean fields of the flow quantities. As the averaging process adds unclosed terms, turbulence models are introduced and subsequently the full range of turbulent scales is modeled [FP02]. Regarding

the topic of this thesis, RANS faces an inherent drawback as fluctuation values cannot be recovered (Fig. 2.1A). However, RANS calculations are done and compared to the experimentally reported mean flow fields and later on used for initialization of the LES simulations. Their background shall be introduced here briefly. For further information the reader is referred to the textbook of Ferziger [FP02].

The starting point are the balance equations that were introduced in section 2.1.1. Reynolds averaging splits any quantity  $\phi$  into a mean component  $\bar{\phi}$  and a fluctuating component  $\phi'$  [Pop]:

$$\phi = \bar{\phi} + \phi' \quad \text{with} \quad \widetilde{\phi''} = 0 \quad (2.8)$$

The procedure is applied to each of the balance equations creating unclosed terms. However, it may only be presented for the momentum equation here as this reveals the resulting term of the Reynolds stresses  $\widetilde{u_i'' u_j''}$ , which is closed by the turbulence model. The averaged momentum equation reads [PV05]

$$\frac{\partial \bar{\phi} \widetilde{u_i}}{\partial t} + \frac{\partial}{\partial x_i} (\bar{\rho} \widetilde{u_i u_j}) + \frac{\partial \bar{p}}{\partial x_i} = \frac{\partial}{\partial x_i} \left( \bar{\tau}_{ij} - \bar{\rho} \widetilde{u_i'' u_j''} \right). \quad (2.9)$$

Turbulence models are used to close the six unknown quantities in  $\widetilde{u_i'' u_j''}$ . The turbulent viscosity model, where the effect of turbulent fluctuations is assumed to be of diffusive nature, introduces the Boussinesq approximation

$$\overline{\rho u_i' u_j'} = \bar{\rho} \nu_t \left( \frac{\partial \bar{c}_j}{\partial x_i} - \frac{\partial \bar{c}_i}{\partial x_j} \right) \quad (2.10)$$

with the turbulent viscosity  $\nu_t$  [Bou87].

Hereby a dependent direction of the turbulence, that is known as isotropy is assumed. By this, only one unknown variable  $\nu_t$  is left that has to be determined with modeling approaches. To obtain satisfactory results two-equation models have to be used [F08]. Two different eddy viscosity models are presented and used:

### Realizable $k - \epsilon$ Model

The standard  $k - \epsilon$  model is the most commonly used turbulence model.  $k$  is the turbulent kinetic energy, and  $\epsilon$  the dissipation rate of  $k$ , whereby  $k$  is connected to large scaled turbulent structures and  $\epsilon$  to small scaled ones. Both quantities are modeled by independent transport equations. With moderate effort, results are provided sufficiently accurate [FP02]. The Realizable  $k - \epsilon$  model is an improvement of the standard  $k - \epsilon$  model. This approach contains a new transport equation for  $\epsilon$  and the critical model coefficient  $C_{nu}$  is modeled as function of the mean flow and the turbulence instead of being a constant.

Thereby mathematical constraints of the normal stresses are satisfied in conjunction with the physics of turbulence. Better performance as the standard approach was observed for many applications [Sta].

### SST $k - \omega$ Model

The SST  $k - \omega$  Model is a hybrid model of the standard  $k - \omega$  and  $k - \epsilon$  model. To switch between both models the blending function is used. When the  $k - \omega$  model is used,  $\epsilon$  is replaced by the vortex frequency  $\omega$ . The model shows its advantages especially near the wall as it provides a considerably better description of medium scaled eddy structures with high numeric stability [LS13].

- **Large Eddy Simulation (LES)**

Constituting the main part of this thesis, LES represents a middle path between DNS and RANS. Motivated by the limitations of the other approaches, LES calculates the large-scale turbulence explicitly and models the smaller scales, which have a more universal character [Pop]. This allows to use coarser grids and avoids the vast computational costs for the calculation of the small-scale motions.

Starting from the NSE equations, instead of an averaging process (RANS), spatial filtering is introduced.

The LES filter function  $\Phi(x - x', \Delta)$ , is characterized by the filter width  $\Delta$ . It determines until which cut-off length turbulence is resolved and which part is modeled by the subgrid scale model (SGS). For a generic variable  $\phi(x)$  the spatial filtering operator reads

$$\tilde{\phi}(x) = \int \phi(x') \Phi(x - x', \Delta) dx'. \quad (2.11)$$

By introducing

$$\bar{\rho} \tilde{\phi} = \overline{\rho \phi} \quad (2.12)$$

density variations are accounted for through favre averaging. Thereby the field is decomposed into a filtered and a residual field following

$$\phi(x) = \widetilde{\phi(x)} + \phi'(x). \quad (2.13)$$

StarCCM+ uses implicit filtering. In consequence the mesh determines the filter width  $\Delta$  [Sta]. Filtering equations 2.1, 2.2 and 2.4 leads to [PV05]

$$\boxed{\frac{\partial \bar{\rho} \tilde{u}_j}{\partial t} + \frac{\partial \bar{\rho} \tilde{u}_i \tilde{u}_j}{\partial x_j} = - \frac{\partial}{\partial x_j} (\bar{p} \delta_{ij} + \bar{\rho} (\widetilde{u_i u_j} - \tilde{u}_i \tilde{u}_j) - \tau_{ij})}, \quad (2.14)$$

$$\boxed{\frac{\partial \widetilde{\rho Y_k}}{\partial t} + \frac{\partial \widetilde{\rho u_j Y_k}}{\partial x_j} = -\frac{\partial}{\partial x_j} (\overline{J_{j,k}} + \overline{\rho(u_j \widetilde{Y_k} - \widetilde{u_j Y_k})} + \overline{w_k})} \quad \text{for } k = 1, N \quad (2.15)$$

and

$$\boxed{\frac{\partial \widetilde{\rho E}}{\partial t} + \frac{\partial \widetilde{\rho E u_j}}{\partial x_j} = -\frac{\partial}{\partial x_j} (\overline{u_j(p\delta_{ij} - \tau_{ij})} + \overline{q_i} + \overline{\rho(u_j \widetilde{E} - \widetilde{u_j E})} + \dot{w}_t)} \quad (2.16)$$

Comparable to RANS calculations, the spatial filtering produces unclosed terms in the conservation equations. Therefore a subgrid-scale model is introduced.

### Sub-grid scale modeling

In this work the Wall-Adapting Local-Eddy Viscosity (WALE) subgrid scale model [FF99] is used [Sta]. The eddies that are smaller than the grid size are accounted for through the subgrid tensor  $T_{ij}$

$$T_{ij} = (\widetilde{u_i u_j} - \widetilde{u_i} \widetilde{u_j}). \quad (2.17)$$

Based on the eddy viscosity assumption the subgrid tensor can be modeled by [FFT]

$$T_{ij} = 2\nu_t \overline{S_{ij}} + \frac{1}{3} T_{kk} \delta_{ij} \quad (2.18)$$

with

$$\overline{S_{ij}} = \frac{1}{2} \left( \frac{\partial \overline{u_i}}{\partial \overline{x_j}} + \frac{\partial \overline{u_j}}{\partial \overline{x_i}} \right). \quad (2.19)$$

For the WALE subgrid modeling approach the turbulent viscosity is introduced [FF99]

$$\nu_t = (C_w \Delta)^2 \frac{(S_{ij}^d S_{ij}^d)^{(3/2)}}{(\widetilde{S_{ij}^d} \widetilde{S_{ij}^d})^{(5/2)} + (S_{ij}^d S_{ij}^d)^{(5/4)}}. \quad (2.20)$$

With the alternative operator  $S_{ij}^d$  in comparison the standard Smagorinsky model

$$S_{ij}^d = \frac{1}{2} \left( \frac{\partial \widetilde{u_i}^2}{\partial x_j} + \frac{\partial \widetilde{u_j}^2}{\partial x_i} \right) - \frac{1}{3} \delta_{ij} \frac{\partial \widetilde{u_k}}{\partial x_k}. \quad (2.21)$$

The WALE subgrid model was introduced because the Smagorinsky model showed too much dissipation and did not perform well near to the walls. The introduction of the new operator improved the turbulent intensities and the prediction of the wall stress rate [FFT].

### 2.1.3 Species Transport and Reacting Flow

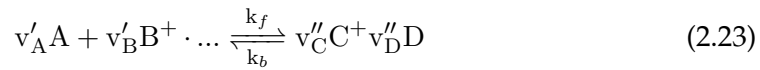
The mixture of the gas has to be tracked individually for each species. Therefore reaction rates and transport coefficients have to be derived.

StarCCM+ solves transport equations for all species to ensure that all mass fractions sum to 1. As the multi-component gas option is applied in reacting cases, the Fick's law gets replaced by a matrix to calculate the scalar diffusivity [Sta]:

$$J_k = \rho \sum_j^N D_{k,j} \nabla Y_j \quad (2.22)$$

$D_{k,j}$  are the multi-component diffusion coefficients. They are calculated based on the Maxwell equations. For further information the reader is referred to [Sta]. To derive relations for the reaction rate  $\dot{w}_k$  and the source term of the heat release  $\dot{w}_T$  the chemical kinetics have to be considered. At first the basics of chemical kinetics are considered.

Equation 2.23 represents any chemical reaction of the educts A and B to C and D with the stoichiometric coefficients  $v$  and reaction rate  $k$ .  $f$  and  $b$  denote forwards and backwards reactions respectively [Sta].



The rate constant  $k$  is based on the Arrhenius equation [WMD06]

$$k = AT^\beta \exp\left(-\frac{E_a}{R_u T}\right). \quad (2.24)$$

The temperature exponent  $\beta$ , the activation energy  $E_a$  and  $A$  are provided by the chemical mechanism. Chemical mechanisms are based on experimental data. They include all the species and reactions that are of importance in the combustion of the specified fuel. Numerous mechanisms exist for the combustion of hydrocarbon fuels. During this work only GRI-Mech 3.0 (325 reactions and 53 species) [Smi+] and the San Diego (247 reactions +50) mechanism [MSD] will be used. They are both applicable to a wide range of combustion processes.

The reaction rate progress is

$$Q_i = k_{f,j} \prod_{k=1}^N \left(\frac{\rho Y_k}{M_k}\right)^{v'_{kj}} - k_{b,j} \prod_{k=1}^N \left(\frac{\rho Y_k}{M_k}\right)^{v''_{kj}}. \quad (2.25)$$

Subsequently for  $S$  reactions and  $N$  species this leads to

$$\dot{w}_k = M_k \sum_{j=1}^S (v'_{kj} - v''_{kj}) Q_j \quad (2.26)$$

and

$$\dot{w}_t = - \sum_{k=1}^N \dot{w}_k \delta h_{f,k}^0 \quad (2.27)$$

for the reaction rate  $\dot{w}_k$  of species  $k$  and the heat release  $\dot{w}_t$ . The formation enthalpy of species  $k$  is represented by  $\delta h_{f,k}^0$ .

Equations 2.24 to 2.27 yield a system of equations which render a straightforward integration almost impossible in the scope of turbulent combustion [Pet00]. Two different approaches will be used to model the combustion in this work:

- **Complex Chemistry**

As noted previously, the reaction mechanisms comprise hundreds of reactions and dozens of species. The complex chemistry approach can be seen as the brute force method to derive the information about the reacting species. For each species an additional balance equation is added. This leads to  $4 + N$  equations that have to be solved [PV05]. A stiff ODE solver is used to integrate the chemical source terms. For turbulence/combustion interaction the Laminar Flame Concept is used, which includes the interaction through the increased turbulent diffusivity [Sta].

- **Tabulated Chemistry**

The tabulated chemistry approach is based on the method of Intrinsic Low-Dimensional Manifolds (ILDM) proposed by Maas et al [MP92]. A procedure was introduced to simplify chemical kinetics by eliminating the steady state species and therefore reduces the number of variables [Toe17]. This results in look up tables which contain the reaction rates in function of few variables. However it failed to deliver accurate results for low temperatures as these regions are not covered and usually determined by linear interpolation [PV05].

In StarCCM+ Flamelet Generated Manifolds (FGM), an advanced method overcoming this limitation, is used. The approach represents a 3D turbulent flame front as a combination of 1-D laminar flame elements (flamelets) [Pet00].

Based on complex chemistry reaction mechanisms, look-up tables are generated a priori inside StarCCM+. Reaction rates and mass fractions are calculated as functions of the mixture fraction  $Z$  and the progress variable  $y$ . This reduces the additional number of balance equations due to the combustion from  $N$  representing the number of species to 2.

The mixture fraction is defined by the mass fraction of the fuel in the fresh gas stream [Flu]

$$z = \frac{m_{fuel}}{m_{fuel} + m_{oxidizer}}. \quad (2.28)$$

A transport equation is solved for the un-normalized progress variable  $y$  [Sta].  $y$  is based on the species weights of  $CO$  and  $CO_2$ . Using the species weight  $W$  and the mass fraction  $Y$ ,  $y$  is calculated based on

$$y = W_{CO_2}Y_{CO_2} + W_{CO}Y_{CO}. \quad (2.29)$$

Subsequently the normalized progress variable  $c_n$  can be derived by

$$c_n = \frac{y - y_{c=0}}{y_{c_n=1} - y_{c_n=0}}, \quad (2.30)$$

where  $y_{c_n=0}$  and  $y_{c_n=1}$  are the un-normalized progress variables at the initial state and equilibrium state respectively.

The source term in the transport equation for the unnormalized progress variable has to be modeled to describe the turbulence-chemistry interaction. This source term determines the flame position. Two different options are used in the scope of this work.

- The **Kinetic Rate Closure** uses the chemical rate based on the FGM table to integrate the source term. The effect of turbulence and the laminar flame speed is not included in the prediction of the source term [Sta].
- **Turbulent Flame Speed Closure (TFC)** has the advantage that the model parameter  $A$  can be calibrated to predict the flame position accurately [Flu]. Based on the Zimont method, which reads

$$S_T = \frac{1}{2} G(u')^{\frac{3}{4}} S_L^{\frac{1}{2}} \alpha_u^{-\frac{1}{4}} I_l^{\frac{1}{4}}, \quad (2.31)$$

the turbulent flame speed is calculated with the stretch factor  $G$ , the velocity fluctuation  $u'$ , the laminar flame speed  $S_L$ , the thermal diffusivity  $\alpha_u$  of the unburnt mixture and the integral turbulent length scale  $I_l$ . For further information about this method the reader is referred to the original publication by Zimont et Al. [VL+98].

#### 2.1.4 Solution Methods

In the previous sections the equations describing a fluid flow with combustion have been derived. This section aims to introduce the procedure to solve them. The solving procedure can be divided into three steps [FP02]:

- Discretization of the partial differential equations
- Pressure-velocity coupling
- Solving the resulting system of equations

As no analytical solution of the NSE exists for cases of interest, numerical methods are applied to solve them. The goal is to transform the partial differential equations to accurate algebraic equivalents.

## Discretization

Different approaches to approximate the equations exist. The most important ones are: finite differences (FD), finite elements (FE) and finite volumes (FV). Only the latter is explained here, as it is used in StarCCM+.

The first step is the subdivision of the domain of interest into a finite number of control volumes (CV). This is done through the mesh generation [FP02].

Onto each of the CVs, the conservation equations are applied in integral form. With applying the Gauss's divergence theorem a transport equation for a generic scalar property  $\phi$  writes [Sta]

$$\underbrace{\frac{d}{dt} \int_V \rho \phi dV}_{\text{Transient Term}} + \underbrace{\int_A \rho v \phi da}_{\text{Convective Flux}} = \underbrace{\int_A \tau \nabla \phi da}_{\text{Diffusive Flux}} + \underbrace{\int_V S_\phi dV}_{\text{Source Term}}. \quad (2.32)$$

Each of the terms in the conservation equation is evaluated individually. This said, emphasis will be put on the transient term and the convective, herinafter referred to as temporal and spatial discretization. The approximations of the integrals for the diffusive flux and the source term are implemented up to  $2^{nd}$  order accurate in StarCCM+.

## Spatial Discretization

The convective flux is approximated using the  $2^{nd}$  order midpoint rule [Eds15]

$$\int_A J^\phi dA = \sum_f J_f^\phi a_f. \quad (2.33)$$

Thereby the flux over the surface  $A$  of the CV is approximated by the sum of the fluxes  $J_f^\phi$  over the cell faces  $f$ . To derive the fluxes, the values of the cell centers have to be known. Generally different methods are available, differing in terms of accuracy and boundedness. Two interpolations are used in this work.

- **Bounded Central-Differencing (BDS)** represents a blend of the unconditionally bounded  $1^{st}$  order upwind differential scheme (FOU), the  $2^{nd}$  order upwind scheme (SOU) and the central-differencing scheme (CDS). The formulation of the flux is [Flu]

$$J_f^\phi = \begin{cases} \dot{m} \phi_{FOU} & \text{for } \xi < 0 \text{ or } 1 < \xi \\ \dot{m}(\sigma \phi_{CDS} + (1 - \sigma) \phi_{SOU}) & \text{for } 0 \leq \xi \leq 1 \end{cases}, \quad (2.34)$$

where  $\phi$  represents the cell-face center value of the corresponding scheme and  $\xi$  is a value that is based on local conditions and the upwind blending factor that is introduced to control the balance between the schemes. This approach combines the advantages of the different strategies as the FOU stabilizes the



solution and the CDS, prone to dispersive errors, preserves the turbulent kinetic energy where the SOU scheme would tend to decay it unnaturally fast.

- **Hybrid MUSCL  $3^{rd}$ -Order/Central-Differencing** is the highest order scheme available in StarCCM+ [Sta]. The blend is defined as

$$J_f^\phi = \begin{cases} \dot{m}\phi_{FOU} & \text{for } \xi < 0 \text{ or } 1 < \xi \\ \dot{m}(\sigma\phi_{MUSCL} + (1 - \sigma)\phi_{CD3}) & \text{for } 0 \leq \xi \leq 1 \end{cases}. \quad (2.35)$$

As with the BDS, based on  $\xi$  the scheme switches between the FOU scheme for non-smooth flows (shocks) and a blend of a MUSCL  $3^{rd}$ -order and  $3^{rd}$ -order CD scheme. The higher order terms lead to a scheme which is supposed to reduce the dissipation in comparison to the  $2^{nd}$  order schemes.

### Temporal Discretization

In the case of an unsteady flow, the underlying equations are discretized not only in space but also in time. Three different options, distinguished by the number of time-levels, are used in this work:

- Also referred to as Euler Implicit [Eds15], the  $1^{st}$  order temporal term calculates the derivation of  $\phi$  by a linear interpolation between the current time step  $n + 1$  and the previous timestep  $n$ . With  $\Delta t$  as the timestep size the scheme writes

$$\frac{d}{dt}(\phi) = \frac{\phi_{n+1} - \phi_n}{\Delta t}. \quad (2.36)$$

- The  $2^{nd}$  order accurate method consists of a Backward Differentiation Formula (BDF) that takes into account two previous time levels [SK04] is

$$\frac{d}{dt}(\phi) = \left( \frac{3}{2}\phi_{n+1} - 2\phi_n + \frac{1}{2}\phi_{n-1} \right) \frac{1}{\Delta t} = BDF(2). \quad (2.37)$$

- To further increase the accuracy, more time levels can be used. A method using five time levels, based on a linear combination of BDFs with less time levels, is available. With the number in the parenthesis representing the number of previous time levels and  $A$ ,  $B$ ,  $C$  as prefactors which are defined in the documentation of StarCCM+ [Sta], a  $2^{nd}$  order accurate BWD scheme based on five time levels writes

$$BDF(5) = BDF(4) \cdot A - BDF(3) \cdot B + BDF(2) \cdot C. \quad (2.38)$$

### Pressure-Velocity Coupling

For incompressible cases, even though pressure and velocity are intrinsically coupled, an equation for the pressure is not provided. The momentum equations can be solved for the velocities if the pressure field is known, but the continuity equation does not

explicitly contain the pressure. Therefore a pressure field is derived iteratively with a pressure correction.

For compressible cases, the continuity equation could be solved to derive the density and the pressure may be obtained by solving the equation of state  $p = p(\rho, T)$  [VM95]. However a correction of the pressure and subsequently the density is still useful as the field can be constructed to satisfy continuity, thereby stabilizing the scheme. Additionally the use of the pressure correction enables the use of one generalized solver for compressible and incompressible flows.

Two algorithms will be used for pressure-velocity coupling in this work. The SIMPLE algorithm (Semi-Implicit Method for Pressure Linked Equations), introduced by Patankar et Al [PS72] and an extension of the algorithm, the PISO algorithm (Pressure Implicit solution by Split Operator method) [Iss86]. SIMPLE, also referred to as Unsteady Implicit, was originally developed for steady state flows, but additional terms in the pressure correction equation enable it's use for transient flows. A comparison for the procedure of the algorithms is shown in figure 2.2. The flow chart is derived from explanations in [VM95].

The outer loop presents the time stepping. Both algorithms share the first three steps. Initialization is done by guessing the pressure field  $p^*$ . Solving the discretized momentum equations yields the velocity components  $u^*$ . Through the pressure correction equation the pressure correction  $p'$ , representing the difference between the correct and guessed velocities, is calculated. Subsequently the pressure and velocity fields are corrected. Following the SIMPLE algorithm, the convergence criteria are checked, determining the necessity of another loop.

In contrary, PISO features a second corrector step before the convergence is checked. Thereby the pressure and velocity are corrected twice. This leads to increased computational effort. However PISO has numerously proven to be fast and efficient due to the improved convergence.

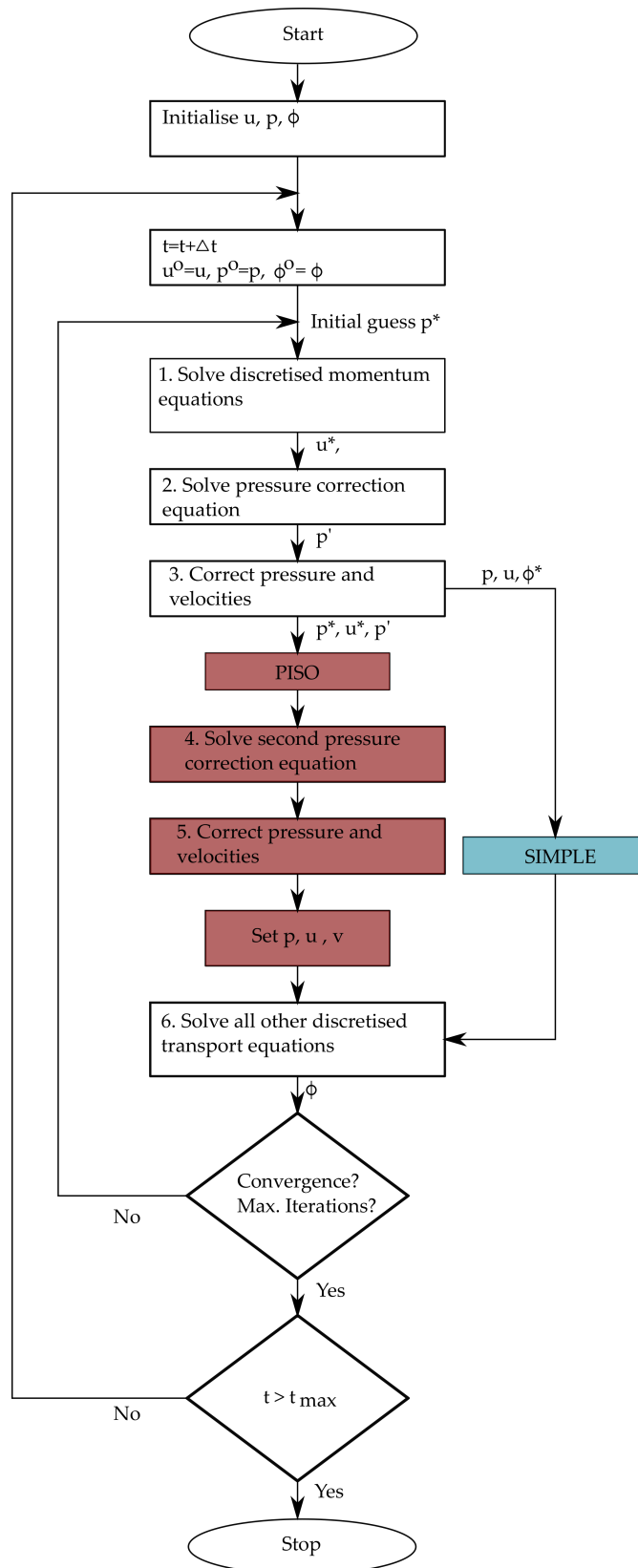


**Figure 2.2:** Solution procedure for the PISO (Red) and the SIMPLE algorithm (Blue)

### 2.1.5 Boundary Conditions

Since acoustics are present in compressible LES calculations, boundary conditions are crucial. Contrary to steady state simulations where waves are not present, special attention has to be taken as an accurate control of the reflections at the boundaries has to be assured [PV05]. Three different boundary conditions at the in- and outlets will be used throughout this work. The goal of this section is just to briefly introduce them. A closer look onto their reflective behavior is taken in section 4.5.

- The **Fixed Velocity Inlet** is applied on the inlet of the test cases. It defines the velocity vector and the scalar properties of the incoming flow.
- The **Fixed Pressure Outlet** is used to define the pressure of the atmosphere into which the flow is exhausted. Backflow can also occur at the boundaries.
- The **Freestream** boundary condition represents the non-reflecting boundary available in StarCCM+ [Sta]. For this far field boundary condition Riemann invariants for a one dimensional flow are introduced. The Riemann invariants for the incoming and outgoing waves are written [Jam14]:

$$R_{\infty} = u_{\infty} - \frac{2c_{\infty}}{\gamma - 1} \quad R_e = u_e - \frac{2c_e}{\gamma - 1} \quad (2.39)$$

With  $u$  and  $c$  representing the extrapolated (e) and the far field ( $\infty$ ) flow velocity and the speed of sound. Adding and subtracting them gives:

$$u_{\infty} = \frac{1}{2}(R_e + R_{\infty}) \quad c = \frac{\gamma - 1}{4}(R_e - R_{\infty}) \quad (2.40)$$

$q_n$  and  $c$  describe the specified far field velocity and speed of sound.

### 2.1.6 Numerical modeling errors

The study of thermoacoustic instabilities which is characterized by propagating acoustic waves requires an accurate treatment of numerical errors introduced by discretization methods. Appropriate guidelines may be derived to perform high-quality LES.

Two types of errors are known to compromise physical wave propagation within a numerical domain. Numerical dissipation manifests in amplitude errors, while numerical dispersion is attributed to phase errors. In Fig. 2.3 both types are exaggerated for a square pulse signal. These errors can result from too large time steps and lead to non-physical effects on turbulent motions, in particular large dissipation as proved in Choi and Moi [CM94]. Incorporating restrictions of the largest time step which are given in terms of CFL number limits thus is a mandatory step towards accurate modeling. The definition of the CFL number is given by:

$$CFL = \frac{u\Delta t}{\Delta x} \quad (2.41)$$

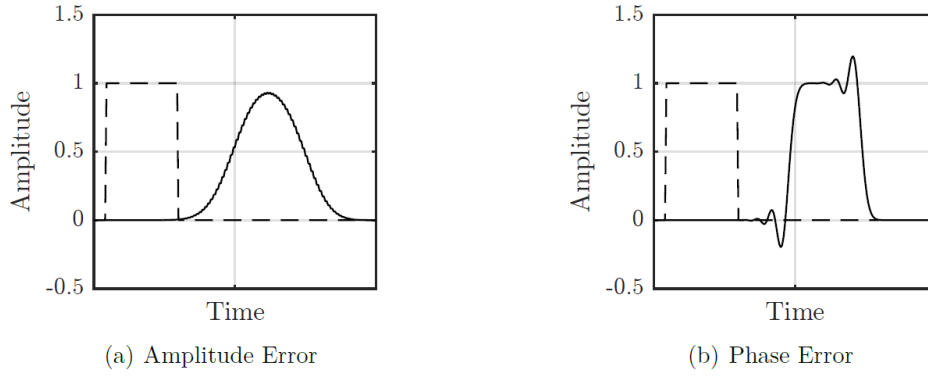


**Figure 2.3:** Visualization of discretization errors due to numerical dissipation (a) and numerical dispersion (b). Dashed Line: Original signal. Solid line: Convected signal [Toe17]

The influence of the CFL number on dispersion and dissipation on an acoustic perturbation has been studied in [Kre12]. Dissipation was negligible for frequencies of interest. Dispersion was too small for to be determined for  $CFL < 4.9$ .

A further source of errors is inextricably linked to mesh resolution and thus always present in LES approaches. The resolved part of the turbulent kinetic energy depends on the grid size. As a consequence, a refinement of the grid also implies a change of physical modeling and is not just affecting numerical elements of the simulation [GF01]. Thus, to assess the physical modelling accuracy, a comparison to benchmark DNS cases is necessary but beyond the scope of this work. Certainly, this will hold for combustion as well. Another way to assess the accuracy of the modeling is offered by specific problems that can be solved analytically. Two cases will be studied in chapter II to test the available settings and discretization methods.

## 2.2 3D Helmholtz Methods

LES is a powerful tool to study combustion instabilities. However, the complexity of the NSE leads to a immense computational effort. Faster methods exist which offer valuable information. Mathematically, the propagation of acoustic perturbations ( $p'$ ) in the limit of small amplitudes in a one dimensional domain can be described according to the linear wave equation for a quiescent fluid [PV05] by

$$\nabla^2 p' - \frac{1}{c_0^2} \frac{\partial^2 p'}{\partial t^2} = 0. \quad (2.42)$$

In absence of mean flow and assuming harmonic oscillations, solving the wave equation yields the (one-dimensional) acoustic field given by a rightward and a leftward travelling wave. If both waves exist simultaneously, the superposition of two travelling waves leads to interference patterns in the disturbance amplitude [Lie+01b]. This phenomenon is referred to as standing waves characterized by

spatially periodic oscillation amplitudes. An important feature of standing waves is a 90° phase difference between pressure and displacement velocity [Toe17].

To determine the shape of the standing wave, the wave equation is conveniently recast into the the Helmholtz equation making use of the harmonic approach with complex notation for pressure  $p' = \hat{p}e^{-i\omega t}$ . With  $\hat{p}$  as a complex number and  $\omega = 2\pi f$  the Helmholtz equation reads

$$\nabla^2 \hat{p} + \left(\frac{\omega}{c_0}\right)^2 \hat{p} = 0. \quad (2.43)$$

Based on the Helmholtz equation the eigenmodes and eigenforms of the system can be found. These constitute (along with the phase relation of pressure and velocity) the solution set of theoretical mode shapes which may be observed within the domain of interest. The corresponding frequencies can be determined analytically for simple geometries or numerically for more complex systems, e.g. gas turbine combustors [PV05].

COMSOL Multiphysics is used in this work to determine the mode shapes and frequencies based on the Helmholtz equation.

## 2.3 Postprocessing

### 2.3.1 Two-microphone Method

To analyze the reflection properties of boundaries or openings different methods are known. In this work, the two-microphone method proposed e.g. by Munjal et Al. [MD90] has been used. Compared to previous methods [CB80b] [CB80a], mean flow effects are incorporated by Munjal. Based on pressure signals of two microphones, forward and backward traveling waves in a duct are separated.

The reflection coefficient is calculated by

$$R = \left( \frac{H_{12}e^{-\beta Mas} - e^{2\beta L}}{e^{\beta s} - H_{12}e^{-\beta s}} \right) e^{2\beta L}, \quad (2.44)$$

where  $Ma$  represents the Mach number to incorporate the mean flow effects,  $s$  is the distance between both probe points and  $L$  the distance from the farthest probe to the chosen measurement plane.  $H_{12}$  is the transfer function that is defined as

$$H_{12} = \frac{p_1}{p_2} \quad (2.45)$$

and  $\beta$  is calculated based on

$$\beta = \frac{ik}{(1 - M^2)} \quad \text{using} \quad k = \frac{2\pi f}{c(1 - M^2)}. \quad (2.46)$$

An exemplary set of microphones is displayed in figure 2.4.

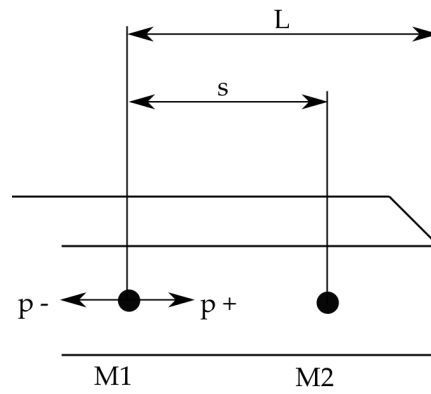


**Figure 2.4:** Schematic of the setup for the two-microphone test

The Two-microphone method will be used in section [4.4](#) to analyze the reflection magnitude and phase for the boundary conditions available in StarCCM+.





## **Part II**

# **Assessment of Numerical Accuracy and Boundary Conditions**



In this chapter simplified test cases are used to assess the numerical accuracy and the impact of boundary condition treatment in StarCCM+.

At sufficient temporal resolution, diffusion and dispersion of convective [RKH67] and acoustic waves is of major importance for the accurate prediction of thermoacoustic instabilities.

In the first test case (Section 3) the convection of a vortex is analyzed for different numerical schemes with respect to diffusion and dispersion. Then, in the second test case (4.2), the impact of numerical settings on the propagation of an acoustic wave is investigated.

Furthermore, proper acoustic boundary treatment is crucial for the CFD of thermoacoustics. Unphysical acoustic reflections at the boundaries can influence the results and should be avoided [WMD06]. Therefore the impact of the BC on the reflection of acoustic waves is studied (Section 4.4).

In industrial CFD, and especially LES, not only the accuracy of a CFD code but also the CPU time is important in order to deliver accurate results in a reasonable time. Therefore, the CPU time of the different numerical schemes is also considered in section 3. In addition, the scalability of StarCCM+ is tested by expanding the test of section 3. Calculations with different numbers of CPU's were performed on the Siemens cluster.



## Chapter 3

# Vortex Preservation

### 3.1 Case Description

The first test investigates the numerical dissipation and dispersion of the code considering the preservation of a vortex [Vor].

The rectangular computational domain with a side length of  $L = 0.312$  m (Fig. 3.1) consists of a two-dimensional, structured mesh with 6400 cells. All the boundaries are periodic, simulating the convection of the vortex in an infinite duct. A flow without viscosity and thermal conductivity is assumed. Thereby reducing the NSE to the Euler equations becomes possible by linearization [Pop].

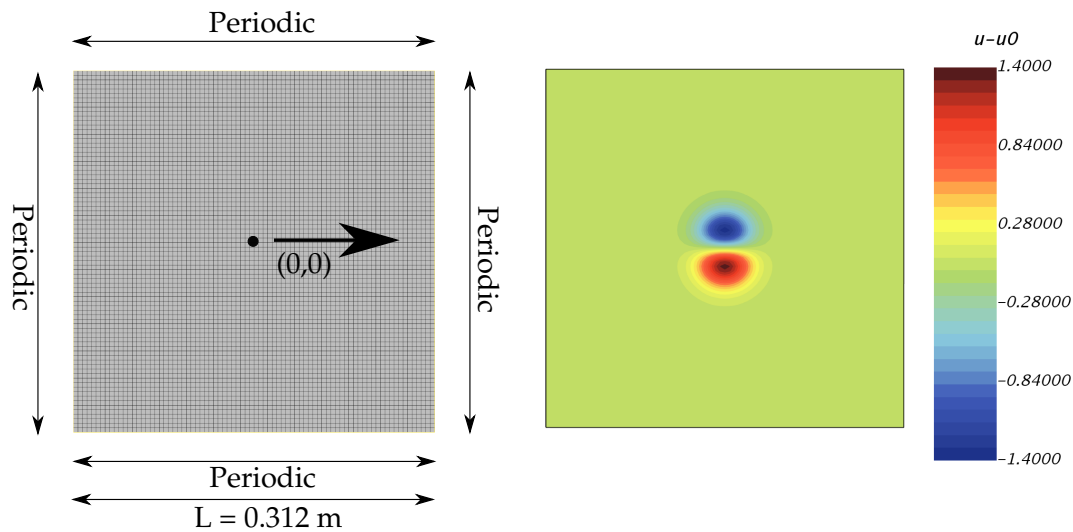


**Figure 3.1:** Computational domain of the vortex preservation test (left) and the initialized vortex (right) displayed as  $u - u_0$

The vortex is initialized based on the potential  $\Psi$  of the vortex:

$$\Psi = \Gamma e^{-\frac{(x-x_c)^2 + (y-y_c)^2}{2R_c^2}} \quad (3.1)$$

The x- and y-velocities write:

$$u_x = u_0 + \frac{\delta \Psi}{\delta y} \quad (3.2)$$

**Table 3.1:** Initial conditions of the vortex and the flow field

$u_0$	$35 \text{ m s}^{-1}$
$T_0$	300 K
$p_0$	101 300 Pa
$\rho_0$	$1.1717 \text{ kg m}^{-3}$
$\Gamma$	$0.035 915 7 \text{ m}^2 \text{ s}^{-1}$
$R_c$	0.015 56 m
$x_c$	0
$y_c$	0

$$u_y = -\frac{\delta\Psi}{\delta x} \quad (3.3)$$

The initial pressure field is given by:

$$p - p_0 = -\frac{\rho\Gamma^2}{2R_c^2} e^{-\frac{(x-x_c)^2+(y-y_c)^2}{2R_c^2}} \quad (3.4)$$

The flow quantities are given in table 3.1. The center of the initial vortex is located at position  $(0, 0)$ . The mean velocity of the flow corresponds to a Mach number of  $Ma = 0.1$ .

## 3.2 Numerical Accuracy

A selection of the calculations which were performed are listed in table 3.2. All the calculations are done using implicit time stepping as explicit time stepping is not supported for LES in StarCCM+.

**Table 3.2:** Numerical settings for the vortex preservation test case

Algorithm	Coupled/ Segregated	Spatial Dis- cretization	Temporal Discretiza- tion
UI	C	$2^{nd}$ order	$2^{nd}$ order
UI	C	$3^{rd}$ order	$2^{nd}$ order
UI	S	$2^{nd}$ order	$1^{st}$ order
UI	S	$2^{nd}$ order	$2^{nd}$ order
UI	S	$2^{nd}$ order	$2^{nd}$ order (5)
UI	S	$3^{rd}$ order	$2^{nd}$ order
PISO	S	$2^{nd}$ order	$1^{st}$ order
PISO	S	$3^{rd}$ order	$1^{st}$ order

Calculations are done using the Unsteady Implicit (UI) and the PISO algorithm for both the coupled (C) and segregated (S) solver. For PISO only  $1^{st}$  order accurate

temporal discretization is implemented in StarCCM+. For Unsteady Implicit 1<sup>st</sup> and 2<sup>nd</sup> order BWD are available. Additionally, the 2<sup>nd</sup> order BWD scheme can be extended to use 5 time levels. Spatial discretization is varied between 2<sup>nd</sup> order bounded central and the 3<sup>rd</sup> order Muscl scheme.

In terms of accuracy the results of the coupled and the segregated solver did not show substantial differences. Therefore the emphasis is put on the segregated solver as the computational time is lower compared to the coupled solver (Sec. 3.3) and less memory is used [Sta].

Two different time step sizes were investigated. The timesteps corresponded to a convective  $CFL = 0.7$  and an acoustic  $ACFL = 0.7$ . As differences between the time step sizes were marginal they will not be presented visually. Table 3.2 and the upcoming graphs show results of calculations with a time step corresponding to  $CFL = 0.7$ .

Fig. 3.2 shows the contour plots of  $u - u_0$  for 6 different cases. The PISO and the unsteady implicit algorithm are compared using the 2<sup>nd</sup> and 3<sup>rd</sup> order spatial schemes. It has to be noted that the exact result would equal the initial vortex without deformation as calculations are done without viscosity. However, all the simulations dissipate the vortex over time, but in general, the behavior of the simulations using the 1<sup>st</sup> order BWD scheme is more dissipative than the calculations of the unsteady implicit algorithm with 2<sup>nd</sup> order BWD.

For the simulations with 1<sup>st</sup> order BWD (figure 3.2 a-c) changing the spatial discretization or the algorithm does not change the results.

The Unsteady Implicit algorithm is able to preserve the convected vortex over a longer time period if 2<sup>nd</sup> order temporal discretization is used. But for this algorithm, the results show a difference between the 2<sup>nd</sup> and 3<sup>rd</sup> spatial discretizations. Even though the Muscl scheme seems to preserve the initial vortex even better than the bounded central scheme for the first flow through times other vortices are introduced. These vortices have an opposed rotational direction in comparison to their neighbours. The effect is also visible in the 2<sup>nd</sup> order calculations but it is weaker.

The best result in terms of the vortex preservation is achieved using the unsteady implicit algorithm with a BWD scheme based on 5 time levels.

Fig. 3.3 gives further insight into the results of the different cases already presented in fig. 3.2. The y-velocity  $v$  is investigated on the central axis ( $y = 0$ ) of the domain. For orderliness only the PISO result using the bounded central scheme is used to represent the calculations with a 1<sup>st</sup> order temporal discretization as results hardly differ for the other two calculations. The stronger dissipative effect of the low order simulations is clearly visible over the flow through time. Already after one flow through time the amplitude gets damped down to less than 25%.

The graph highlights the vortices that are introduced with the 3<sup>rd</sup> order scheme using the Unsteady Implicit algorithm and visualizes the accuracy of the 5 level BWD scheme.

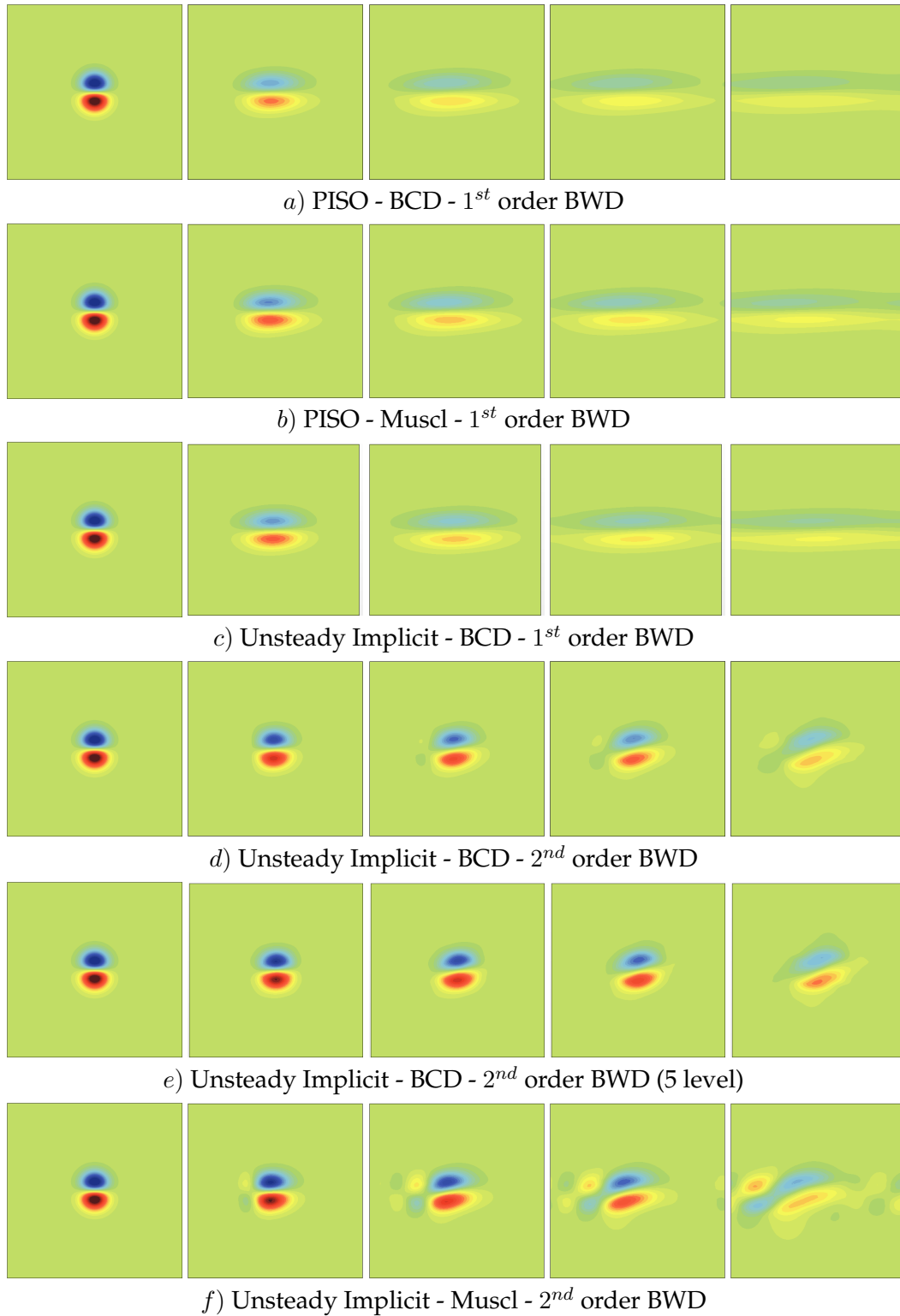


**Figure 3.2:** a) - f): Contour plots for different settings of  $u - u_0$  for the initial flow field and after 1, 3, 5 and 10 flow through times. Notation: Algorithm - Spatial Discretization - Temporal Discretization



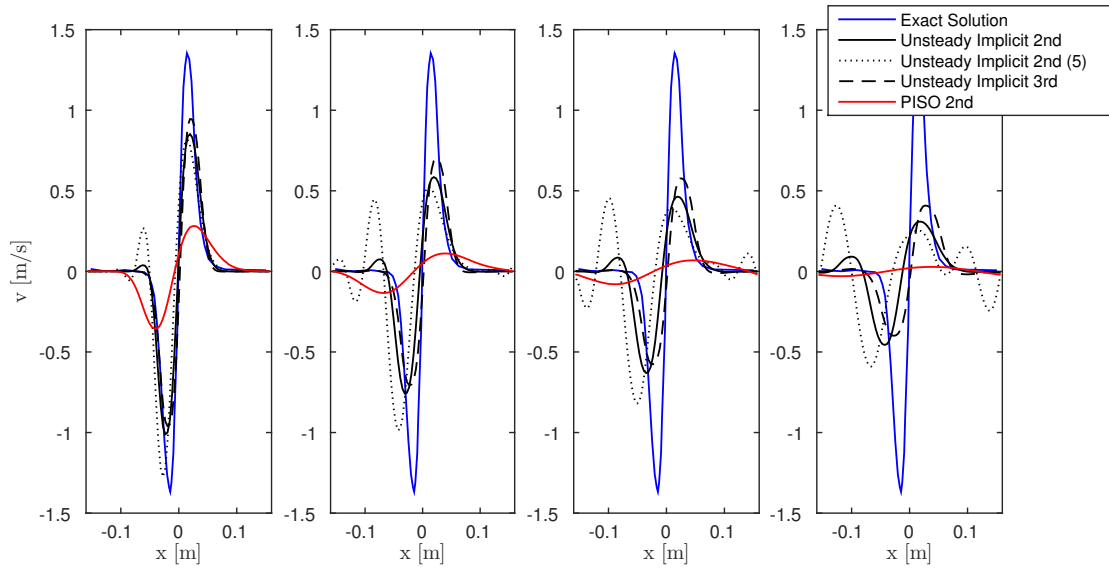


**Figure 3.3:** Velocity  $v$  of the exact result (blue), the PISO algorithm (red) and the Unsteady Implicit algorithm (black) for  $y = 0$  after 1, 3, 5, 10 flow through times. The order specifies the spatial discretization, the parenthesis the time levels of the BWD scheme

### 3.2.1 Numerical accuracy in comparison to other codes

A comparison to other codes is done in fig. 3.4 for the  $y$ -velocity after 20 and 40 flow through times. Data for OpenFOAM, AVBP and the YALES solver is taken from CERFACS[Vor]. The numerical schemes used in those solvers are displayed in table 3.3.

**Table 3.3:** Settings of AVBP, YALES and OpenFOAM

Solver	Spatial Discretization	Temporal Discretization
AVBP	3 <sup>rd</sup> order	3 <sup>rd</sup> order
YALES	4 <sup>th</sup> order	4 <sup>th</sup> order
OpenFoam	4 <sup>th</sup> order	2 <sup>nd</sup> order
StarCCM+	2 <sup>nd</sup> order	2 <sup>nd</sup> order

The higher order codes, particularly AVBP, are able to preserve the vortex for a longer time. This effect of the order of discretization has been noted in the previous investigations of this chapter already. Especially the temporal discretization shows a high influence. However, even though high numerical schemes are used, YALES and OpenFOAM show a visible dissipative effect. The result representing the calculations done in StarCCM+ corresponds to the 3 level BWD results of the Unsteady Implicit algorithm using bounded central spatial discretization.

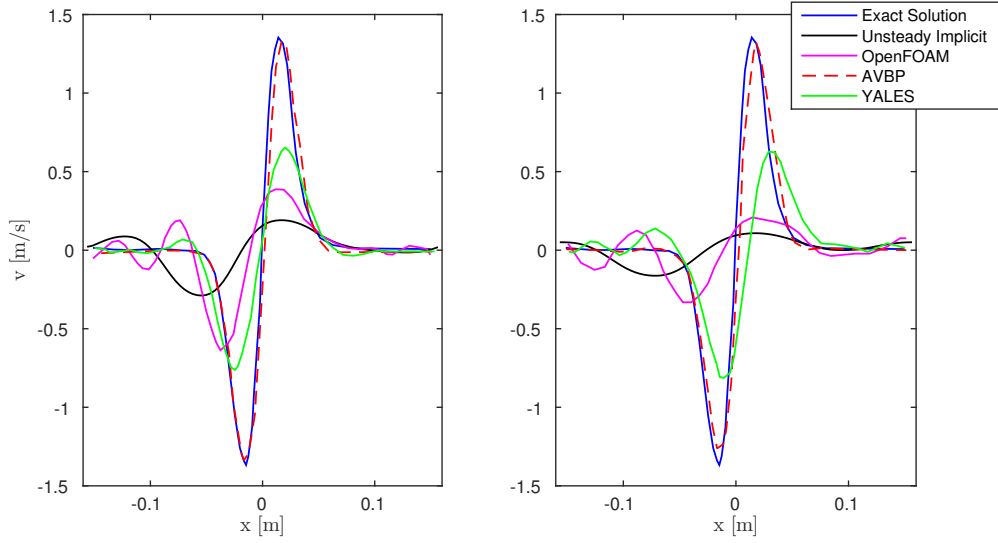


**Figure 3.4:** Velocity  $v$  of the exact result (blue), the Unsteady Implicit algorithm in StarCCM+ (black), Open Foam (magenta), AVBP (red dashed) and YALES (green) for  $y = 0$  after 20 and 40 flow through times [Vor]

### 3.3 Computational Time

An important point in the industrial application of CFD is the computational time. This section aims to present the influences of the different numerical schemes on the run time. The computational time is evaluated per timestep. As this time is not constant, a mean value over a simulation time of  $0.3s$  is presented.









Comparing the computation times between the PISO and the Unsteady Implicit algorithm is not straightforward. The details of the algorithms can be found in section 2.1.4. In short, the computation time depends heavily on the settings used in the algorithms.

For Unsteady Implicit, the number of inner iterations is based on tests investigating the asymptotical behavior of a solution during a timestep. A number of 8 inner iterations has been found to be appropriate.

For the PISO algorithm, different settings of the PISO residual reduction and the maximum PISO correctors have been tested. The two stopping criteria were swept between 10-30 maximum PISO correctors and 1%-3% residual reduction respectively. No substantial difference in accuracy has been found by reducing the residual reduction for more than 2.5% and the correctors for more than 20. The listed calculations in table 3.2 and 3.4 correspond to these values.

In general, the coupled solver needed about 40% more time to solve the equations for one time step compared to the segregated solver. For UI, changing between the 1<sup>st</sup> and 2<sup>nd</sup> order BWD leads only to small differences in computational time. However, high-accuracy temporal discretization using 5 time levels increases the computational time by more than 50% compared to the standard 3 level BWD scheme. Using the

**Table 3.4:** Computational time for the Vortex Preservation test case.  
 Notation: Algorithm, segregated or coupled solver, spatial discretization, temporal discretization and computational time [ $\frac{s}{\Delta t}$ ]

UI	C	2 <sup>nd</sup>	2 <sup>nd</sup>		0.14s
UI	C	3 <sup>rd</sup>	2 <sup>nd</sup>		0.18s
UI	S	2 <sup>nd</sup>	1 <sup>st</sup>		0.09s
UI	S	2 <sup>nd</sup>	2 <sup>nd</sup>		0.10s
UI	S	2 <sup>nd</sup>	2 <sup>nd</sup> (5)		0.16s
UI	S	3 <sup>rd</sup>	2 <sup>nd</sup>		0.13s
PISO	S	2 <sup>nd</sup>	1 <sup>st</sup>		0.06s
PISO	S	3 <sup>rd</sup>	1 <sup>st</sup>		0.08s

Muscl scheme as spatial discretization increases the computation time about 25% for each set of settings. The PISO solver was noticeable faster than the Unsteady Implicit solver reducing the computational time around 30%.



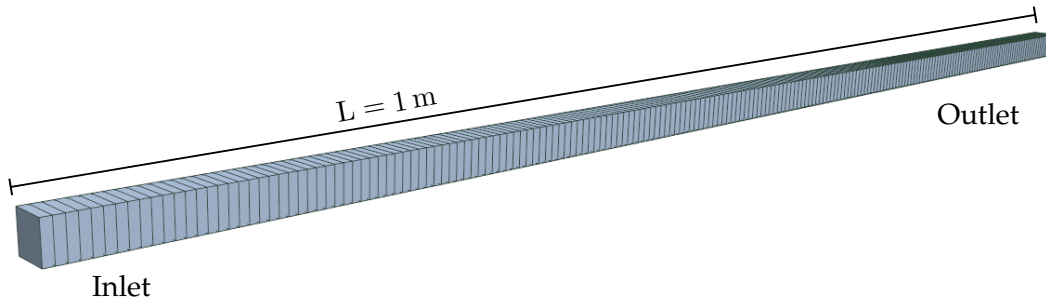
## Chapter 4

# Acoustic Wave Propagation

In this test the propagation of an acoustic perturbation is studied. First, based on the insights in section 3, selected numerical settings are investigated in terms of the capability to predict the right amplitude and speed of the wave. In the second part emphasis is put onto the treatment of the boundary conditions.

### 4.1 Case Description

A 1-D duct (Figure 4.1) with  $L = 1$  m and a cell count of 200 cells is initialized with a mean flow and an initial perturbation in velocity and pressure. An inviscid flow regime is investigated, thereby reducing the NS-equations to the Euler equations. The acoustic perturbation travels with the speed of sound (Fig. 4.2) and, depending on the boundary conditions, gets reflected or leaves the domain .



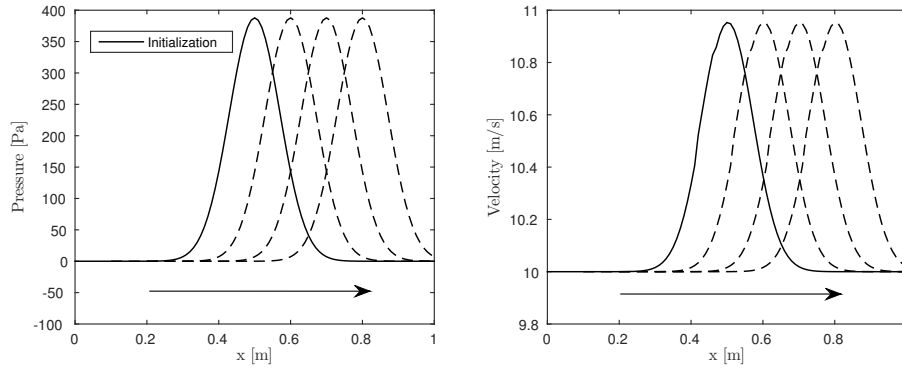
**Figure 4.1:** Computational domain of the acoustic perturbation test

Table 4.1 shows the flow variables for the initial flow field. The reference pressure corresponds to atmospheric conditions. A mean flow with a velocity  $v = 10 \text{ m s}^{-1}$  is introduced. The gaussian perturbation is initialized following:

$$p' = P' \exp\left(-\frac{(x-x_0)^2}{\sigma^2}\right) \quad (4.1)$$

$$u' = \frac{p'}{\rho_0 c_0} \quad (4.2)$$

The time step is set according to  $ACFL = 0.7$ .

**Figure 4.2:** Wave propagation through the domain**Table 4.1:** Flow variables of the wave propagation test

$u_{mean}$	$10 \text{ m s}^{-1}$
$P'$	388 Pa
$p_{ref}$	101 300 Pa
$x_0$	0.5 m
$\sigma$	0.1
$c_0$	$346 \text{ m s}^{-1}$
$\rho_0$	$1.16 \text{ kg/m}^3$

## 4.2 Numerical Accuracy

To determine the numerical accuracy fixed value boundary conditions are used:

- Inlet: Fixed velocity (velocity ( $v' = \text{m s}^{-1}$ ) and temperature imposed)
- Outlet: Fixed pressure (pressure ( $p' = 0 \text{ Pa}$ ) and temperature imposed)

For the fixed velocity inlet and the fixed pressure outlet, three different settings (Tab. 4.2) were tested to compare the behavior of PISO and Unsteady Implicit faced with an acoustic perturbation. Also the influence of time levels studied in the backward differentiation scheme was investigated for the Unsteady Implicit algorithm. For PISO the only option, 1<sup>st</sup> order BWD, is used.

**Table 4.2:** Completed calculations for the numerical accuracy of the wave propagation

	Spatial Discretization	Temporal Discretization
PISO	2 <sup>nd</sup> order	1 <sup>st</sup> order
UI	2 <sup>nd</sup> order	2 <sup>nd</sup> order (3-level)
UI	2 <sup>nd</sup> order	2 <sup>nd</sup> order (5-level)

Figure 4.3 shows the evolution of the maximum and minimum pressure and velocity in the domain over the computation time for the PISO and Unsteady Implicit algorithm using the 3-level BWD scheme.

The calculation was done until  $t = 0.115$  s, corresponding to 40 reflections. For an exact result the amplitudes would be constant over the time due to the assumption of an inviscid flow. However, decreasing max/min values of the velocity and pressure indicate the dissipation of the algorithms. Endorsing the results of the previous vortex preservation case, the amplitudes of the PISO algorithm decrease faster than those using the Unsteady Implicit algorithm.

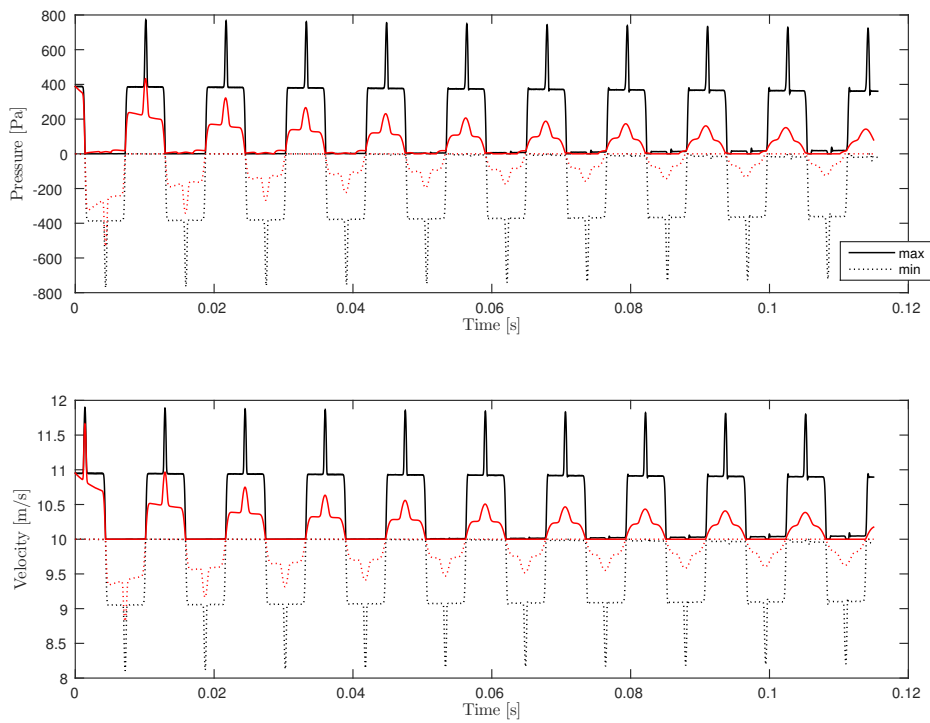


**Figure 4.3:** Min. and max. pressure and velocity for Unsteady Implicit (black) and PISO (red) in the computational domain

Comparing the results after 40 reflections, fig. 4.4 gives a detailed view on the differences. The PISO algorithm is not able to preserve the acoustic perturbation. The shape is hardly conserved with an amplitude lower than 25% compared to the initial amplitude. The Unsteady Implicit algorithm is able to preserve the perturbation accurately. However, low dissipation and a slight misprediction of the traveling velocity is present. In front of the primary perturbation a wiggle is introduced. This wiggle indicates dispersion (Sec. 2.1.6). Using the 5-level BWD scheme shows the best results in terms of the traveling velocity and the dissipation. Also, no wiggle is visible.

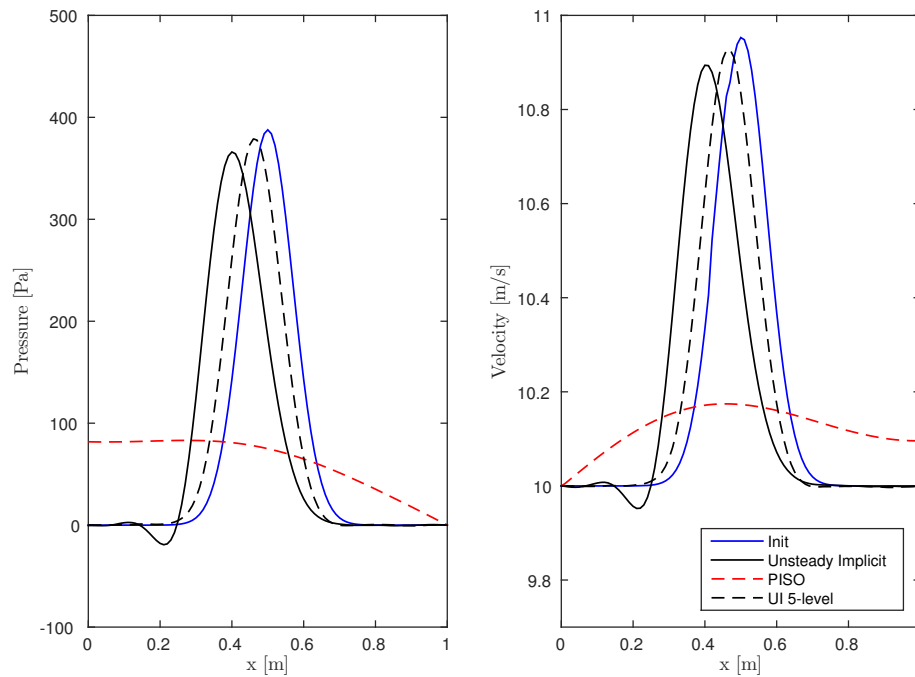


**Figure 4.4:** Comparison of the acoustic perturbation for PISO and Unsteady Implicit after 40 reflections

### 4.3 Computational Time

The trend of the computational time is similar to the vortex preservation test with Unsteady Implicit needing approximately 50% more computational time per timestep. Using 5 instead of 3 levels increases the computational time for another 30%. The influence of the settings on the computational time was already discussed in the last chapter. The same settings in terms of inner iterations, corrector steps and residual reduction are used here.

**Table 4.3:** Computational time for the wave propagation test case. Notation: Algorithm, spatial discretization, temporal discretization and computational time [ $\frac{s}{\Delta t}$ ]

PISO	2 <sup>nd</sup>	1 <sup>st</sup>		0.02s
UI	2 <sup>nd</sup>	2 <sup>nd</sup> (3)		0.03s
UI	2 <sup>nd</sup>	2 <sup>nd</sup> (5)		0.04s

### 4.4 Boundary Condition Treatment

Now, instead of a fixed pressure outlet, the so-called freestream boundary is used (Sec. 2.1.5), which is supposed to be non-reflecting. For acoustic simulations non-reflecting



boundaries are mandatory as fluctuating pressure and flow structures that penetrate the boundaries can lead to reflections. These reflections interact with the upstream flow and therefore can lead to a physically unrealistic flow [PV05].

**Table 4.4:** Completed calculations for the assessment of the boundary condition treatment

	Outlet Condition	Mach Number
UI	Freestream	0.0288
UI	Freestream	0.03

Two different calculations are performed to investigate freestream boundary condition (Tab. 4.4). Both use the Unsteady Implicit algorithm. The simulations only differ in terms of the Mach number which is imposed at the outlet.

For the freestream boundary, if the Mach number is set to  $Ma = 0.0288$ , the exact value for the mean flow, no reflection is detected (Fig. 4.5). The perturbation travels through the domain, and when reaching the boundary the perturbation leaves the domain. The pressure in the domain remains constant.

However, a strong sensitivity to the Mach number is observed as shown in figure 4.6. If using a Mach number that does not correspond to the mean flow, directly at the beginning a pressure and velocity perturbation is introduced at the outlet.

The perturbation travels through the domain, interacts with the initialized perturbation, and hits the inlet. As the inlet has a fixed velocity ( $v' = 0 \text{ m s}^{-1}$ ), the velocity perturbation is transformed and added to the pressure perturbation. Then the perturbation travels back to the outlet where it leaves the domain without reflection. The pressure decreases about 200 Pa from the reference pressure which is imposed at the outlet.

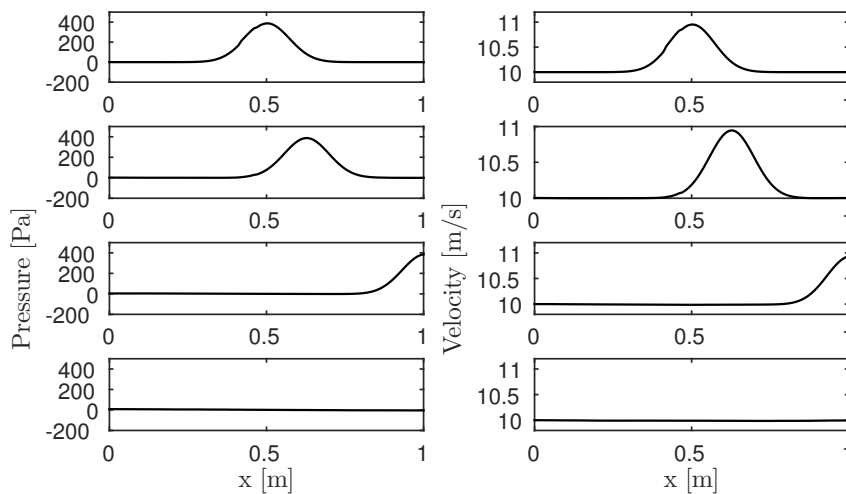


**Figure 4.5:** Velocity and pressure after 0, 40, 160 and 320 timesteps in the domain for  $M = 0.0288$

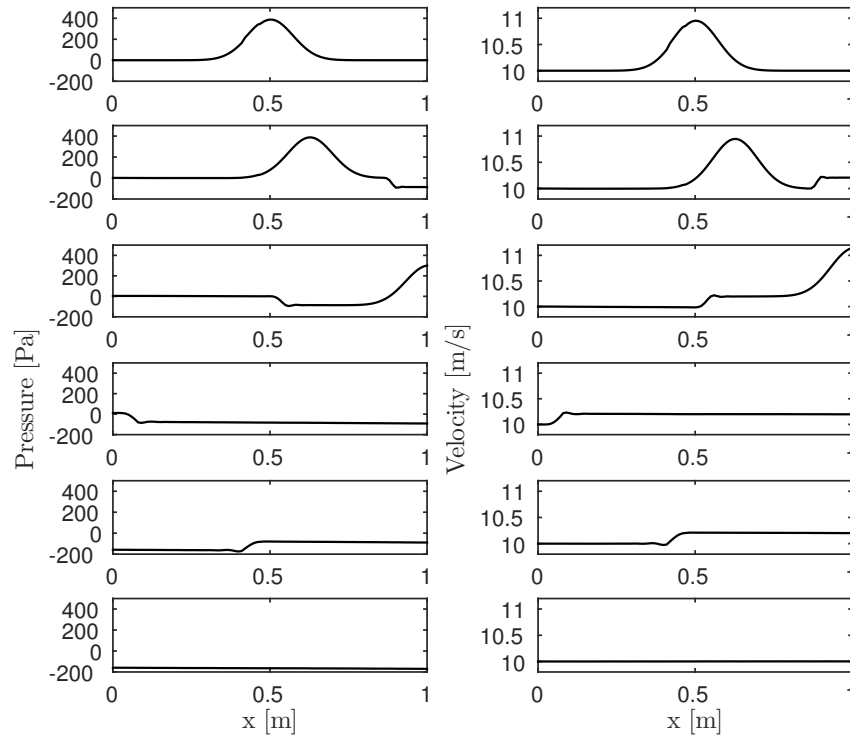


**Figure 4.6:** Velocity and pressure after 0, 40, 160, 320, 480 and 720 timesteps in the domain for  $M = 0.3$

## 4.5 Two-microphone method

In the previous subsection the propagation of an acoustic wave has been investigated. Even though, the reflective and non-reflective behavior of the boundary conditions was determined, emphasis was put onto the accuracy as the boundaries were only perturbed by one frequency. In order to determine the reflection coefficient magnitude and phase, the two-microphone method, introduced in section 2.3.1, is used.

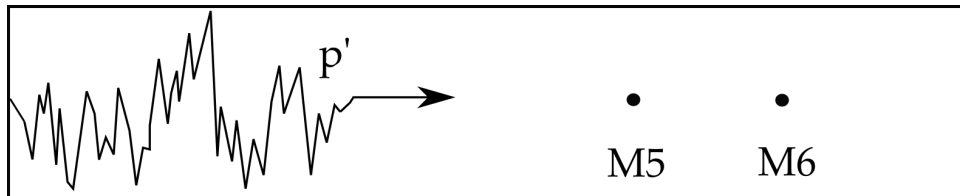


**Figure 4.7:** Exemplary pressure perturbation travelling in the duct

For each boundary condition, a white noise signal is created in Matlab, applied to the inlet (or to the outlet to test the inlet) and the reaction of the boundary condition is observed. An example of a perturbation in the 1-D duct is shown in figure 4.7. The white noise signal gives a constant power spectral density while fluctuating at different frequencies. To provide a data base for this test, 6 probe points to monitor

the pressure were applied to the 1-D duct. Table 4.5 shows the analytically derived reflection coefficients for the corresponding boundaries [PV05].

**Table 4.5:** Analytically derived reflection magnitude and phase [PV05]

	Boundary Condition	Magnitude	Phase
Velocity Inlet	$u' = 0$	1	$0^\circ$
Pressure Outlet	$p' = 0$	1	$180^\circ$
Freestream	Non Reflecting	0	-

To perturbate the velocity inlet, a fluctuating pressure based on the white noise from Matlab was imposed on the pressure outlet. These perturbations travel through the domain, pass the microphones and get reflected at the inlet. The result in terms of the pressure evolution for the microphone 1+2 is shown on the left side of figure 4.8 for the timespan of  $0.01 \text{ s} < t < 0.02 \text{ s}$ . The right side confirms the analytical results from table 4.5. The perturbations get reflected fully ( $R = 1$ ) and the phase is constant and zero.

On the other side, for the pressure outlet, white noise was imposed onto the velocity inlet boundary condition. The pressure evolution and reflection coefficient magnitude/phase for the pressure outlet confirms the analytical results (Fig. 4.9). The perturbation gets fully reflected but in contrast to the velocity inlet the phase change is  $180^\circ$ .

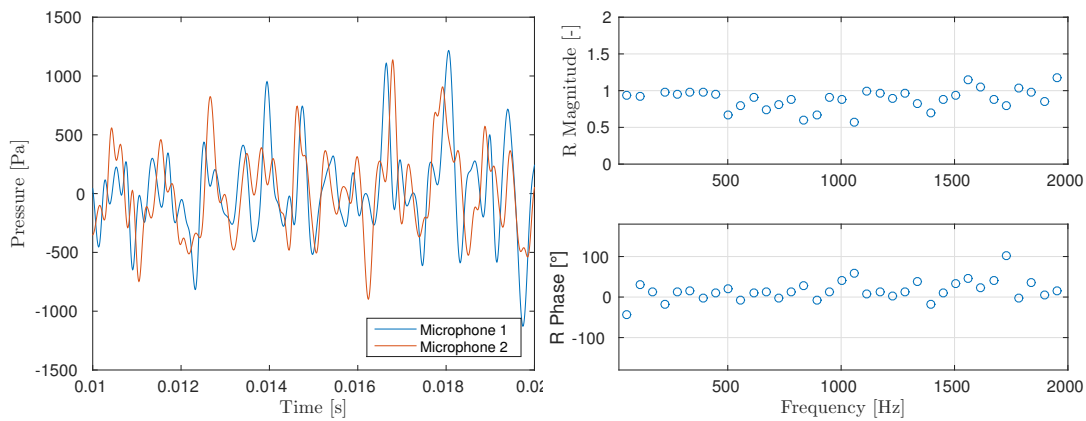


**Figure 4.8:** Pressure signal of M1 ( $x = 0.1 \text{ m}$ ) and M2 ( $x = 0.2 \text{ m}$ ) and the reflection coefficient magnitude and phase for the velocity inlet

Fig. 4.10 shows the reflection coefficient magnitude for the freestream outlet perturbed by white noise. No reflection is detected for the freestream outlet. Note that the plot of the reflection phase coefficient is not of value here as the magnitude of the reflection is zero.

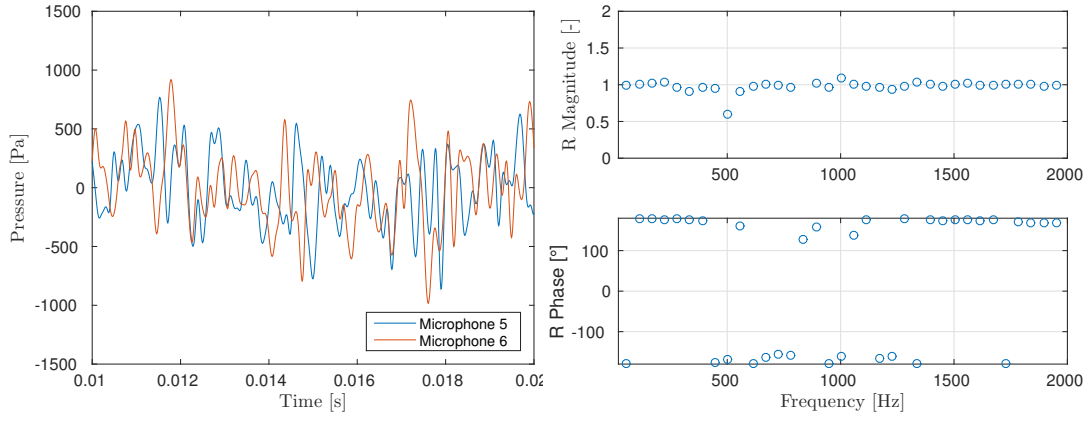


**Figure 4.9:** Pressure signal of M5 ( $x = 0.8$  m) and M6 ( $x = 0.9$  m) and the reflection coefficient magnitude and phase for the pressure outlet

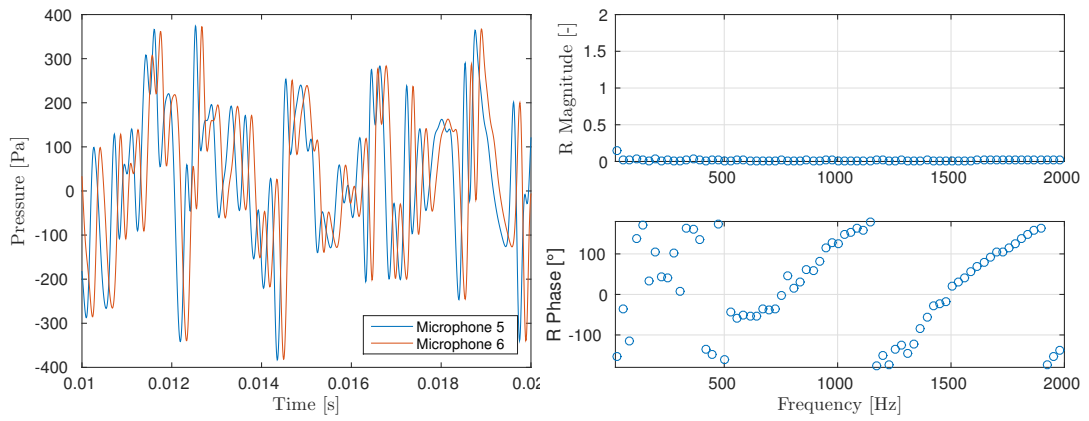


**Figure 4.10:** Pressure signal of M1 ( $x = 0.75$  m) and M2 ( $x = 0.9$  m) and the reflection coefficient magnitude and phase for the freestream boundary condition

## Chapter 5

# Performance

The vortex preservation test is converted into 3-D to test the performance and scalability of the code. Relating it to CFD, scalability describes the ability to decrease the computation time by adding more processors to a simulation [ERAEB05]. This is mandatory to run computationally sophisticated LES calculations as the only way to make them temporally feasible, is to run them on numerous processors. However, using parallel computing increases the message passing between the processors. The goal of this section is to find an optimal ratio of  $\frac{Cells}{Processor}$  without wasting computational resources.

To test this, the grid is expanded into z direction. The new mesh dimension is  $120 \times 120 \times 120 = 1728000$  cells. Time step size is kept to  $\delta t = 0.000\,072\,8\text{ s}$  imposing  $CFL = 0.7$  and the Implicit Unsteady algorithm is applied. Runs are made with 24, 48, 72, 96, 120 CPU's on the Siemens cluster. Afterwards, the speedup  $Su$  [Rah94] is calculated following equation 5.1:

$$Su = \frac{t_0}{t_N} \quad (5.1)$$

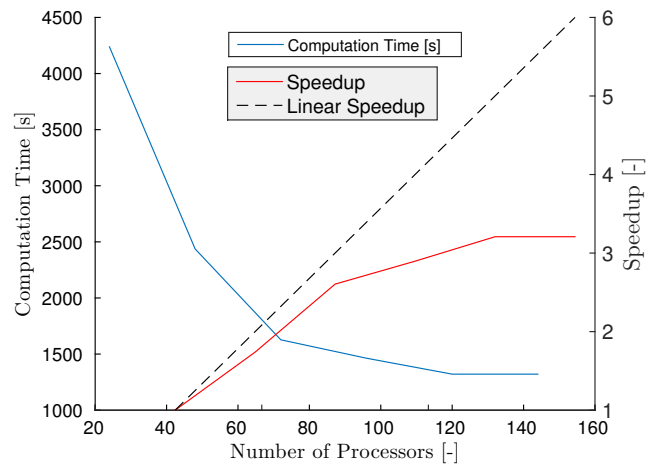
$t_0$  corresponds to the execution time for 24 processors and  $t_N$  to the execution time for N processors. The speedup factor is a simple measure to analyze parallel computing, as it just compares the execution time for N processors.

Fig. 5.1 shows the calculation time, Speedup factor and the linear Speedup factor over the number of processors. The linear Speedup factor corresponds to a linear decrease in terms of computation time, meaning that:

$$\frac{t_0}{t_N} = \frac{N_0}{N} \quad (5.2)$$

This is generally not possible because an increase of message passing is inevitable for CFD calculations.

For this test case the Speedup factor is pretty close to the ideal linear Speedup up to a number of 72 processors. This corresponds to 25000 cells per processor. But then the gradient starts to decrease. This trend can be seen in the decrease of the computational time as well. A minimum is reached with 120 processors. Probably the computational time would even increase again with more processors as the message passing increases further.



**Figure 5.1:** Calculation time, Speedup factor and the linear Speedup factor over the number of processors using the Unsteady Implicit algorithm

## Chapter 6

# Conclusion of the test cases

Different test cases have been analyzed to investigate the performance of StarCCM+ for key capabilities of a code to predict thermoacoustic instabilities.

Giving a broad data base, sections 3 and 4 studied the numerical accuracy of different settings in StarCCM+. No substantial difference was found in terms of accuracy between the segregated and coupled solver.

The PISO results for both cases showed a stronger dissipative behavior than the calculations using the Unsteady Implicit algorithm and were not able to preserve the vortex and the acoustic perturbation accurately. This behavior can be explained by the lack of options to choose higher order temporal schemes. Unsteady Implicit calculations based on the 1<sup>st</sup> order BWD showed the same trends.

The calculation time is heavily dependent on the different stopping criteria of the solvers. After tuning the criteria to a satisfying degree of convergence in the loops, PISO converged approximately 1.5 times faster than Unsteady Implicit. For Unsteady Implicit the calculation time was insensitive to the order of temporal discretization, only the switch from 3 to 5 time levels lead to an increase of 50 %.

Varying the spatial scheme did not have an influence on the PISO algorithm. However a difference was detected for the Unsteady Implicit algorithm. New vortices were generated using the Muscl scheme. Using the second order bounded central scheme, these vortices were hardly visible.

The time levels for the backward differentiation schemes have an impact on the accuracy of the results. However regarding the increase of computational time by a factor of 35 % for the acoustic perturbation and 50 % for the vortex preservation does not justify the use of higher level BWD.

Even though they show a dissipative effect, the best results, representing a trade of in terms of accuracy and computational effort, were achieved with the 2<sup>nd</sup> order bounded central and the 3-level BWD scheme using the Unsteady Implicit algorithm. Subsequently this combination will be used for further calculations.

In terms of boundary conditions the fixed value boundary conditions showed the expected reflecting behavior. The freestream boundary condition showed no reflection for the correct mach number but proved to be sensitive for derivations. Obviously it is a simple task to tune the mach number in a 1-D flow but it has to be

pondered if reflections can be prevented for an unsteady 3-D case. This will be tested in the following chapter.

The performance test showed that the minimum cell count per core should not be below 25000 cells per core.



## **Part III**

# **The Volvo Validation Rig**



## Chapter 7

# Introduction

In the previous chapter the propagation of convective and acoustic waves was analyzed for different numerical settings and the impact of boundary condition treatment on acoustics was investigated. Now the knowledge will be transferred to the academic Volvo configuration which provides an experimental database.

At first, the setup of the Volvo validation rig is introduced and the literature is reviewed. As a second step, the RANS settings and the results for a non reactive and a reactive operating point are presented. In the third chapter, an acoustic analysis performed with Comsol Multiphysics is introduced to derive the chamber modes of the combustor. The final chapter comprises the main part of this work. LES of the Volvo validation rig are performed and their settings explained. The non reactive operating point is validated to determine the capabilities of StarCCM+ to predict unsteady flow patterns. Subsequently, turbulence-combustion interaction and combustion modeling are investigated for the first reactive operating point. Results are compared to the RANS simulations and experiments. Targeting the thermoacoustics, the last step is to study different operating points of the combustor. Low frequency longitudinal acoustics are investigated for the first unstable operating point. Different simulations are done to evaluate whether StarCCM+ is able to predict the trend of stronger oscillations with increased equivalence ratios. Finally high frequency transverse modes in the combustor duct are investigated.

### 7.1 Experimental Setup

The Volvo case is a configuration developed in the 1990's by Sjunneson et Al [SNM91], [SHL92], [APC92] with the goal to provide an experimental data base for the development and validation of numerical codes.

The Validation Rig consists of a rectangular duct section and a bluff body. The bluff body is designed as an equilateral triangle. Air enters the duct and gets mixed with propane behind the fuel injection. A honeycomb provides better mixing and a controlled level of turbulence. The top and bottom walls are water cooled and the side walls are air cooled to accommodate quartz windows for optical access [FL94]. The dimensions of the combustor are shown in Fig. 7.1. The flame sits behind the flameholder and the combustor discharges into a larger duct.

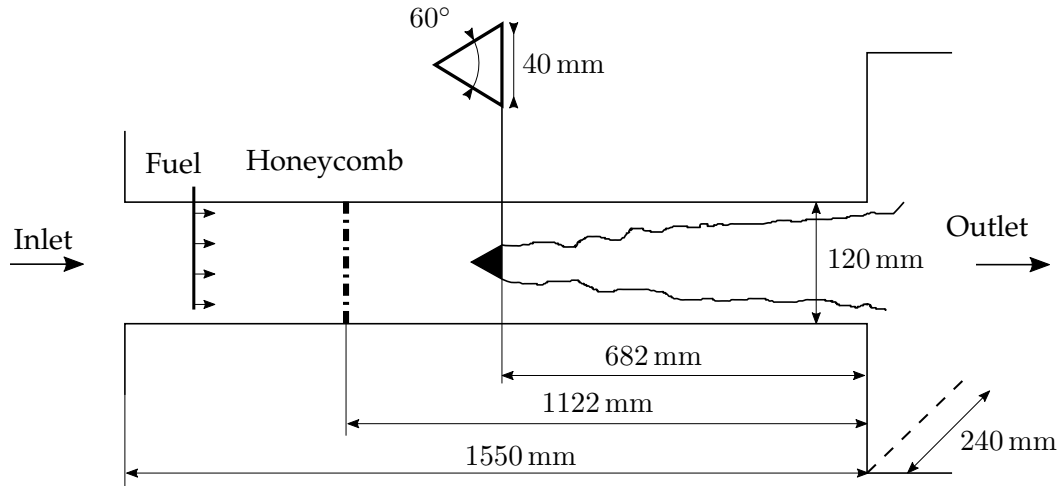


**Figure 7.1:** Experimental setup of the Volvo validation rig

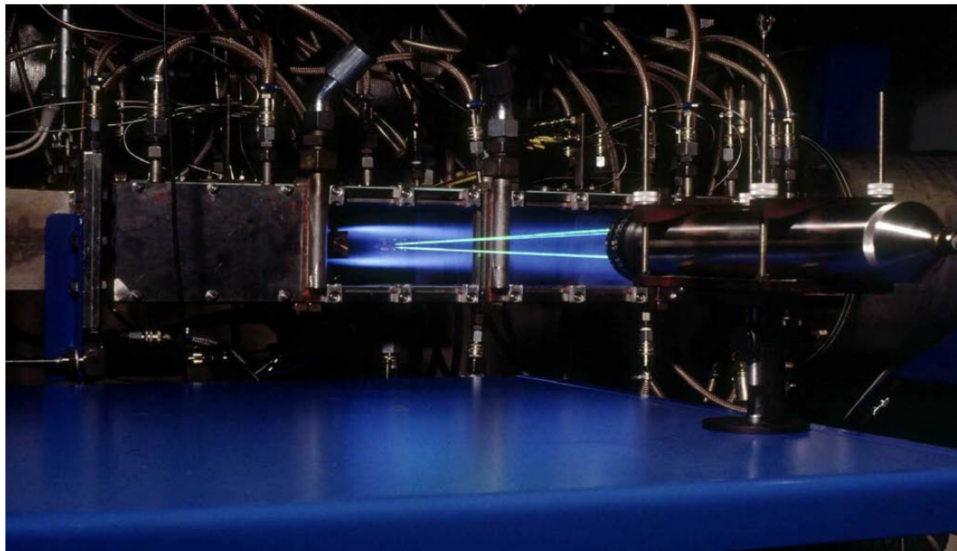


**Figure 7.2:** LDA measurements for the Volvo validation rig. [JE10]

Laser Doppler Anemometry (LDA) was performed to measure velocities and turbulent fluctuations (Fig. 7.2). Additionally, Coherent Anti-Stokes Raman Scattering was used to derive temperature profiles and measure species concentrations in the flow. The location of the measurements can be distinguished in planes M1-M7 which are, in a magnified view of the combustor, displayed in Fig. 7.3. Vortex shedding frequency, temperature and velocity profiles as well as RMS-values of pressure fluctuations are available for comparison.

For the reactive operating points two different inlet velocities have been investigated for several equivalence ratios (Fig. 7.4). At the low velocity, 100 Hz oscillations increase almost linear with increasing  $\phi$  up to  $\phi = 1$  where a sudden change in the RMS values is present. At the high velocity, featuring high frequency oscillations of 1380 Hz, a jump of the fluctuation values occurs at  $\phi = 0.7$ .

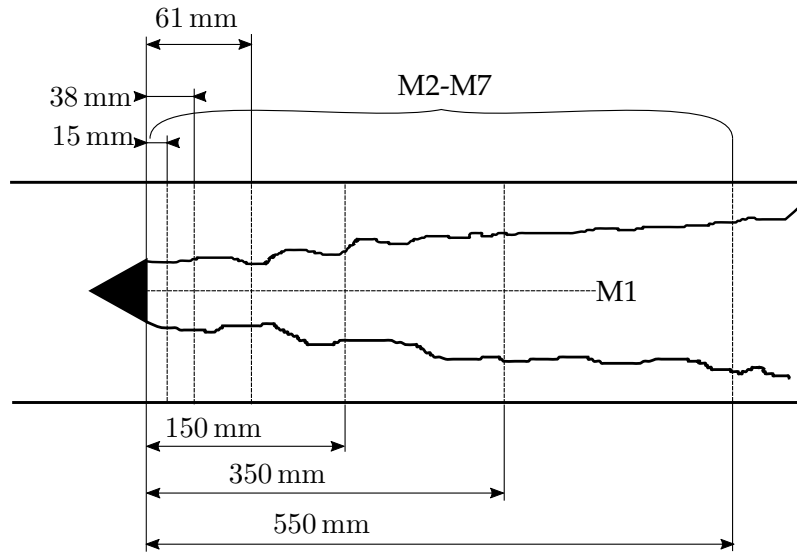


**Figure 7.3:** Measurement planes M1-M7 for the determination of flow field profiles

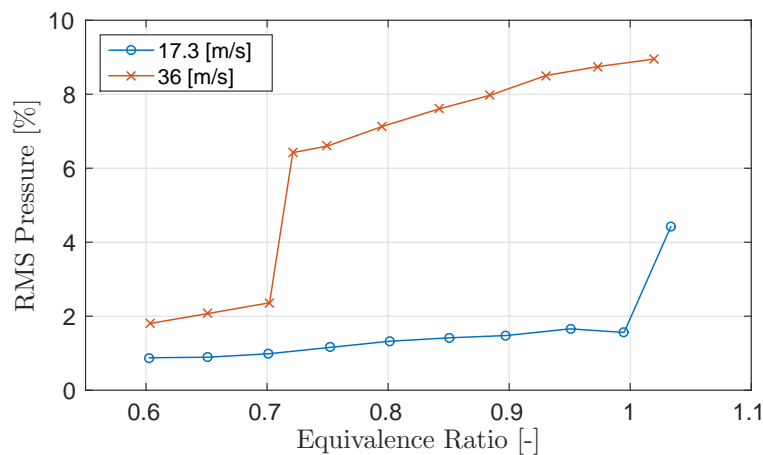


**Figure 7.4:** RMS value of the pressure for different equivalence ratios and inlet velocities [SOS91]

## 7.2 Literature Review

In most commercial combustion devices the flow speed is significantly higher than the flame speed. Therefore action has to be taken to enable combustion. Bluff bodies are one possibility. Mostly placed on the symmetry axis of a combustor they create a recirculation zone, which entrains the combustion products and transports them upstream for mixing and igniting the air/fuel-stream in the shear layer. This process stabilizes and anchors the flame to the bluff body, leading to its expression as a flame holder [SHL09]. Numerous forms of bluff bodies are implemented and were already studied extensively.

Offering a large validation base for numerical simulations the Volvo setup has already been investigated by different research groups and institutes (Tab. 7.2). In general, three main classes can be distinguished. A cold flow point (Case C) without

**Table 7.1:** Operating points for the Volvo case

	Case	$u_{bulk} [m s^{-1}]$	$\phi$	$T_u [K]$	Mode Topology
<b>C</b>	Cold flow	16.6	0.0	288	-
<b>R</b>	Reacting stable	17.3	0.65	288	-
<b>B</b>	Buzz	17.3	0.95	288	1Lx-0Ty-0Tz (100Hz)
<b>S</b>	Screech	36	0.72	288	1Lx-0Ty-2Tz (1380Hz)[Gha15]

combustion and two reacting points differing in terms of the inlet velocity ( $u_{bulk}^1 = 17.3 m s^{-1}$  and  $u_{bulk}^2 = 36 m s^{-1}$ ). For an inlet velocity of  $u_{bulk}^1$  and an equivalence ratio of  $\phi = 0.65$ , reported as the reacting stable case (Case **R**), temperature and velocity profiles are available.

In the experiments, the equivalence ratio was varied for  $u_{bulk}^1$  and the response of the combustor was tracked. As seen in Fig. 7.4, showing the RMS value of the pressure at the bottom wall ( $x = 0.85 m$ ), the fluctuation values vary. Interestingly, an equivalence ratio of  $\phi = 0.95$ , referred to as case **B**, is reported as the **Buzz** case in the literature featuring longitudinal low frequency oscillations. Regarding the RMS values of the pressure this operating point only differs by 50% from the reacting stable case in terms of the pressure oscillations. However, the drastic change in terms of instabilities occurs at over stoichiometric equivalence ratios, which will therefore also be investigated in this work

For the second inlet velocity ( $u_{bulk}^2$ ), Fig. 7.4 displays the fluctuation level as well. Case **S** (Screech) is referred to this inlet velocity with an equivalence ratio  $\phi = 0.72$ . Again, the choice of the point is disputable as it is located at a point where the fluctuation amplitude increases by a factor of three between two measurement points. A superposition of the low frequency mode and a high frequency mode of 1380Hz (transverse) was observed in the experiments. Unfortunately there is in general no information about the specific frequencies at the corresponding equivalence ratio. The only information is that low frequency oscillation occurred at the low inlet velocity and a high frequency oscillation at the higher inlet velocity.

An overview of the four operating points addressed in the literature is given in Tab. 7.1. Additionally to this points, different equivalence ratios will be investigated to have a further insight into the occurrence of the instabilities. These points will be introduced later on.

The first simulation results were already presented by the research group of Sjunnesson et Al. [SOS91] which introduced the Validation Rig. Afterwards, few simulation results were presented during the 90's [Olo92]. However, due to the restricted amount of computational resources these modeling studies were limited to RANS calculations.

In the last years, the advance in computation made transient URANS and LES simulations feasible as displayed in the increasing number of LES simulation for combustion devices [Pit06] [Gha15] [JZA06] [PK11]. This offered the possibility to

Table 7.2: Investigations on the Volvo validation rig of different research groups

Authors	Computational Domain	Cases				Outlet B.C.	Settings
		C	R	B	S		
Porumbel et Al. [Por06]	Partial 3D $1 \times 0.12 \times 0.24$ m	×	×	○	○	Partially Reflecting	LES, $2^{nd}$ order spatial and temporal, Linear Eddy Mixing model as closure for the reactive cases
Giacommazi et Al. [GGB04]	Partial 3D $0.55 \times 0.12 \times 0.24$ m and $0.55 \times 0.12 \times 0.08$ m	×	×	○	○	Fixed Pressure	LES, $2^{nd}$ order spatial and temporal, one-step chemistry
Park et Al. [PK11]	Partial 3D $1 \times 0.12 \times 0.48$ m	×	○	○	○	Fixed Pressure	LES, $2^{nd}$ order spatial and temporal, G-equation approach
Li et Al. [Li+16]	Partial 3D $1 \times 0.12 \times 0.12$ m	○	×	×	×	Acoustic Reflecting and Non Reflecting	LES, $2^{nd}$ order spatial and temporal, G-equation
Cocks et Al. [CSS13]	Partial 3D $0.782 \times 0.12 \times 0.08$ m	×	×	○	○	Wave Transmissive	LES with 4 solvers, $2^{nd}$ order spatial and temporal, flame surface density (FSD) model
Jourdain et Al. [JE10]	2D $1 \times 0.12$ m	○	○	×	×	Fixed Pressure	Arnoldi extraction and URANS, $3^{rd}$ order spatial and $2^{nd}$ order temporal, EDC-type combustion
Lee et Al. [Lee+16]	Partial 3D $1 \times 0.12 \times 0.24$ m	×	×	○	○	Partially Reflecting	URANS & LES, $2^{nd}$ order spatial and $1^{st}$ order temporal, Laminar flamelet approach
Fureby et. Al. [FL94] [Fur00]	Partial 3D $0.8 \times 0.12 \times 0.12$ m	×	×	○	×	Fixed Pressure	LES, $2^{nd}$ order spatial and temporal, flamewrinkling
Ghani, Maestro et Al [Gha15] [GMB16] [Gha+15] [Mae+17]	Full 3D $1.5 \times 0.12 \times 0.24$ m	×	×	×	×	3D NSCBC	LES combustion model LES, $3^{rd}$ order temporal and spatial scheme two-step mechanism

study the dynamics of the combustor. During this literature review, emphasis will be put onto recent publications. A selection of the conducted research is shown in table 7.2.

The first publication of LES simulations of the stable cases was done by Fureby et Al [FL94]. Due to the lack of computational resources in this time they were forced to use 2D-meshes, which were not able to totally mimic the physical processes in the flow. In the year 2000, LES-calculations of a partial 3D-domain representing the half depth of the shortened combustor were conducted. The work focused on the influence of vortex shedding on the combustion instabilities [Fur00]. Case C, R and S were investigated. However, for the two reacting operating points, oscillations that were not reported in the experiments were observed.

Cocks et Al. [CSS13] compared the performance of four different solvers (OpenFOAM, Fluent and two academic solvers) on case C and R. Noteworthy was that especially the occurrence of symmetrical or asymmetrical shedding in the reacting cases led to derivations in terms of the combustion and subsequently the acceleration downstream of the bluff body.

Giacomazzi et Al. [GBB04] studied the differences between different simulation domains (2D, 3D with periodic boundary conditions, full 3D), concluding that in their case, only the full 3D domain is able to resolve flow phenomena as the shortening of the recirculation zone and the acceleration downstream of the bluff body.

G-equation LES was performed by several groups [PK11] [Li+16]. Focusing on the dynamical behavior of the flame, Li et Al studied case R, B and S using a G-equation-based flamelet library model. Another approach was investigated as a fixed pressure outlet was combined with a reflective and a non-reflective inlet condition. Flow fields matched the experimental results.

In general, less studies have been conducted focusing on the combustion instabilities generated due to the coupling between heat release, flow and acoustics. Jourdain et Al. [JE10] used a different approach than LES. They developed linear flow solvers combined with an Arnoldi extraction method, which computes the least damped eigenmodes. Their results matched results gained by URANS calculations for case B and case S, but not the experimental results. They indicated that the high frequency could also be the 6th longitudinal mode instead of a transverse mode.

Lee et Al. [Lee+16] focused on the stability of the combustor. Using the inlet velocity of the reacting stable case the mixture fraction was varied and the response of the combustor analyzed. In contrary to the experimental findings, they observed a stable regime for  $0.7 < \phi < 0.75$  whereas it was reported to occur at  $\phi = 0.65$ . However, confirming the experiments, an unstable regime was reported for higher equivalence ratios ( $\phi > 0.8$ ).

The leading institute in the last years in terms of investigations of the combustion instabilities in the Volvo case is CERFACS. As the only institute that was able to predict all four operating points accurately, several publications are addressing different aspects. Ghani et Al. [Gha15] performed LES calculations for non reacting



and reacting flows and compared them to experimental results and Helmholtz solver predictions. The CFD code AVBP was used, which solves the NSE using two step Taylor-Galerkin convection scheme (third order accuracy in time and space). The WALE subgrid model and the thickened flame model to describe flame/turbulence interaction were used [GMBS16]. For the control of combustion instabilities boundary conditions are crucial. This difficulty was solved by using Navier-Stokes Characteristic Boundary Conditions (NSCBC) [PL92].

The effort was rewarded as this setup was able to capture the flow and combustion behavior, matching with temperature and velocity profiles, as well as capturing transversal and longitudinal modes in the different cases. Noteworthy was the comment for the reacting stable case. Even though no dominant frequency was reported from the experiments, recent research [Roc+17] ponders this statement. The presence of acoustics is not disqualified. High sensitivity of different parameters was reported resulting in different distinct limit cycles [GMBS16].

Rochette et Al [Roc+17] summarized and expanded the investigations. The lack of information about inflow/outflow boundary conditions was condemned as the main problem in the experimental setup as they have a major impact on stability or instability of the combustor. Also the combustor was found to be very sensitive in respect to heat transfer at the bluff body and the chemical schemes. Turbulent combustion models played a minor role.

It can be concluded that the recent publications showed the complexity to model the Validation rig. The lack of information about the reacting stable case and the statement of different researchers that do not disqualify thermo acoustic instability for this case shows the sensitivity of the burner to many parameters. Up to now, the unstable cases were only predicted accurately by Ghani et Al. and partially by Fureby.



## Chapter 8

# Reynolds-Averaged Simulations

Historically the RANS approach has been the only possible method to solve the NSE as the computation of the instantaneous flow remained too expensive for a long time [PV05]. However, RANS is nowadays still the standard approach in commercial codes and has numerous times proven its value in the field of fluid mechanics. This chapter aims to introduce the numerical setup for the RANS calculations, introduces convergence criteria and displays the results for Case C and R in comparison to the experimental flow fields. In the RANS approach the conservation equations are not explicitly solved for the turbulent fluctuations in the flow. Acoustics are not present in their solution as a mean field is derived. Therefore acoustics can not be studied in this section. At first the numerical domain is introduced. Afterwards, initial and boundary conditions, which are relevant for the physical models, are given. Furthermore, a grid study is introduced ensuring that the grid fulfills both the meshing criteria as well as acceptable computational resources. Finally a conclusion for the RANS calculations of the two operating points is done to determine the settings and the mesh that will be further on used as the LES calculations are initialized with these results.

## 8.1 Numerical Settings

### Computational Domain

The computational domain used in the major part of this work is a partial three dimensional slice of the combustor. Fig. 8.1 shows the outer surface of the combustor with increased transparency and the reduced domain in blue. The thickness  $t$  in  $z$ -direction equals the half of the bluff body size. This simplification is done for the calculations of all cases as the topology of the mode that is reported for case B has a longitudinal shape and therefore can be captured with a reduced domain (see Section 10). The only exception is case S. This simplification saves computational effort massively as only  $\frac{1}{12}$  of the combustor dimension is represented in the partial domain. The only case that requires the full domain of the combustor is case S as it features a high frequency transverse mode. The length of the duct represents the total length of the combustor ( $L = 1.5 \text{ m}$ ). The honeycomb is omitted as it is presumed to have minor influence on the acoustics [Gha15] and no geometrical information is available for it. In the experimental setup it was only used to assure a constant turbulence level

and enhance mixing. One may notice, that in contrary to the computational domains used by the presented publications, the discharges duct is part of the computational domain. This will be elaborated more precisely during the presentation of the LES settings as it is directly connected to the boundary conditions which will be of major interest for the transient simulations.

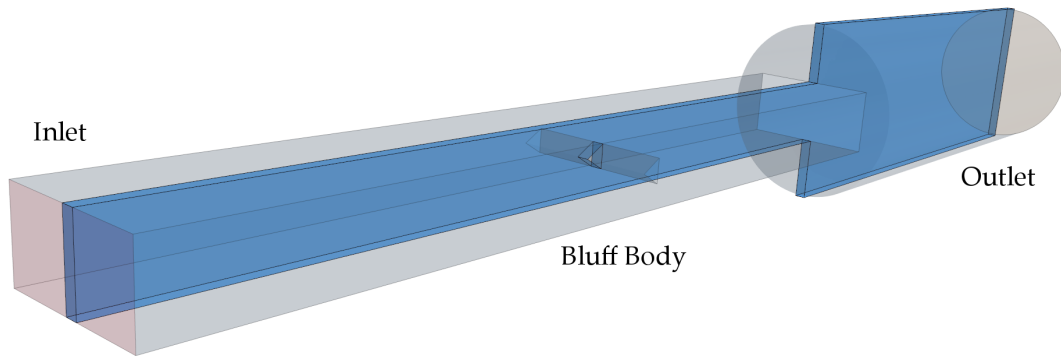


**Figure 8.1:** Computational domain of the Volvo case

### Meshing and wall treatment

Different meshes are created to achieve a mesh independent solution for the RANS calculations. Prior to running the simulation and investigating the solution of the different meshes, several mesh quality criteria are checked as poor mesh quality can impact the solution. The different measures won't be introduced explicitly here but the Siemens Mesh quality guidelines are followed including

- Cell skewness angle  $< 80^\circ$
- Boundary skewness angle  $< 80^\circ$
- Face validity metric  $> 0.95$
- Cell quality metric  $> 0.5$
- Volume change  $< 0.1$

Accurate prediction of flow and turbulence across wall boundary layers is crucial. The quality of the modeled boundary layer is controlled using the dimensionless wall distance  $y^+$ . Using the all- $y^+$  treatment of StarCCM+ the recommendation would be  $y^+ < 1$  or  $30 < y^+ < 60$  but even in between those values reasonable solutions are created [Sta]. Subsequently it is taken care that the majority of the cells lies in the appropriate range of values. While the  $y^+$  values of the cells at the bluff body are kept at a value at least  $< 3$ , the  $y^+$  values of the duct walls are kept in the range of 25 – 60.

Even though the simple geometry of the combustor would enable the use of structured meshes, polyhedral meshes are used as the insights gained during this work shall be transferred to complex geometries of Siemens combustors which cannot be meshed in a structured manner.

Finally, four different grids having a cell count of 0.33, 0.66, 2.2 and 4.1 million cells were investigated. Their results will be presented and investigated in sections 8.2 and 8.3. The differences of the meshes were achieved by sweeping the base size, which is connected to each volume control defined over the geometry. An exemplary view of the refinement zones around the bluff body is shown in Fig. 8.2. Around the bluff body the finest cells are present with a gradual coarsening further down- and upstream. The minimum cell sizes (around the bluff body) are presented in Tab. 8.1.

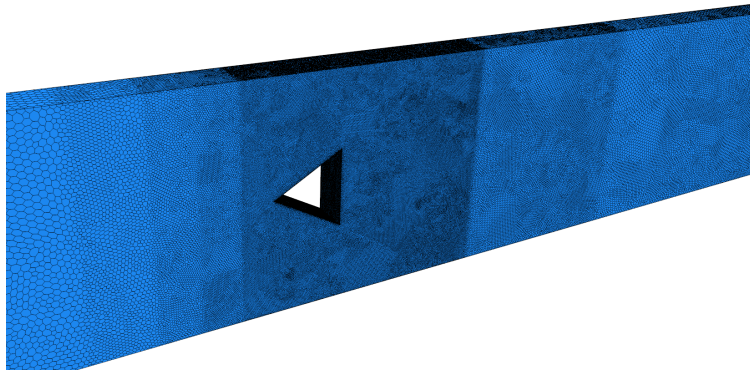


**Figure 8.2:** Refinement zone near the bluff body

**Table 8.1:** Smallest cell sizes in region around bluff body

Mesh [ <i>Mio cells</i> ]	$\Delta x[m]$
0.33	0.001
0.66	0.0008
2.2	0.0006
4.1	0.00045

## Boundary Conditions and Flow Field

Defining physically valid initial and boundary conditions is of major importance to obtain good results with CFD. The initial results defining the necessary values at the very beginning of the simulation are introduced through a guessed flow field with constant values. The boundary conditions try to map the reality as good as possible. Top and bottom walls are modeled with a fixed temperature of  $T = 350$  K as the experimental setup is water-cooled at this locations. The sidewalls are treated as symmetry planes. The bluff body walls are defined as adiabatic walls as they are not cooled. For a specific determination of their temperature a conjugate heat transfer simulation would be needed. The reflection behavior of the boundary conditions is of minor interest in this chapter as acoustics are not present in the averaged flow field. Therefore the inlet and the outlet boundaries are modeled with a fixed inlet velocity

(Tab. 7.1) providing the reported mass flow at the inlet and a fixed pressure outlet representing the atmospheric conditions.

### Turbulence Closure and Combustion Modeling

Both the turbulence closures presented in section 2.1.2 are used throughout this work. The Realizable  $k - \epsilon$  and the SST  $k - \omega$  will further on be abbreviated as  $k - \epsilon$  and  $k - \omega$ . To save computational effort the combustion modeling was done with tabulated chemistry. The kinetic rate closure was favorable as it provides no factor that has to be tuned to accurately mimic the combustion. However, the turbulent flame closure was tested as well. As an addition, the complex chemistry approach was considered despite the computational effort.

### Convergence Criteria

Different measures can be used to derive if a solution is converged and if the iterative procedure can be stopped. Two main quantities can be monitored therefore:

- **Residuals:**

In an iterative method a solution is guessed and systematically improved by the equations. After a number of iterations an approximative solution is derived. As this solution does not satisfy the equations exactly a residual  $r$  is introduced [FP02]. This residual measures the imbalance of a conserved quantity in a CV. Realistically, these residuals will never reach zero, but the lower the value is, the more accurate is the solution. Star CCM+ determines a RMS residual of all cells  $n$  by

$$r_{rms} = \sqrt{\frac{1}{n} \sum n r^2}. \quad (8.1)$$

The residuals are normalized by

$$r_{norm} = \max\{r_1, r_2 \dots r_m\} \quad (8.2)$$

to compare multiple residuals [Sta]. Residuals will be monitored for several quantities.

- **Quantities of interest:** The goal of RANS calculations is to achieve a steady state. Subsequently the flow field should not change from iteration to iteration. Another measure for the convergence of a solution is to monitor different quantities as in- and outgoing massflows, integrated quantities like average temperatures or quantities at discrete points.

The named measures are very important to achieve an accurate solution for the problem. However, especially under consideration of the characteristics of an intrinsically unsteady flow in the wake of the bluff body, monitoring discrete points should only be used as an additional measure as the solution tends to slightly but noticeably oscillate

around a mean flow over the iterations. Therefore, the mean results presented in the following represent iteration averaged results. Averaging started when the residuals were settled and monitors indicated convergence. For the cold flow simulations the averaging started after 1000 iterations, for the reacting simulations 2000 iterations after ignition.

## 8.2 Coldflow Results

The first operating point that is being investigated is case C. Fig. 8.3 displays the resulting mean axial velocities on the planes M2-M5. The experimental results are indicated by the dots. First, the mesh independency is analyzed using  $k - \epsilon$ . In vicinity to the bluff body all simulations show a similar behavior, but they begin to differ slightly further downstream. However, the different mesh sizes only seem to differ slightly.

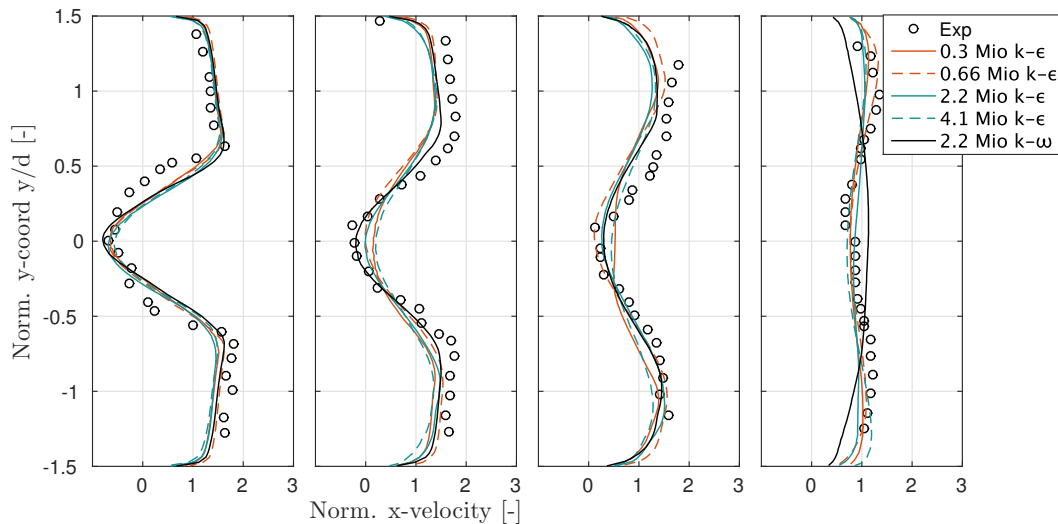


**Figure 8.3:** Mean x-velocities on M2-M5 for case C

Another perspective on the solutions is given by Fig. 8.4 which shows the mean axial velocities on the centerline M1. All the simulations show almost an equivalent recirculation zone which is slightly too short and too strong. The  $k - \epsilon$  simulations show a similar progression further downstream but differ slightly in between the normalized coordinates of  $x = 1 - 3$ . Only the 2.2 million mesh predicts the flow accurately in this region.

The impact of the turbulence model is captured for the 2.2 million mesh. All the  $k - \epsilon$  simulations tend to mimic the flow fields more accurately than  $k - \omega$ , which underestimates the velocity in the region near to the walls and overestimates the velocity in the center for M5. The overprediction of the axial velocity in the center of the duct for the  $k - \omega$  closure is clearly visible in Fig. 8.4.

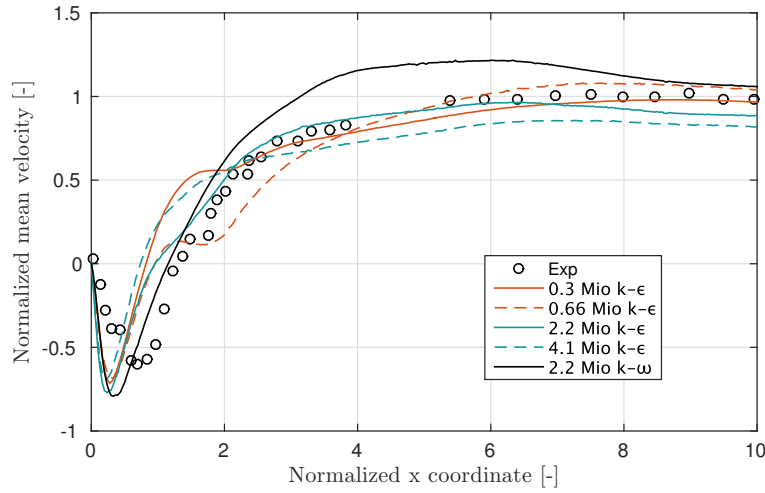


**Figure 8.4:** Mean velocity on the centeraxis for four different mesh densities using operating conditions of case C

The residuals, displayed exemplary for the  $k - \epsilon$  simulation with 2.2 million cells in Fig. 8.5, indicate a converged solution as the residuals of each quantity decreased to at least a value below  $10^{-4}$ .

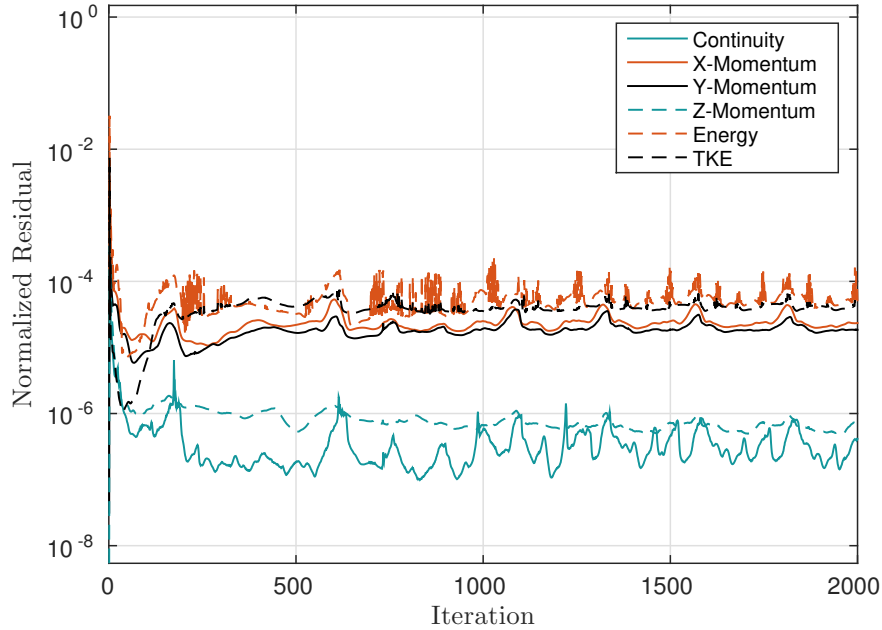


**Figure 8.5:** Residuals for case C using the  $k - \epsilon$  closure with 2.2 million cells

### 8.3 Reacting Stable Results

This section shows the RANS results for case R. Similar to the previous chapter, simulations were done for four meshes as well as  $k - \epsilon$  and  $k - \omega$ . As a second part



the combustion modeling is varied. The flame shape for the RANS simulations is shown exemplary for the 2.2 million mesh using the  $k - \epsilon$  approach in a contour plot of the temperature (Fig. 8.6).

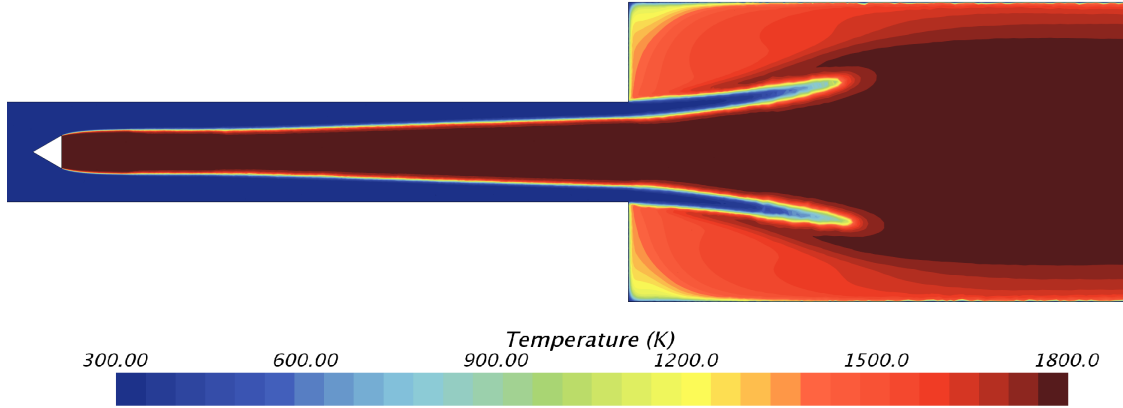


**Figure 8.6:** Flame shape for case R using the  $k - \epsilon$  closure with 2.2 million cells

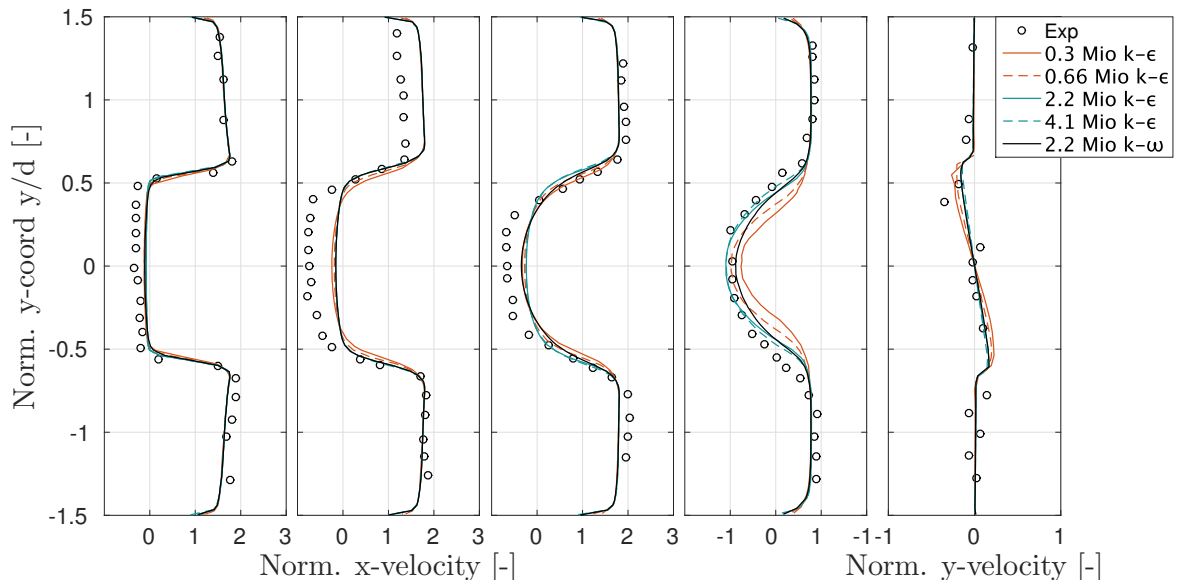


**Figure 8.7:** Mean x-velocities on M2-M5 and mean x-velocity on M2 for case R

Similar to the previous chapter, the mesh independency is evaluated for  $k - \epsilon$ . Fig. 8.7 shows the mean axial velocity on the planes M2-M5 and the mean transverse y-velocity on M2. Only one plane is shown for the transverse velocity as almost no transverse velocity is present on the planes further downstream. Regarding the axial velocity, differences between the meshes are hardly visible on planes 2-4. All simulations underestimate the recirculation zone in the vicinity of the bluff body. However, differences occur on plane 5 as the recirculation zone tends to narrow faster for the coarser meshes. The 2.2 and the 4.1 Mio mesh capture the velocity profile quite accurately. The same trend is visible in Fig. 8.8. All simulations resemble

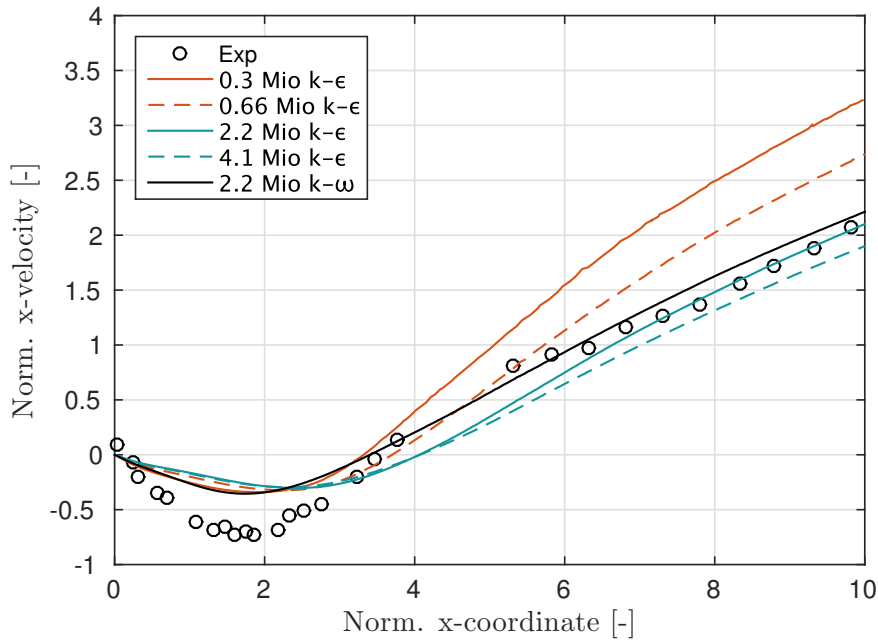


**Figure 8.8:** Mean velocity on the centeraxis for four different mesh densities using operating conditions of case R

themselves close to the bluff body and the coarse meshes overestimate the acceleration downstream. In terms of the recirculation zone the trend of is reversed in comparison to the cold flow results. For the reacting case, the recirculation zone is predicted too long and too weak. The temperature planes that were measured are displayed in

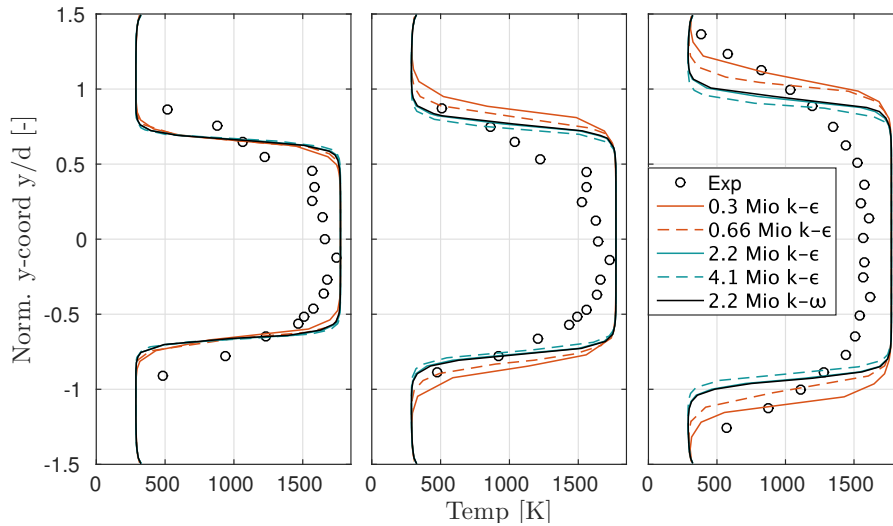


**Figure 8.9:** Temperature profiles on M5-M7 for case R

Fig. 8.9. While the temperature profiles of the different simulations almost equal for M5, the reason for the overestimated acceleration downstream for the coarse meshes can be observed on M6 and M7. The flame is wider and therefore more gas expands through the higher temperature. Subsequently the volume flow and thereby the axial velocity rises. In general for all simulations the gradient from the burnt to the

unburnt region is too high as the experimentally derived mean temperature profiles are flatter, probably due to the movement of the flame in the turbulent flow, which does not happen in RANS.

The differences between the turbulence levels are minor than for the previous operating point. For the 2.2 million mesh the  $k - \omega$  closure overpredicts the velocity downstream slightly.

A comparison of the two closures for the flamelet approach is done in Fig. 8.10 displaying the a mean axial velocity on the central axis. The differences by varying the tuning factor  $A$  of the TFC approach are marginal. The recirculation zone is underpredicted by both closures but predictions are quite accurate further downstream. The complex chemistry approach was tested as well. However the calculations resulted in unphysical solutions and no convergence could be achieved. Therefore the presentation of the results is omitted here.

The residuals, shown in Fig. 8.11, display the convergence for the  $k - \epsilon$  simulation with 2.2 million cells. All residuals drop below  $10^{-5}$  and indicate convergence of the solution. For this representation Iteration 0 corresponds to the moment of ignition. In general, the reactive simulations were started with a coldflow and than the mixture was ignited behind the bluff body by patching the progress variable to  $c = 1$ , describing a fully burnt mixture, on a small box.

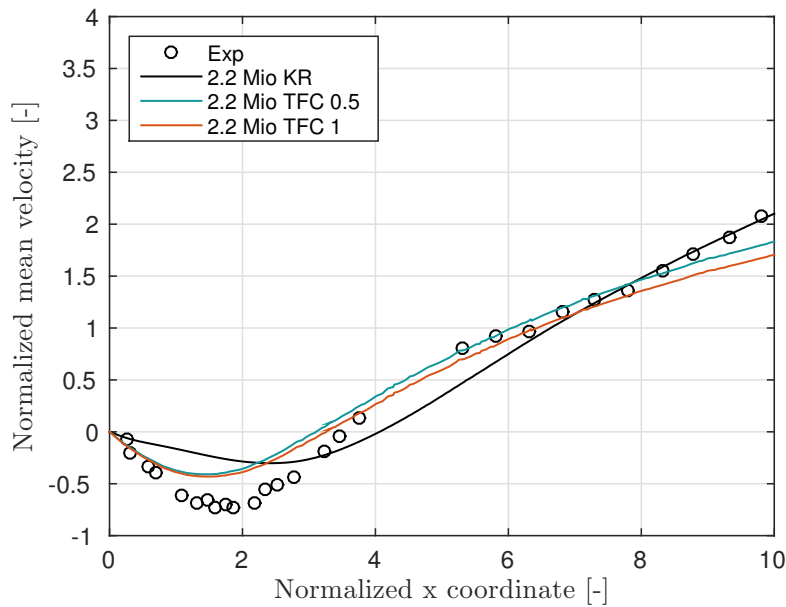


**Figure 8.10:** Comparison between the kinetic rate and the turbulent flame speed closure for  $k - \epsilon$  and the 2.2 Mio mesh

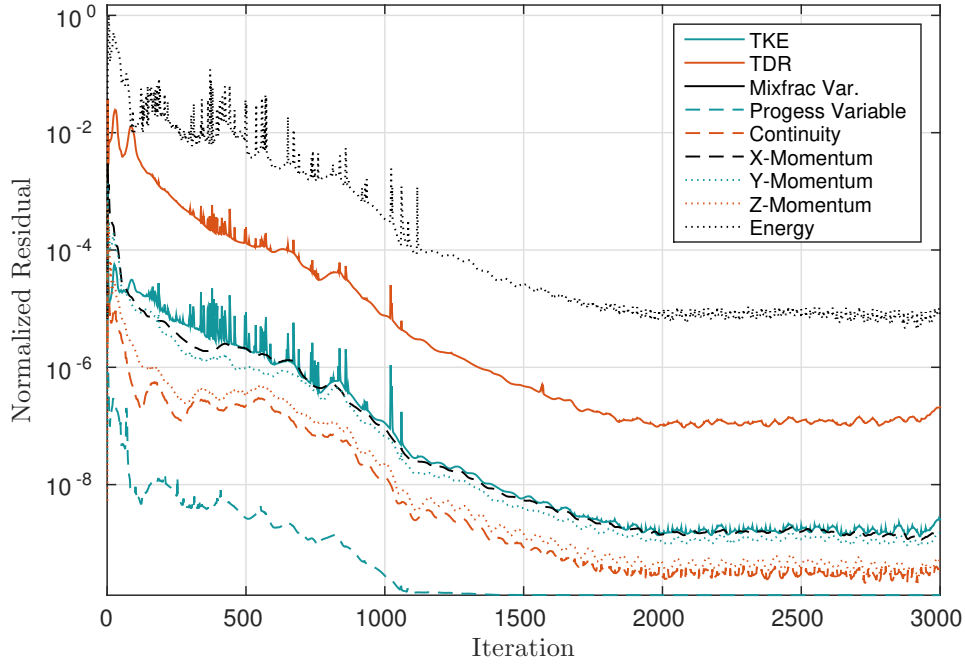


Figure 8.11: Residuals for case R with 2.2 million cells

## 8.4 Conclusion of the RANS approach

Different meshes, turbulence and FGM closures have been studied using the experimental database of case C and R. Keeping in mind that these cases are intrinsically unsteady the RANS approach gives a good indication of the flow field. However, the RANS approach clearly reaches its limits in predicting the recirculation zone directly behind the bluff body. As a conclusion and a foresight for calculations which will be done to initialize LES, the 2.2 million cell mesh performed satisfactory. It showed a sufficient grid independence in relation to the finer 4.1 million mesh.

As a turbulence closure the  $k - \epsilon$  approach was used as  $k - \omega$  overestimated the axial velocity downstream of the bluff body for the cold flow. In case R, no major differences were detected.

Differences between the closures for the flamelet approaches were marginal. While TFC showed slight advantages in the recirculation zone, Kinetic Rate performed better further downstream. As no tuning factor is necessary for KR, it will be used subsequently.

## Chapter 9

# Acoustic Analysis with Comsol Multiphysics

Since the objective is to capture the dynamical behavior of the Volvo setup, it is useful to compute the chamber modes before performing costly LES. Comsol Multiphysics is used to solve the discretised Helmholtz equation (Section 2.2) in the domain.

### 9.1 Settings

The full three dimensional domain (Fig. 9.1) of the experimental setup is used including the dischargement of the gases into the larger duct. The inlet and the combustor walls are modeled as zero velocity fluctuation boundaries ( $u' = 0 \text{ m s}^{-1}$ ) and the outlet as a fixed pressure boundary ( $p' = 0 \text{ Pa}$ ). The sound speed field is calculated based on an approximative temperature field corresponding to cold gases ( $T = 288 \text{ K}$ ) for  $x < 0.82 \text{ m}$  and to hot gases ( $T = 1800 \text{ K}$ ) for  $x > 0.82 \text{ m}$ . The mean velocity of the flow is neglected due to  $u \ll c$ .

### 9.2 Chamber modes derived by Comsol Multiphysics

A set of the modes found by Comsol is summarized in table 9.1.

Fig. 9.2a and 9.2b display the first (86 Hz) and the second (217 Hz) longitudinal mode obtained by the Helmholtz solver. The normalized pressure amplitudes on the central axis H1 are displayed in Fig. 9.3a. The first mode corresponds to the low frequency oscillation that was detected by Sjunnesson et Al. [SOS91] in the experiment. The mode shape is a classical quarter wave mode with a pressure antinode at the velocity inlet and a quasi pressure node at the dischargement into the outlet duct. The term quasi pressure node corresponds to the fact that  $p'$  is not yet zero at the dischargement ( $x = 1.5 \text{ m}$ ). Pressure is still slightly fluctuating at this position. The second longitudinal mode ( $f = 217 \text{ Hz}$ ) is presented as it arised in the LES simulations which will be presented later. However, it was not reported experimentally.

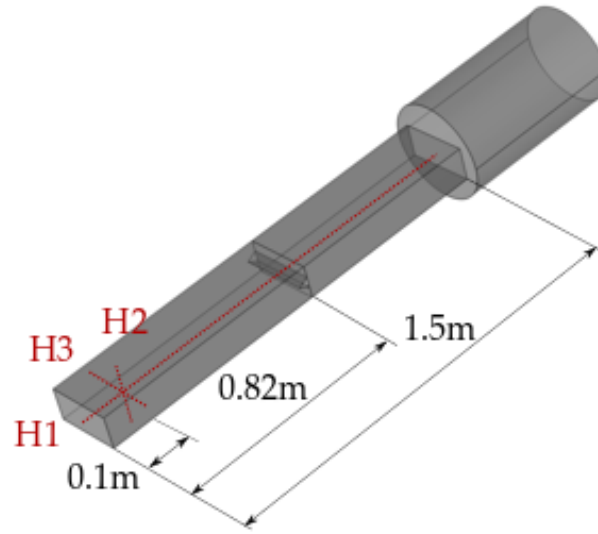


**Figure 9.1:** Computational domain for the calculation of the mode shapes. H1, H2 and H3 indicate the the line probes for evaluation.

**Table 9.1:** Frequencies and mode shapes obtained by the Helmholtz solver and LES in comparison with the experimental results [SOS91]. The mode name consists of the number of pressure nodes in x-direction (nLx), y-direction (pTy) and z-direction (qTz).

Mode	Frequency [Hz]	LES [Hz]	Experiment [Hz]
1L-0Ty-0Tz	86	95	100
2L-0Ty-0Tz	217	200	not reported
3L-0Ty-0Tz	320	not observed	nr
4L-0Ty-0Tz	430	no	nr
5L-0Ty-0Tz	532	no	nr
6L-0Ty-0Tz	705	no	nr
0L-0Ty-1Tz	716	no	nr
1L-0Ty-1Tz	770	no	nr
7L-0Ty-0Tz	850	no	nr
3L-0Ty-1Tz	870	no	nr
8L-0Ty-0Tz	952	no	nr
4L-0Ty-1Tz	1001	no	nr
9L-0Ty-0Tz	1090	no	nr
6L-0Ty-1Tz	1318	no	nr
1L-1Ty-0Tz	1422	no	nr
1L-0Ty-2Tz	1422	not observed	1380

Searching for a corresponding mode to the high frequency oscillations, two modes with a equivalent frequency of  $f = 1422$  Hz are found in Comsol. Both are superpositions of a transverse and the first longitudinal mode. The modeshape was not reported explicitly in the publications of the experiment. While the choice was

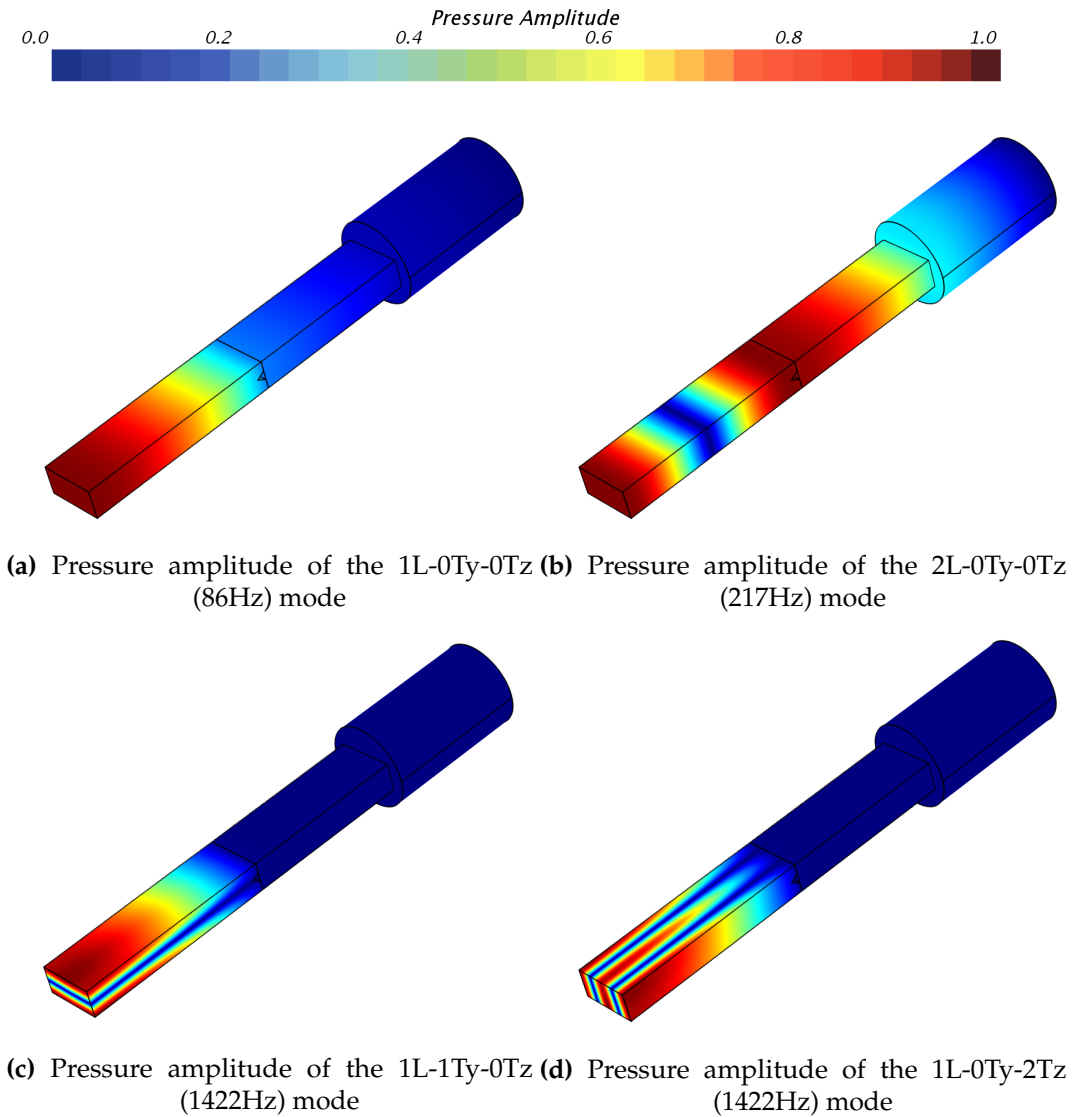


**Figure 9.2:** Absolute pressure amplitude of the 1L-0Ty-0Tz, 2L-0Ty-0Tz, 1L-1Ty-0Tz and 1L-0Ty-2Tz mode

obvious for the longitudinal mode, it isn't for the transverse mode.

The first transverse mode (Fig. 9.2c) features fluctuations in y-direction while the second (Fig. 9.2d) features fluctuations in z-direction. The mode shapes for both are displayed on the probe line H2 and H3 extended in y- and z-direction at  $x = 0.1$  m (Fig. 9.3b and 9.3c). Which mode corresponds to the high frequency oscillation can not be derived by this approach. But following the work of Ghani [Gha15], he suggests that the 1L-0Ty-2Tz mode is present as his LES-results indicated a symmetric pattern of perturbations for transverse velocity and heat release in z-direction.

The solution of the the Helmholtz solver clearly shows where large pressure amplitudes can be respected. Even though the heat release will fluctuate heavily downstream of the bluff body, the main pressure fluctuations for the first longitudinal mode may be detected upstream, near to the inlet. That's due to the fixed velocity ( $u' = 0$ ) condition at the inlet leading to an antinode in pressure. Contrary to the 1L

mode, a second antinode is present for the 2L mode downstream of the bluff body.

Possible sources for the derivation of the frequencies obtained by the Helmholtz equation and the ones from the experiments are the neglect of the flow and the approximated temperature field. Also no heat combustion-acoustic coupling is considered as this a pure acoustic approach. With an accurate temperature profile the modes would penetrate deeper into the region behind the bluff body as the change in temperature (and therefore speed of sound) acts like a reflector at the bluff body in this approach. The larger regions with lower sound speeds would lead to a lower frequency and thereby the difference between the obtained 1L mode and the experiments should shrink. However, the frequencies are detected accurately if the simplifications are kept in mind.

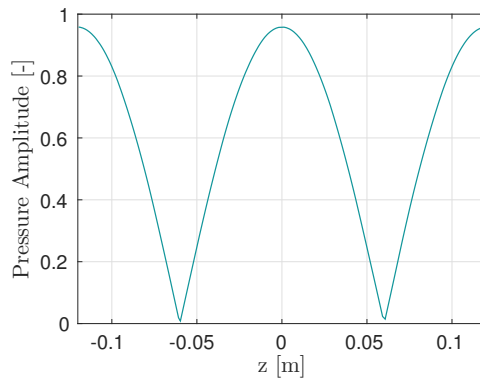
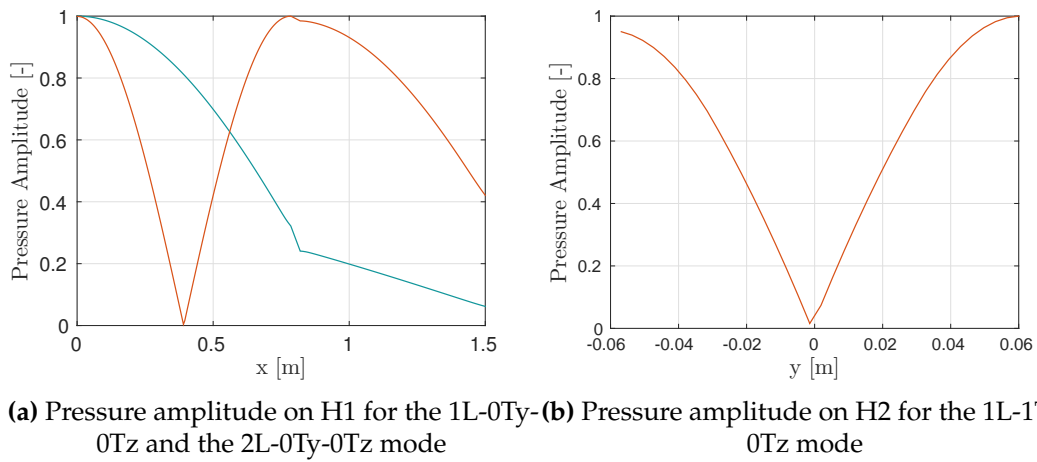


**Figure 9.3:** Modeshape of the 1L-0Ty-0Tz, 2L-0Ty-0Tz, 1L-1Ty-0Tz and 1L-0Ty-2Tz mode



## Chapter 10

# Large Eddy Simulations

In contrast to RANS, LES resolves the turbulent structures up to a certain filter width  $\Delta$  and offers the possibility to study the acoustics in the combustor. It is a superior approach for intrinsically unsteady flows but also requires a vast amount of computational resources. In this chapter the simulations of all four operating points are presented.

At first basics of the numerical setup are introduced. After a case-specific explanation of the settings, the non reactive case C is discussed and compared to the experimental results and the best RANS result. Then the reactive operating points with the low inlet velocity are investigated. The influence of the boundary conditions, the mean flow fields and the SGS modeling is discussed for case R. Afterwards the coherence of the equivalence ratio and the magnitude of the fluctuations is targeted and excited modes are studied. Finally, case S with a high inlet velocity is presented. Using the full 3-D domain, simulations for two equivalence ratios are performed.

### 10.1 Numerical Settings

At first, the general settings will be discussed. Later on, in the corresponding chapters, case specific settings will be specified. The LES settings used for the cases depend mainly on the experiences that were made during the test cases in chapter II. Subsequently the segregated solver is used with the unsteady implicit algorithm. Temporal discretization is done with the second order accurate 3 level BWD scheme. The spatial discretization is based on the bounded CD scheme offering an accuracy up to second order.

#### Computational Domain and Boundary Conditions

Unfortunately, geometrical information about the experimental setup is limited to the combustor section and the bluff body. Neither the inflow conditions, nor the discharge duct is specified explicitly. To accurately mimic the realistic operating scenarios the computational domain for the calculations compromises the whole combustor section from the air inlet to the dischargement into the atmosphere (Fig. 8.1).

The discharge duct was added because information about the boundary conditions at the dischargement into the larger duct are not available. Therefore the

decision was made to add the discharge duct, which should impose an accurate jump condition, and thereby acoustic behaviour at the dischargement. However, it obviously adds cells, making the simulation computationally slightly more expensive. Two different 3-D computational domains in terms of the depth of the combustor were used. One represents the full domain and the other the slice which was used for the RANS calculations. Additionally a quasi 2-D approach with a depth of one cell was tested for case C. As this approach was not succesful, cases C, R and B were modeled using the partial 3-D domain. Featuring a transvers mode, the full three 3-D domain has to be used for the screech case.

For the LES of the Volvo validation rig the boundary conditiations are crucial. The acoustics control the stability of the burner and therefore care has to be taken to model the BC accuratly. The reviewed literature agrees in terms of the inlet BC. Almost all of the publications used a fixed velocity ( $u' = 0 \text{ m s}^{-1}$ ) inlet, which is acoustically reflecting.

The outlet boundary conditions differ. None of the works includes the dischargement of the combustor into the larger duct and the majority used a fixed pressure outlet. But following a simple analytic approach in Poinso's work [PV05] shows that the reflection coefficient for a jump condition (dischargement into the larger duct) is smaller than  $R = 1$ . Subsequently approaches with advanced BCs were investigated as for example the 3D NSCBC conditions used by Ghani [Gha15]. The approach used in this work is different. Adding the discharge duct should impose the correct condition for the jump but now the problem is shifted to the outlet of the domain. Ideally, the outlet would be non-reflecting and thereby acoustics, which are present in the discharge duct as well, would be able to leave the domain and the interaction with the combustor section would be reduced. Otherwise the reflected acoustics of the boundary could modulate the flow in the duct as they are able to travel upstream.

The first step is to increase the cell size downstream towards the outlet. This increases the dissipation and damps the fluctuations in the discharge duct. As presented in section 2.1.5 two outlets are available in StarCCM+. The standard fixed pressure and the freestream outlet. The fixed pressure boundary is used for the non reacting cases. As no combustion is present the fluctuation levels were low even though reflection at the outlet was present.

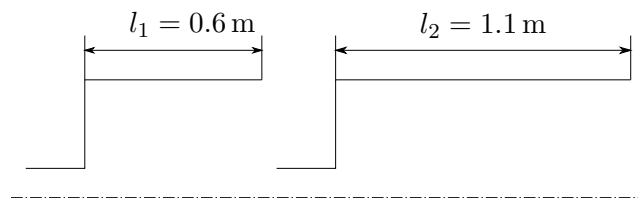


**Figure 10.1:** Short (Left) and long (Right) discharge duct

For the reacting cases, with thermoacoustics present, the fluctuations were higher and therefore a solution had to be found. The first step was the use of the freestream

boundary condition. However, as already shown in the test cases, the sensitivity to the mach number can cause pressure drifting. Two actions were taken to solve this issue. At first the discharge duct was extended (Fig. 10.1), thereby the fluctuations were reduced leading to a more homogeneous flow field that perturbrates the outlet. Impinging of transverse fluctuations is hereby minimized.

A further step was the use of an acoustic suppression zone. It is introduced as a source term, defined by

$$S_j = k \cdot g(x)(u - u_{mapped}), \quad (10.1)$$

into the momentum equation. To avoid reflections, which can occur by introducing the source term, the shape of the product of the strength  $k$  and the geometrical definition  $g(x)$  is implemented exponentially (Fig. 10.2). While  $k$  is a constant value  $g(x)$  defines the form of the shape based on the x-coordinate. As a result the velocity fluctuations of the flow are damped and the flow is assimilated towards the velocity field  $u_{mapped}$  which is consequently mapped onto the boundary. This ensures that the Mach number of the flow equals  $Ma$  imposed onto the outlet closely and should thereby avoid the pressure drift.

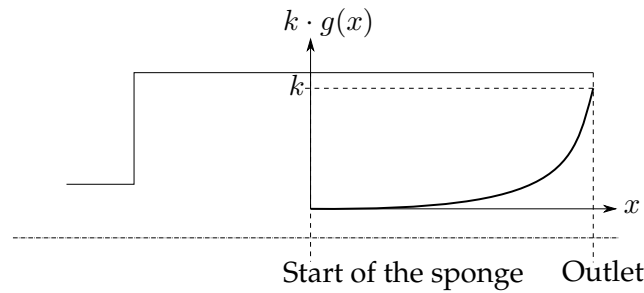


**Figure 10.2:** Trend of  $kg(x)$  in the domain of the Volvo case

Table 10.1 summarizes the four different outlet conditions that were tested on the reacting cases.

**Table 10.1:** Outlet boundary conditions

Configuration	Domain	Outlet	ASZ	Mapped Fields
1	Short	Pressure Outlet	No	Constant
2	Short	Freestream	No	Constant
3	Long	Freestream	No	RANS
4	Long	Freestream	ASZ	RANS

## Meshing and Wall Treatment

Due to the implicit filtering based on the mesh size, the resolution of the grid has a direct influence on the filter width  $\Delta$ . The smaller the mesh elements, the smaller

the turbulent structures that are resolved and the less is modeled by the subgrid scale model. Subsequently the overall accuracy increases with a higher mesh density. Assessing a proper turbulence modeling, the ratio of modeled turbulent kinetic energy  $k_{SGS}$  to the resolved turbulent kinetic energy  $k_{Res}$  can be determined, as defined in Eq. 10.2. According to Pope [Pop] a minimum of 80% of the overall turbulent kinetic energy should be resolved:

$$\frac{k_{SGS}}{k_{SGS} + k_{Res}} < 0.2 \quad (10.2)$$

The energies  $k_{SGS}$  and  $k_{Res}$  are calculated following

$$k_{SGS} = \left( \frac{\nu_t}{C_s \Delta} \right)^2 \quad (10.3)$$

and

$$k_{Res} = \frac{1}{2} (u_i - \bar{u}_i)(u_i - \bar{u}_i) \quad (10.4)$$

with  $C_s \Delta$  representing a model constant of the SGS model.

The CFL number condition, controlling the time step size, was already introduced in section 2.1.6. Obviously, the time-step size has a major influence on the computational cost. Therefore, to enable feasible calculations, it has to be increased without impacting the stability and the accuracy. As a consequence, a time step size of  $\Delta t = 5e^{-6}$ s was chosen which leads to  $ACFL < 4$  in the finest regions of the mesh.

### Convergence criteria

For the LES simulation the topic of the convergence is more complex than for RANS. Two different types of convergence have to be considered. On one side there are the inner iterations inside one time step which have to converge, and on the other the convergence relates to the achievement of a steady transient flow. A steady transient flow represents a flow field which is intrinsically unsteady but features a constant mean flow field. The convergence of the inner iterations was already introduced in chapter II. 8 inner iterations are found sufficient to achieve convergence in one time step using the unsteady implicit algorithm.

Due to the unsteadiness of the flow, the residuals, on which the convergence of the whole flow for the RANS calculation based, are not a good indicator for a converged LES solution. Instead several quantities of interest are monitored over the solution time. The mass imbalance,

$$\Delta \dot{m} = \dot{m}_{in} - \dot{m}_{out}, \quad (10.5)$$

calculating the difference between the inlet mass flow  $\dot{m}_{in}$  and the outlet mass flow  $\dot{m}_{out}$  is the most basic measure which is done. Additionally the integral of the turbulent kinetic energy over the whole domain is observed to determine when the flow reaches it's fully unsteady pattern. Pressure monitors on numerous discrete points are used to observe the instabilities in the flow. Similar to the RANS simulations,

averaged temperatures on planes are monitored, and convergence is indicated when the mean value reaches a steady state.

To wash out the settling effects after switching from RANS to LES, approximately three flow through times (of the combustor duct) were needed to reach a steady transient flow. This number varied slightly but proved to be a good reference value for the simulations. At this point the time step averaging was started and the simulation were run until the mean values reached a steady state (at least four flow through times).

## 10.2 Analysis of the non reacting operating point C

### 10.2.1 Settings and Mesh Validation

#### Mesh Validation

For a quantitative statement over the full domain, the mean values can be used in Eq. 10.2. This lead to a percentage of 88.9% of the turbulent kinetic energy that was resolved for the mesh with 2.2 million cells for case C. However, this percentage does not disqualify the presence of regions that are not well resolved. The contour plot in Fig. 10.3 shows the fraction of the turbulent kinetic energy that is resolved by the SGS model for the region of interest behind the bluff body, which was the only location where the fraction of 0.2 was exceeded partially with exception of cells in the vicinity of the walls. As a conclusion the mesh with 2.2 million cells was found the resolve the turbulent kinetic energy satisfactory.

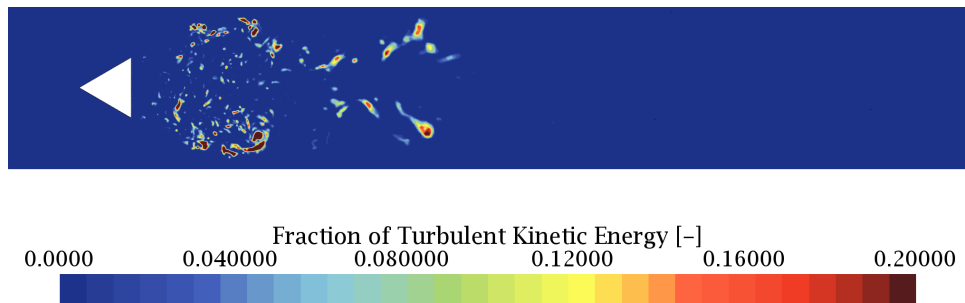


Figure 10.3: Fraction of the SGS Turbulent Kinetic Energy for case C

#### SGS Modeling

The WALE subgrid model was used as it is recommended by StarCCM+ and has numerous shown its performance.

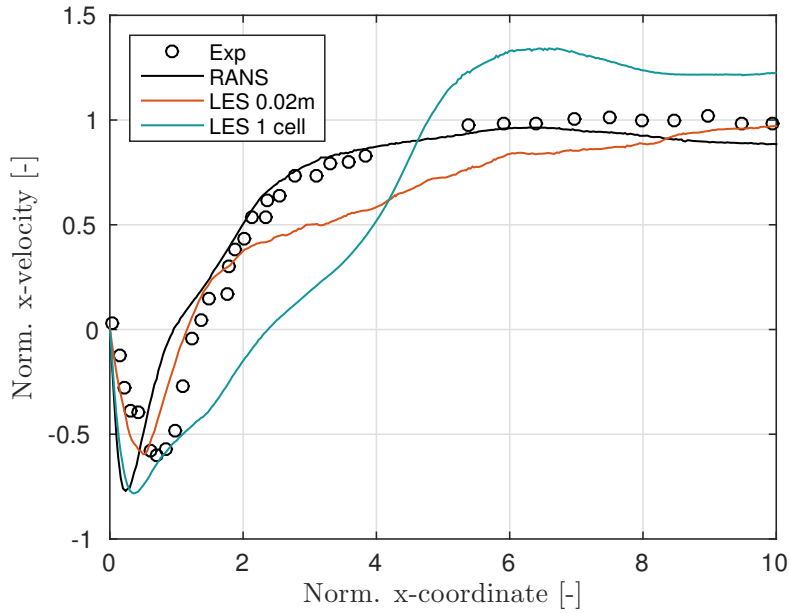
### 10.2.2 Averaged cold flow fields

Fig. 10.4 shows the mean axial velocity on the central axis M1 for three simulations. Results are normalized by the inlet velocity ( $s = 16.6 \text{ m s}^{-1}$ ) and the bluff body side

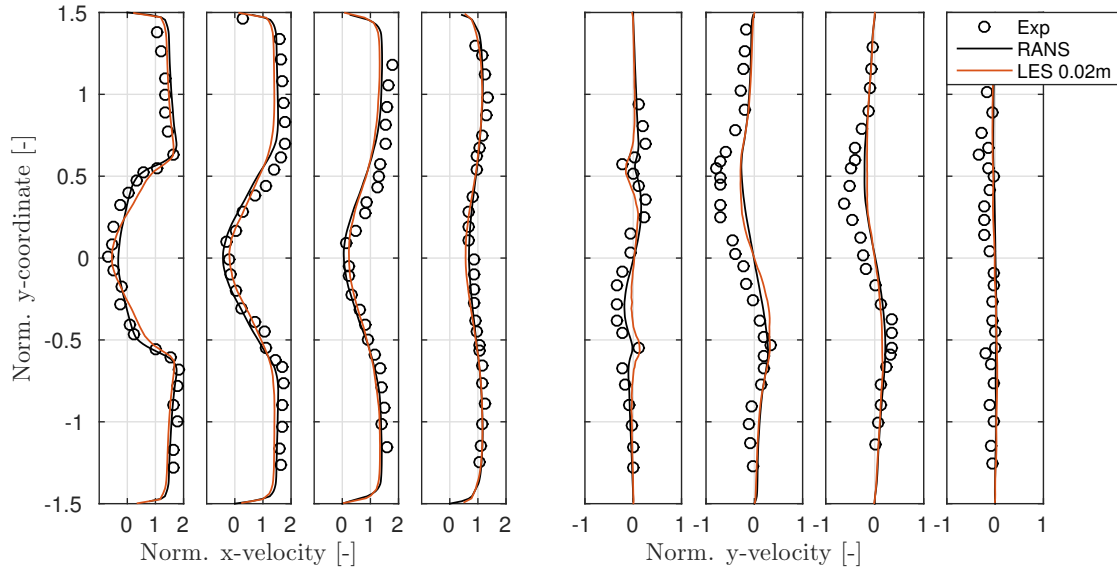
length ( $s = 40$  mm). The RANS simulation underpredicts the recirculation zone but is able to accurately predict the flow downstream of the bluffbody. In contrary, the LES result with the partial 3-D domain predicts the recirculation zone accurately and slightly underpredicts the axial velocity downstream. The quasi 2-D approach does not capture the flow field while overpredicting the recirculation zone and the velocity further downstream. Therefore this approach won't be contemplated below.

Fig. 10.5 shows the x and y-velocity profiles on M2-M5 for the RANS and the LES simulation with the partial 3D domain. The mean velocity profiles of the two simulations are almost equivalent in the vicinity of the walls. They differ slightly in the region behind the bluff body as the x-velocity profiles confirm the observations from the previous graph. While the RANS simulation slightly underpredicts the recirculation velocity in the center, the prediction around  $y_{norm} = \pm 0.5$  is accurate on M2. Further downstream the profiles of the LES and RANS calculation assimilate.

The assimilation is present in the y-velocity profiles as well. The simulations are able to predict the trend of the y-velocity on M1, without capturing the magnitude accurately. Further downstream the profiles almost equal again and underprediction of the y-velocity is present.



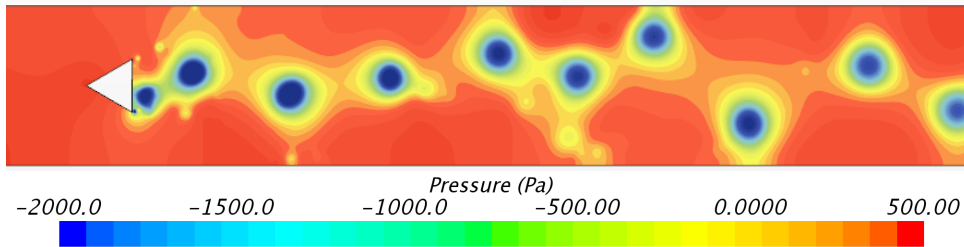
**Figure 10.4:** Mean axial velocity on the centerline M1 behind the bluff body for case C



**Figure 10.5:** Velocity profiles for case C. Left: Mean axial velocity on M2-M5. Right: Mean transverse velocity on M2-M5.

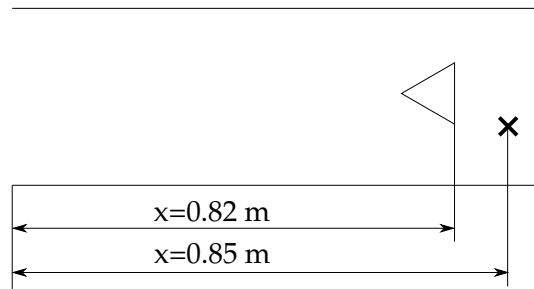
### 10.2.3 Unsteady flow field

Fig. 10.6 displays the fully developed asymmetric vortex shedding behind the bluff body. Periodically, vortices are detached from either side of the triangle. The vortices are visualized by the low pressure areas which travel downstream through the duct.



**Figure 10.6:** Evolution of the pressure contour for the non reacting case

To analyze the unsteady behavior of the flow, the shedding frequency of the vortices is studied. Therefore transverse velocity was recorded for different probe points in the partial 3-D domain. For a specific point behind the bluff body (Fig. 10.7) the velocity signal is shown at top right in figure 10.8. A Discrete Wavelet Transform (DWT) is performed which yields the spectral history of the signal (bottom right). The advantage over the Fast Fourier Transformation (FFT) at bottom left is the localization of frequencies in the time domain. The FFT shows a vortex shedding frequency of  $f = 116 \text{ Hz}$ , while the wavelet displays that the shedding frequency changes slightly in the time domain. Table 10.2 shows the comparison to the experiments and the results obtained by Ghani. Subsequently StarCCM+ is able to predict the experimentally derived vortex shedding frequency accurately



**Figure 10.7:** Location of the velocity probe

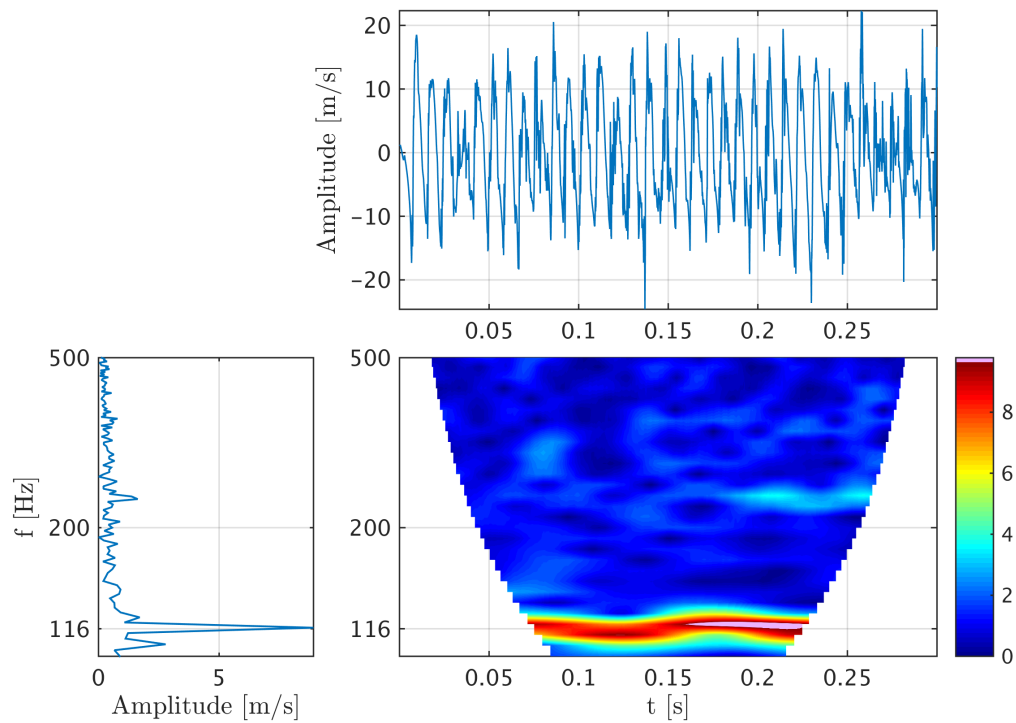


**Figure 10.8:** Shedding frequency analysis for case C. Top right: Transverse velocity signal behind the bluff body. Bottom right: DWT of the signal. Bottom left: FFT transform of the signal

**Table 10.2:** Vortex shedding frequencies for the experiment and LES simulations

	Frequency ( $Hz$ )
Experiment [SNM91]	105 Hz
Ghani et Al. [Gha15]	120 Hz
LES	116 Hz



## 10.3 Analysis of the reacting flow at low inlet velocity (Buzz mode)

### 10.3.1 Settings and Mesh Validation

#### Mesh Validation

Similar to case C, the mesh is validated in terms of the fraction of SGS turbulent kinetic energy which is resolved by the SGS model. Using the mean values leads to a quantitative statement with a percentage of 81.3% which is resolved by the 2.2 million cells mesh for case R. The contour plot is displayed in Fig. 10.9. It displays that similar to the cold flow, the Pope criterion is satisfied in the flow field, except for a few spots behind the bluff body. Overall the 2.2 million mesh was found to resolve the flow field satisfactory.

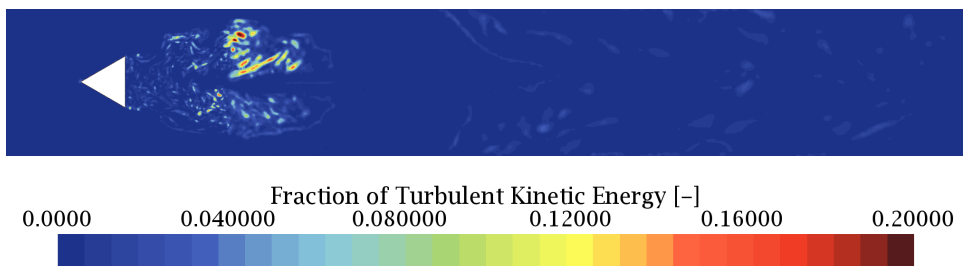


Figure 10.9: Fraction of the SGS Turbulent Kinetic Energy for case R

#### SGS Modeling

As a standard approach the WALE subgrid model is used. Additionally, a comparison to the Dynamic Smagorinsky model is done in Section 10.3.3.

#### Combustion Modeling

As introduced in section 2.1.3, two different approaches and mechanisms are tested in general. In the end, only the flamelet approach was applied successfully. Complex chemistry failed to deliver physical results during RANS tests and therefore is not used for LES. The primary approach is the kinetic rate approach with GRI-Mech as a chemical mechanism. In addition, the use of the turbulent flame speed closure and the San Diego mechanism will be discussed in section 10.3.3.

### 10.3.2 Influence of boundary condition treatment

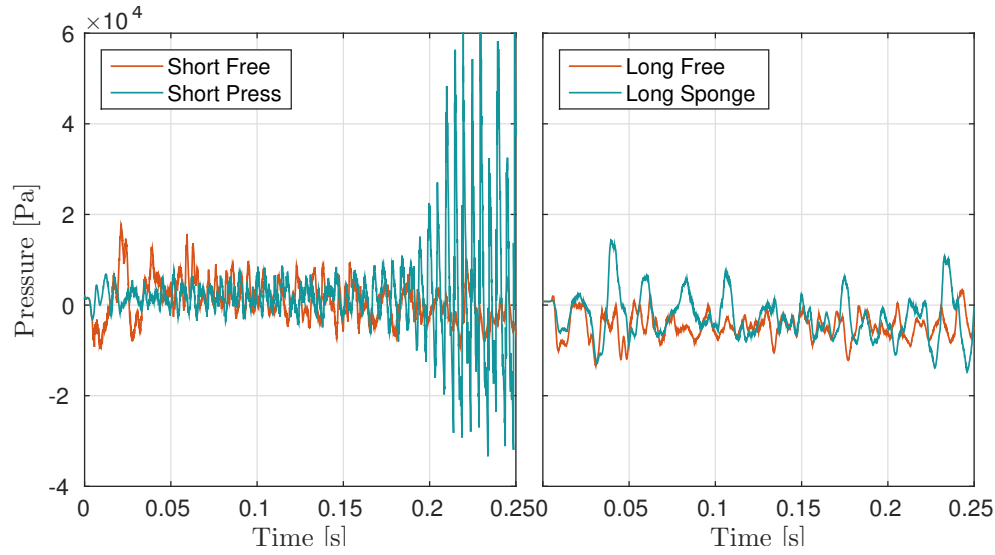
For the cold flow case, the fluctuation levels were as low that unphysical reflections of the fixed pressure outlet did not play a major role. However, for combustion cases the coupling of the pressure fluctuations and the heat release comes into play. This leads to higher fluctuations whose reflections can impact the flow and stability of the combustor. Therefore, the acoustics of the combustor have to be considered in this chapter. For different boundary conditions, the acoustics in the combustor vary as the reflective behavior enables or disables the acoustic perturbations to leave the computational domain. Case R is used in this section so subsequently the pressure fluctuations should remain low (Fig. 7.4) as no dominant frequencies are reported for this equivalence ratio.

Fig. 10.10 shows the pressure signal at point P (0.1, 0, 0 m) for different BCs. For the fixed pressure outlet the mean pressure remains constant and the fluctuations inside a certain limit until  $t = 0.2$  s. Up to this point the reflections of the outlet do not seem to have an influence on the fluctuation levels in the combustor, but then the fluctuations rise drastically up to amplitudes of 0.6 bar. This impacts the flow as the flame is not able to stay attached to the bluff body and is blown off.

Subsequently the next step was to use the acoustically non reflective freestream boundary condition. As it is sensitive to the mach number,  $Ma$  had to be tuned. Therefore, simulations with  $Ma = 0.8, 1.0, 1.25, 1.5$  and  $1.75$  were run to test if it is possible to impose a value for which the pressure does not drift (Fig. 10.11). All mach numbers but  $Ma = 1.75$  (Fig. 10.10) lead to a drift of the pressure in the combustion chamber. Even for this mach number the pressure is still slightly drifting. For the other mach numbers the drift is not even settling into a stable mean pressure after some time. The pressure keeps on drifting.

The tuning of the Mach number is time-consuming and requires considerable computational effort. In consequence this is not an approach that is favorable for future works. The advanced approach, the extension of the discharge duct, was already presented in section 10.1 and will be presented with a RANS result patched onto the outlet and a sponge which is applied to the discharge duct. Both simulations run with the larger domain achieved to avoid the pressure drift. The sponge displayed here had a strength of  $k = 2000$  and the sponge region spanned over half of the long discharge duct. Even though these simulations were able to hold the mean pressure constant, their fluctuation levels differ. The sponge introduces unphysical low frequency oscillations ( $f = 50$  Hz) with higher amplitudes than they are expected. For both simulations without the sponge (constant  $Ma$  and RANS result), the frequency of the simulation resembles the eigenfrequency of the combustor ( $f = 95$  Hz). The amplitudes of the fluctuations after settling are similar with values around  $p_{RMS} = 1$  bar.

The dynamic behaviour is analyzed in more detail in section 10.3.4.



**Figure 10.10:** Case R: Pressure evolution for different boundary conditions. Left: Short domain. Right: Long domain

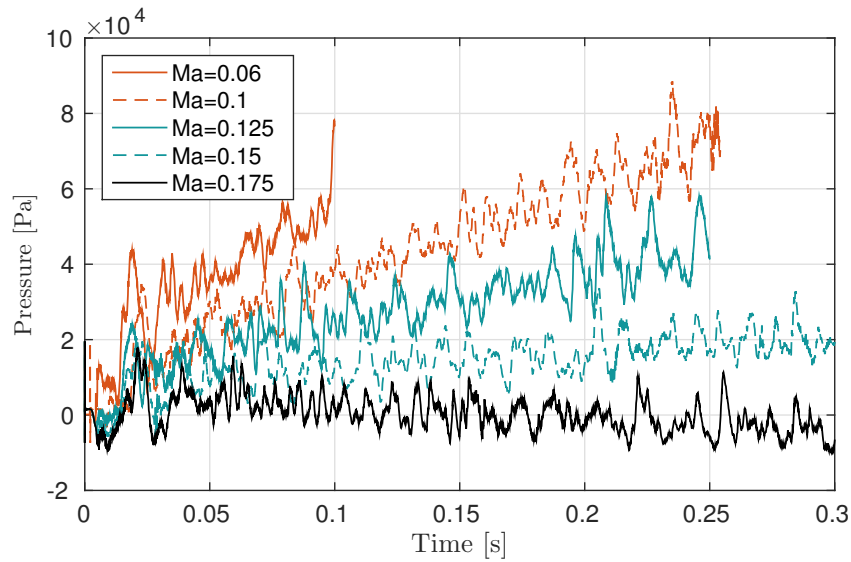


**Figure 10.11:** Case R: Pressure evolution for different mach numbers of the freestream condition

### 10.3.3 Averaged reacting flow fields

In the coldflow case, StarCCM+ has already shown its capability to model turbulent flows. Now, the capabilities towards the prediction of a reactive flow are assessed for Case R (Tab. 7.1). Fig. 10.12 displays the mean axial velocity on M1 behind the bluff body. None of the simulations is able to capture the full flow field accurately. The RANS simulation is able to predict the velocity further downstream, but is not able to capture the recirculation zone. The LES calculations overestimate the acceleration downstream and the recirculation zone is predicted to short. Differences between the different boundary conditions are hardly reflected in the flow fields in contrary to the domain size. However, results differ slightly as the recirculation velocity is higher and the acceleration downstream less when the long discharge duct is used.

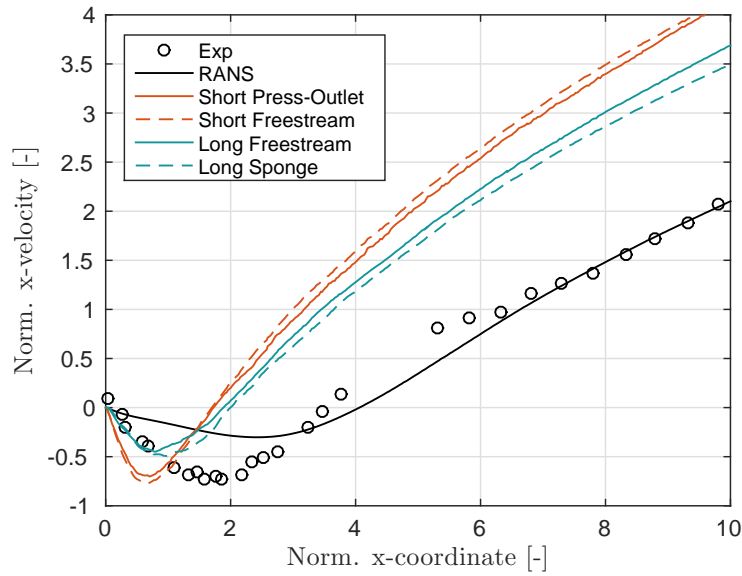


**Figure 10.12:** Mean axial velocity on the centerline M1 behind the bluff body for case R

The mean  $x$ - and  $y$ -velocities on the planes M2-M5 are shown in Fig. 10.12. It's noticeable how well the RANS calculation is able to predict the flow field further downstream (M5). Directly behind the bluff body the recirculation velocity is underestimated. In general, one can observe that the shape of the velocity profile for the LES calculation is too smooth, while for the RANS calculation, the gradient between the recirculation zone and the area that is not directly affected by the bluff body, is captured.

The temperature profiles express the nature of the different simulations (Fig. 10.14). While the RANS calculation displays a clear boundary between the burnt and unburnt zones this is different for the LES calculations. The flame moves and therefore the gradient of the mean temperature is flattened. However, the temperature profiles are not captured accurately and one may observe that for the LES calculations the temperatures are too high further downstream (M6 and M7), especially in vicinity

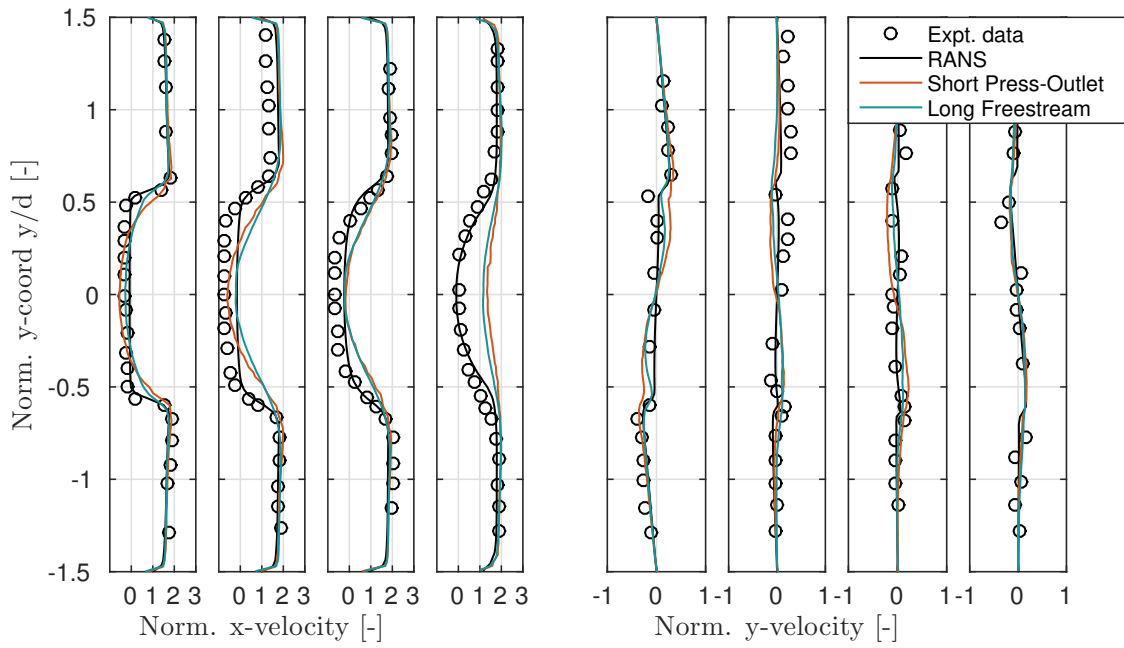


**Figure 10.13:** Velocity profiles for case R. Left: Mean axial velocity on M2-M5. Right: Mean transverse velocity on M2-M5

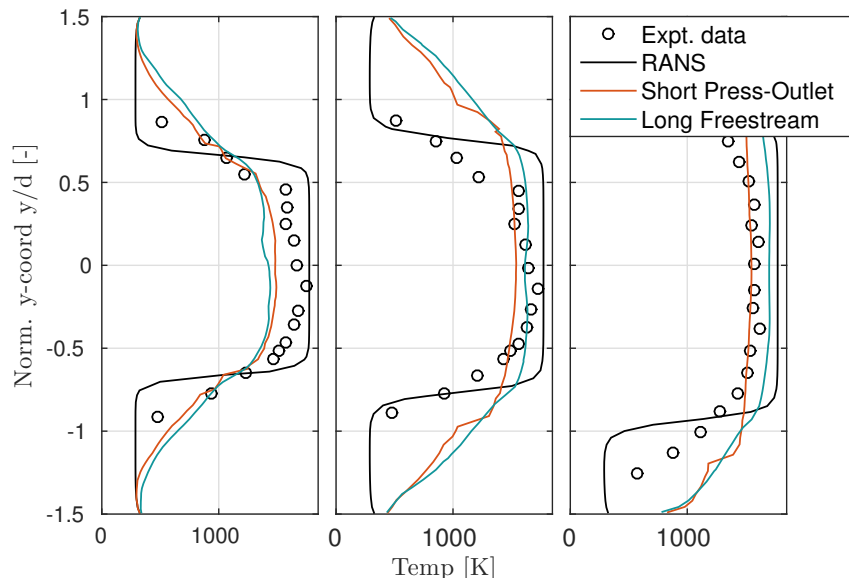


**Figure 10.14:** Temperature profiles on M5-M7 for case R

of the walls. This is the reason for the overestimation of the axial velocity downstream as the increased combustion leads to a higher volume flow rate and subsequently a higher axial velocity. As a conclusion, the predicted efficiency of the combustor was too high. Instead of an efficiency of approximately 40% (Experiments), 90% of the fuel is burned at the dischargement into the larger duct. Fig. 10.15 displays the flame shape for case R. Worthy of remark is the switch from a asymmetric vortex shedding in the cold flow to a symmetric vortex shedding in the reactive flow. This is a common phenomena that has been observed for bluff body stabilized flames before [Fur00][CSS13].

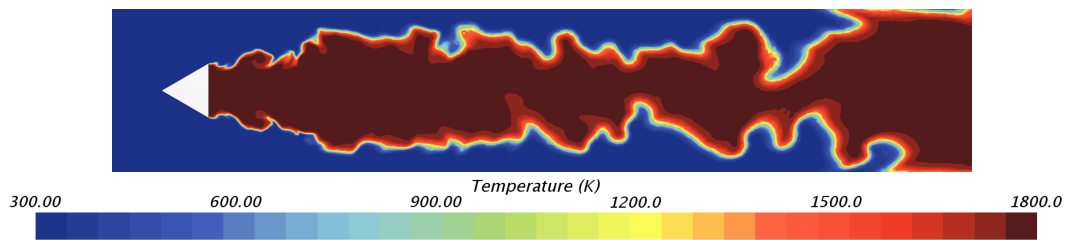


**Figure 10.15:** Flame shape for the LES simulation with the long domain and a freestream outlet

As this deviations are obviously not satisfactory, different approaches were made to improve the solution of flow fields.

### Influence of the combustion modeling

As the cold flow velocities were predicted accurately, the main suspect of the deviations is the combustion modeling.

The first step was to use the San Diego mechanism instead of GRI-Mech as it is specifically validated for propane combustion. However, this approach resulted in blow off of the flame and could not be applied successfully. An alternative closure for the FGM approach is the turbulent flame speed closure which offers a tuning factor to adjust the combustion. Applying this closure lead to a similar behaviour as for the San Diego mechanism and the flame was blown off (Fig. 10.16).

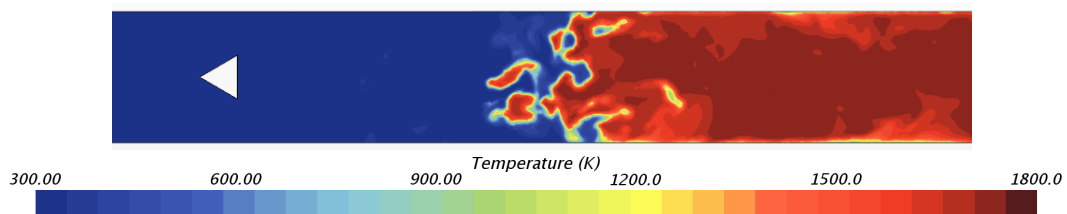


**Figure 10.16:** Case R, TFC: Blowoff of the flame

The outcome of this section is not satisfactory. Further work has to be done into this topic as the prediction of mean flow fields and combustion behaviour is a key point for CFD for combustors.

### Influence of the SGS modeling

Another suspect for the deviations was the used SGS model. Fig. 10.17 shows a comparison of the WALE and the Dynamic Smagorinsky model for the long discharge duct with a RANS solution patched onto the outlet. No improvement was observed for the use of a different SGS model. Instead the acceleration even slightly increased while the deviations are in general small.

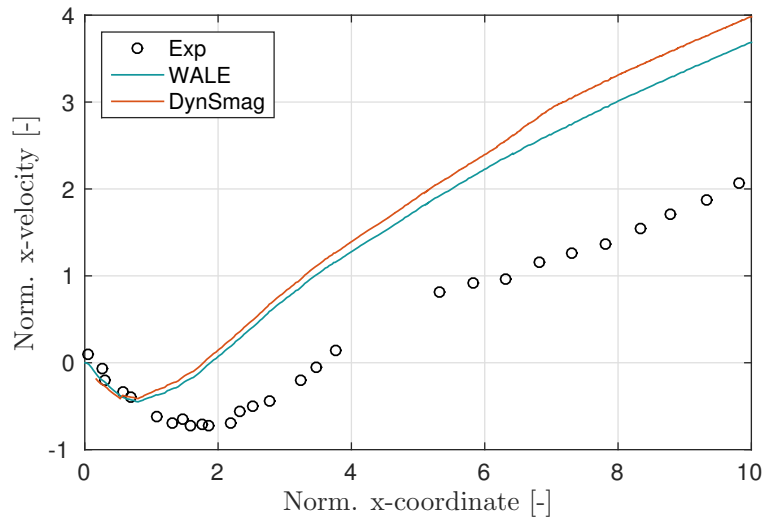


**Figure 10.17:** Case R: Mean axial velocity on M1 for WALE and Dynamic Smagorinsky SGS modeling

### 10.3.4 Dynamic behaviour for varying equivalence ratios

The sensitivity of the fluctuation levels to the equivalence ratio has already been stated. This section aims to investigate if StarCCM+ is able to predict the complex coherences that lead to the excitement of those. Therefore three different operating points are investigated (Table 10.3) and compared for the short combustor with a freestream condition imposing a constant  $Ma$ . Additionally, as the unstable operating points are investigated now, the frequencies inside the combustors will be investigated closely and the corresponding modes visualized.

**Table 10.3:** Case B: Investigated operating points with  $p_{RMS}$  reported from the experiments for  $x = 0.85$  m

Case	$\phi[-]$	$p_{RMS}[bar]$
R	0.65	1
B <sub>1</sub>	0.95	1.8
B <sub>2</sub>	1.05	4.5

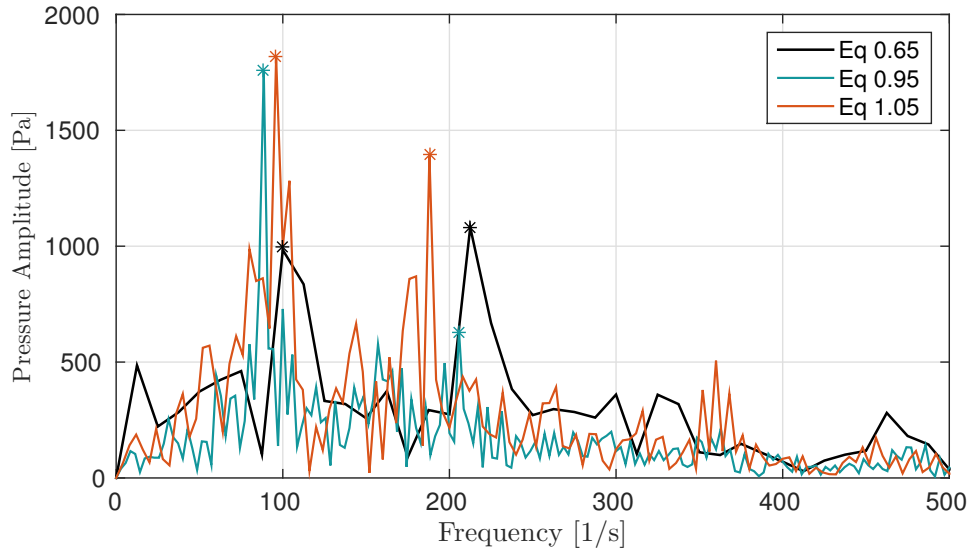
Figures 10.18 and 10.19 show FFTs for each of the three equivalence ratios for probes at  $x = 0.1$  m and  $x = 0.85$  m respectively. For the reacting stable case both the first and the second longitudinal mode appear to be excited weakly. The fluctuation levels are low corresponding to the observations reported from the experiments. Further downstream, at the bluff body, only the second longitudinal mode can be observed.

Increasing the equivalence ratio to the value for the buzz case, the 1L mode becomes clearly dominant at  $x = 0.1$  m. Same pattern can be seen at the bluff body as the 1L mode, in contrary to case R, is visible now. Noteworthy is the comparison of the magnitude in pressure amplitudes for both modes. The variation can be directly linked to the mode shapes that were derived in Comsol as the 2L modes has the same pressure amplitude for both measurement locations while the amplitude for the 1L mode sinks to around a third from  $x = 0.1$  m to  $x = 0.85$  m.

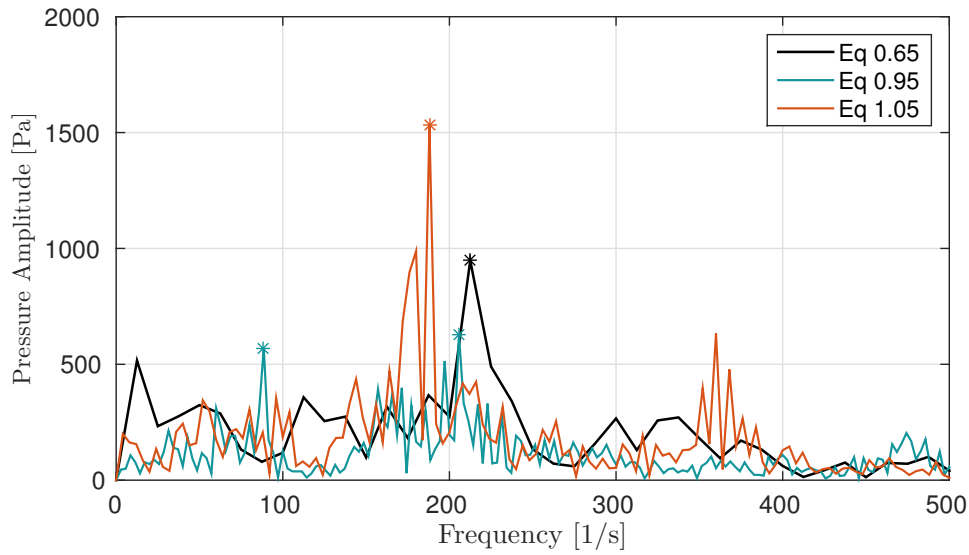
Changing to case B<sub>2</sub> the 2L mode reinforces again. While the magnitude of 1L mode only increases slightly, the 2L mode almost reaches 1500 Pa. Subsequently the 2L mode is clearly dominant behind the bluff body.

The conformity in the change of the magnitudes for the different measurement locations has already been mentioned. Fig. 10.20 displays a comparison of the modeshapes derived by Comsol and the modeshapes from the LES simulations of case B. The modeshapes were derived by the use of a 2-D FFT (Fig. 10.21) over the central plane of the combustor for the analogue frequencies. In general, the form of the shapes matches very well. The 1L mode is captured accurately until the bluff body. From there on, the shape differs as it seems to be slightly disturbed. The 2L mode is captured over the whole combustor duct. The only deviation is manifested in slight downstream shift of the pressure node. A possible reason for this is the simplification of the temperature profile for the Comsol approach.

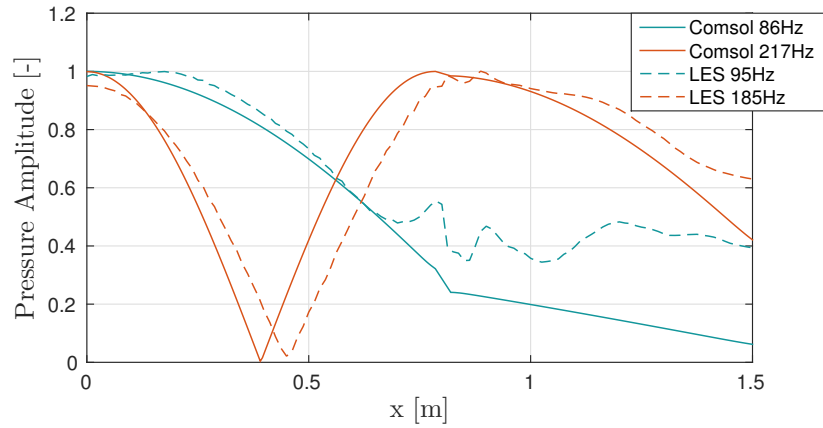




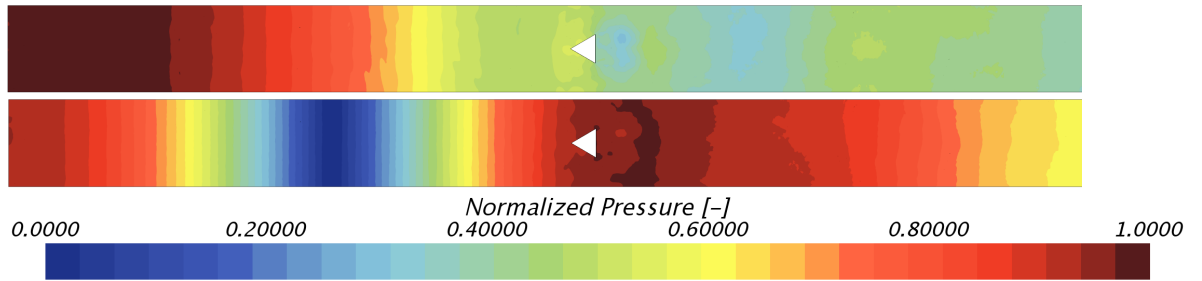
**Figure 10.18:** Case R,  $B_1$  and  $B_2$ : FFT's for different equivalence ratios  $\phi$  at  $x = 0.1$  m



**Figure 10.19:** Case R,  $B_1$  and  $B_2$ : FFT's for different equivalence ratios  $\phi$  at  $x = 0.85$  m



**Figure 10.20:** Comparison of the modeshapes of the LES for  $\phi = 0.95$  and Comsol



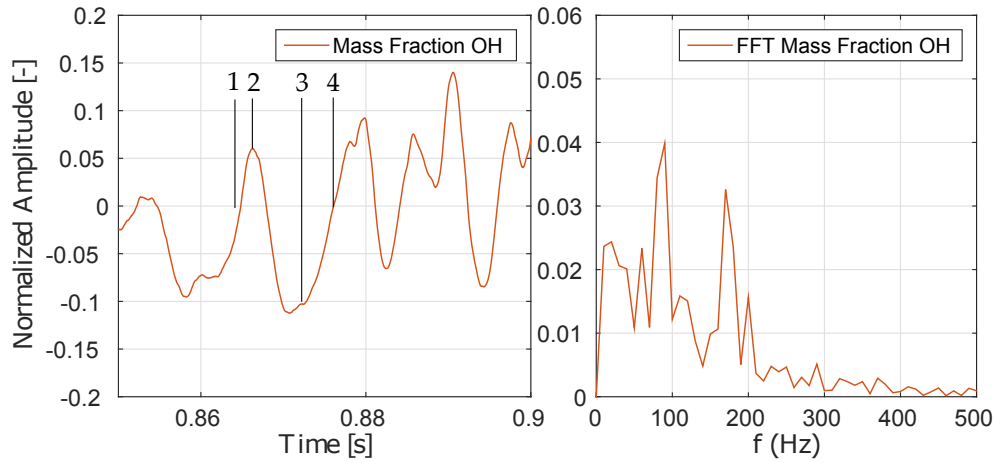
**Figure 10.21:** Surface FFT for the 1L mode (top) and the 2L mode (bottom)

Fig. 10.22 shows the heat release for case B<sub>1</sub>. As no simple measure of heat release is available for the FGM approach in StarCCM+, the volume integral of the mass fraction of OH is used as an indicator. The integral is evaluated for a region behind the bluff body. The FFT of the heat release (Fig. 10.22) reveals that the heat release is not strictly following the dominant frequency of pressure measurements close to the combustion region (Fig. 10.19). Instead, the heat release fluctuates with a superposition of the 1L and the 2L mode with the 1L mode being slightly dominant.

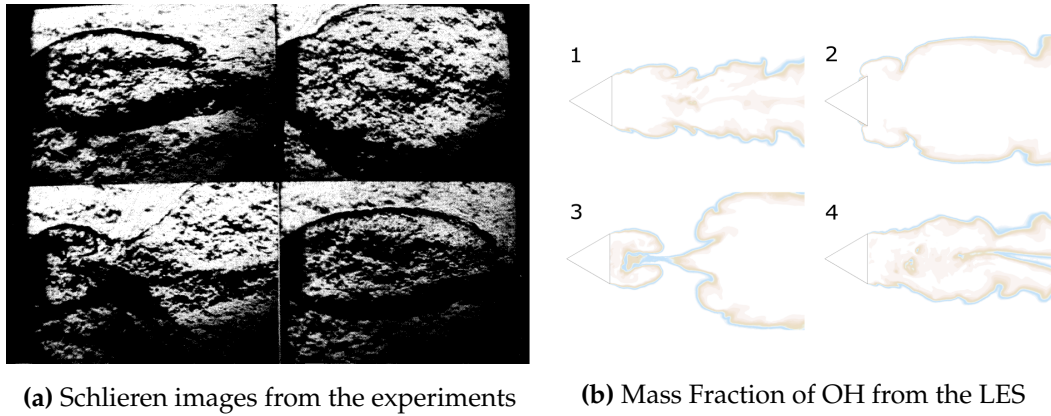
The oscillating flame front behind the bluff body was visualized by Schlieren images of Sjunnesson et Al. [APC92]. A comparison to the simulation results is shown in Fig. 10.23, visualizing the flame front at four distinct instantaneous snapshots of the oscillation phase (Fig. 10.22).

At the point of the maximum heat release, the flame front stands almost perpendicular to the main flow and even moves in front of the bluff body edges. At minimum heat release, the flame is shed symmetrically and the two reacting layers interact on the centeraxis. This movement of the flame can be explained by the pressure fluctuations causing the shear layers to roll up. Subsequently the heat release fluctuates and feeds back energy into the pressure oscillations.

As a conclusion for the investigation of the low-frequency oscillations, Fig. 10.24 displays the RMS values for both experiments and LES. It has to be noted that



**Figure 10.22:** Case B<sub>1</sub>: Left: Mass fraction of OH indicating heat release. Right: FFT of mass fraction OH.



**(a)** Schlieren images from the experiments

**(b)** Mass Fraction of OH from the LES

**Figure 10.23:** Visualized flame fronts of the experiments and the simulations

the points for the LES simulations correspond to the probe at  $x = 0.1$  m and the measurement of the experiments to  $x = 0.85$  m. Subsequently the magnitude can not be compared directly. However, the increase of the fluctuations from the low to the higher equivalence ratios is captured qualitatively. Only the sudden jump to the highest equivalence ratio of  $\phi = 1.05$  is not predicted.

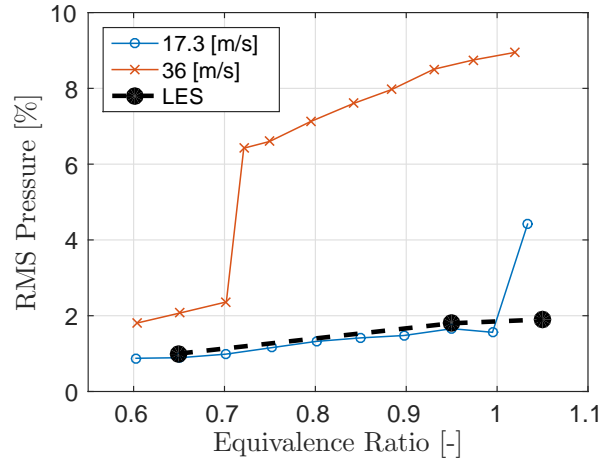


**Figure 10.24:** RMS value of the pressure for different equivalence ratios and inlet velocities and results obtained by the LES simulations for  $u_{in} = 17.3 \text{ m s}^{-1}$

## 10.4 Analysis of the reacting flow at high inlet velocity (Screech mode)

### 10.4.1 Numerical Settings

In the experiments, Screech, indicating high-frequency transverse fluctuations, occurred at an inlet velocity of  $u = 36 \text{ m s}^{-1}$ . In general, the settings in this section correspond to the settings which were used in the previous simulations. However, some modifications had to be done.

Due to the transverse mode, the partial 3-D domain does not satisfy the requirements to approach this case. Therefore simulations of the full 3-D domain with approximately 22 million cells had to be done. The long discharge duct is used as good experiences were made without the need of tuning during the investigations of the previous cases.

The freestream BC could not be applied successfully in this case as it lead to significant pressure reduction at the outlet and eventually divergence of the solver. Therefore, despite its reflective character, the fixed pressure BC had to be used. Additionally, to increase the stability, the time step was decreased to  $\Delta t = 1e^{-6} \text{ s}$ . Two operating points are investigated for the high inlet velocity (Tab. 10.4).

**Table 10.4:** Case S: Investigated operating points with  $p_{RMS}$  reported from the experiments for  $x = 0.85 \text{ m}$

Case	$\phi[-]$	$p_{RMS}[\text{bar}]$
S <sub>1</sub>	0.72	4
S <sub>2</sub>	0.85	7.5

### 10.4.2 Dynamical behaviour for varying equivalence ratios

Fig. 10.25 shows the flame shape behind the bluff body for the full combustor, displayed by an isosurface of  $Y_{OH} = 0.01$ . The recirculation zone can be detected clearly, indicated by the blue contour. Additionally the symmetric vortex shedding, already displayed for case B, is present.

Unfortunately, after a simulation time of  $t = 0.05$  s no high frequency oscillations could be detected for case  $S_1$ . Subsequently the equivalence ratio was increased to  $S_2$  as the first operating point is located in the region of high gradient in terms of the RMS pressure (Fig. 7.4). The simulation was then run up to  $t = 0.15$  s.

Fig. 10.26 shows a FFT of a pressure signal at point P [0.1, 0, 0 m]. This corresponds to a location close to antinodes for both the possible candidates (1L-1Ty-0Tz and 1L-0Ty-2Tz) which have been derived by Comsol. However, instead of the reported high frequency oscillation, the 2L mode, which was already observed for the buzz case, is excited.

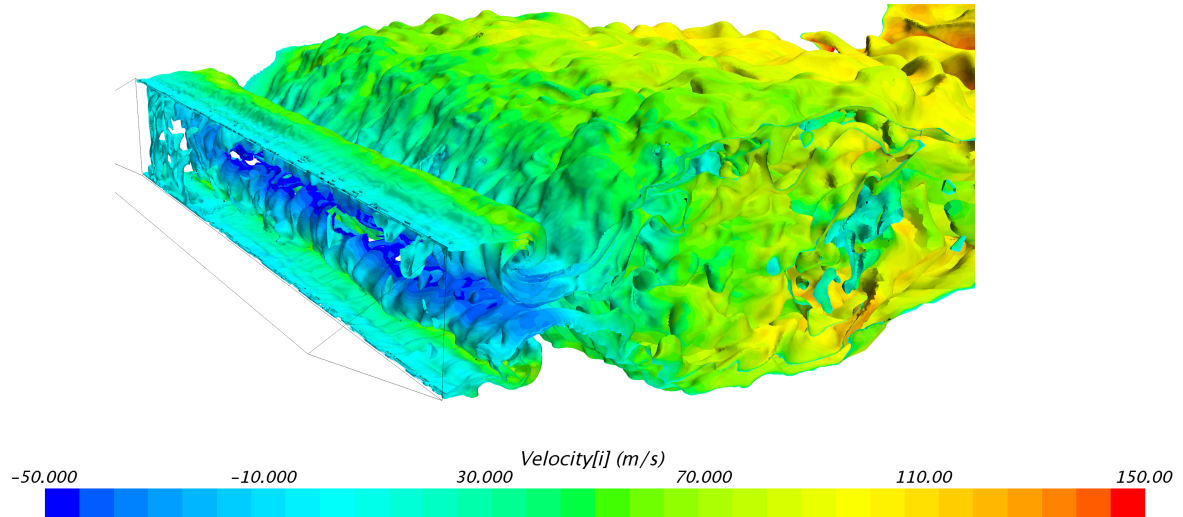
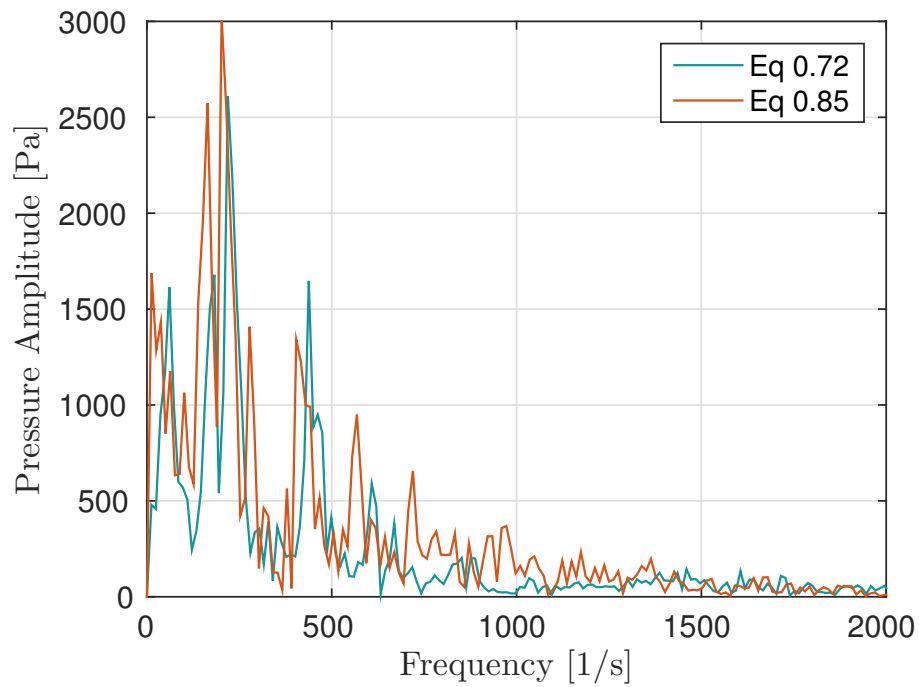


**Figure 10.25:** 3D image of an isosurface for  $Y_{OH} = 0.01$  with the color indicating the axial velocity for case S

### 10.4.3 Scalability of StarCCM+ on JURECA

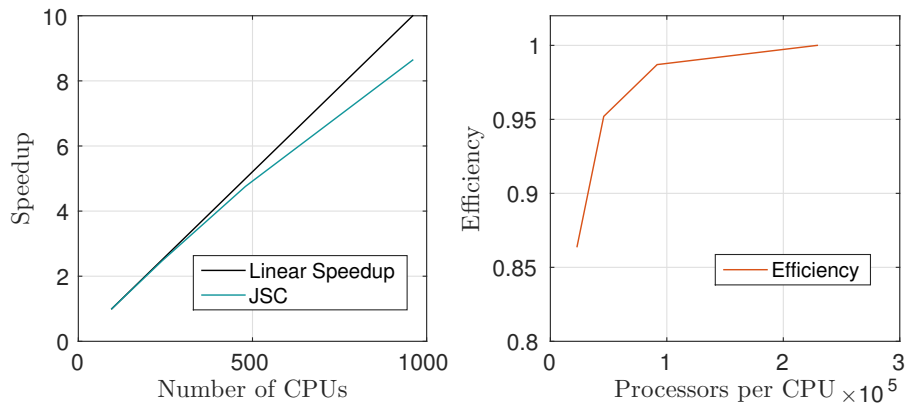
Due to the enormous computational effort of this simulation and the temporal shortage of licenses, part of it had to be run on the HPC JURECA in Jülich [Jue16] which provided the necessary amount of processors. Similar to the vortex preservation test case, a performance test was done for 96, 240, 480, 960 processors. Higher numbers of processors were requested as well, but simulations did not run for CPU numbers > 1000.

Fig. 10.27 shows the results of this test. Hereby the Speedup factor of 1 and an efficiency of 1 correspond to the computation with 96 processors. Up to 500 processors, or around 45000 cells per processor, the Speedup is close to linear and the efficiency still lies around 95%. For lower numbers of cells per processor the efficiency



**Figure 10.26:** Case S: FFT of a pressure signal at P [0.1, 0, 0 m]

sinks considerably and subsequently only should be used if the overall time is more important than the costs. This number is close to the recommendation that was done during the test cases (25000 cells per processor).



**Figure 10.27:** Speedup and Efficiency of StarCCM+ on JURECA

## Chapter 11

# Conclusion and Outlook

### 11.1 Conclusion

In the present work, the LES approach in StarCCM+ has been studied by means of generic test cases and the Volvo validation rig.

At first the numerical accuracy and the boundary conditions were assessed in a vortex preservation and an acoustic wave propagation test. Various models were tested and settings to achieve accurate results in reasonable time were derived. Boundary conditions, which are crucial for thermoacoustics, were investigated on a simplified 1-D duct and the freestream condition was found to be acoustically non-reflecting with the limitation of a strong sensitivity for the flow field.

As a next step, the insight was transferred to the analysis of the academic Volvo case. RANS investigations were performed showing considerable accuracy far from the bluff body for a non reactive and a reactive case, while they were not able to capture the flow field in the intrinsically unsteady regions of the recirculation zone. For the LES approach, the capability to capture the unsteady structures, the vortex shedding frequency and the mean flow field was verified by studying the non reacting operating point. For the reportedly stable reactive operating point the acceleration downstream was overestimated and the flow fields could not be predicted accurately as the combustor efficiency was overpredicted. Different approaches did not lead to an improvement for the prediction of this issue. Diverse boundary conditions and the change of the SGS model showed minor influences on the flow fields. Variation of the combustion modeling or chemical mechanisms, two major issues which have been investigated, could not be applied successfully.

LES predictions of the dynamic behaviour evidenced longitudinal low frequency instabilities. Both the reported 1L mode with an accurate prediction of the frequency and a 2L mode were observed. Modeshapes derived by the LES data coincided with results of an acoustic analysis based on a simplified approach done in Comsol Multiphysics. The coherence of the equivalence ratio and the rise in magnitude of the instabilities could be predicted qualitatively up to  $\phi = 1$ . For higher ratios the sudden increase of the instabilities could not be observed.

Utilizing the full 3-D domain with 25 million cells, computations targeting the

high-frequency transverse modes evidenced in the experiments could not be predicted by StarCCM+ as no dominant transverse fluctuations were observed.

Additionally scalability test were performed for both the generic test cases on the Siemens cluster and the Volvo validation rig on Jureca. The tests revealed a scalability up to 1000 processors and a recommendation of a minimum cell count of 25000 per processor is concluded to achieve a compromise amongst efficiency and speed.

## 11.2 Outlook

While this work constitutes a comprehensive evaluation of LES in StarCCM+, particular drawbacks offer material for further investigations in future work.

The test cases were performed with structured grids to enable a direct comparison to other codes. However the mesh used in this work was polyhedral. For a full evaluation of the dissipative and dispersive behavior of the models testing polyhedral meshes might be of value.

While the experimental results of the non reactive cases could be met satisfactory, the results for the reactive cases showed some differences. In particular the combustion modeling needs further investigation as the efficiency of the combustor was overpredicted. Subsequently the flow fields showed differences to the experimental results. The utilization of different combustion models or closures for the used flamelet approach and chemical mechanisms offers a broad field for further work and should be targeted for meaningful LES of combustion devices.

While this work showed that the study of acoustics is possible with StarCCM+, a different behavior in terms of combustion would probably modify the acoustics in the combustion devices. Therefore further investigations based on an accurate combustion modeling would improve the chances to capture the thermoacoustics not only qualitatively but also quantitatively.

The approach used in Comsol Multiphysics was a simplistic approach. The next step which would be possible is the introduction of an accurate RANS temperature field or even the use of linear euler equations taking into account the flow field.



# Bibliography

- [AG16] Siemens AG. "Siemens sets new world records at Duesseldorf power plant Fortuna". 2016. URL: <https://www.siemens.com/press/en/feature/2014/corporate/2014-02-lausward.php>.
- [Age17] International Energy Agency. "World Energy Outlook 2017". 2017.
- [APC92] Sjunnesson A., Henrikson P., and Lofstrom C. "CARS measurements and visualization of reacting flows in a bluff body stabilized flame". In: *28th Joint Propulsion Conference and Exhibit AIAA 92-3650* (1992).
- [BAS15] BASREC. "The development of electric transport - Its effect on the security of the electrical energy system and forecasting energy demand in chosen 8 BASREC countries". 2015.
- [Bou87] J. Boussinesq. "Théorie de l'écoulement tourbillant". In: *Mém. Présentés par Divers Savants Acad. Sci. Fr., Vol 23.46-50* (1887).
- [CB80a] J.Y. Chung and D. A. Blaser. "Transfer function method of measuring in-duct acoustic intensity in a duct system with flow". In: *Journal of the Acoustical Society of America* 68, 1570-1577 (1980).
- [CB80b] J.Y. Chung and D. A. Blaser. "Transfer function method of measuring in-duct acoustic properties. I. Theory." In: *Journal of the Acoustical Society of America* 68, 907-913 (1980).
- [CC13] Intergovernmental Panel on Climate Change. "Climate Change 2013: The Physical Science Basis". 2013.
- [CM94] H. Choi and P. Moin. "Effects of the computational time step on numerical solutions of tubulent flow". In: *Journal of Computational Physics*, 113:1-4 (1994).
- [CSS13] Peter Cocks, Vaidyanathan Sankaran, and Marios Soteriou. "Is LES of reacting flows predictive? Part 1: Impact of numerics". In: *51st AIAA Aerospace Sciences Meeting including the New Horizons Forum and Aerospace Exposition*. American Institute of Aeronautics and Astronautics, 2013. DOI: [10.2514/6.2013-170](https://doi.org/10.2514/6.2013-170).
- [DSG14] Laera D., Camporeale S.M., and Campa G. "Application of a Weakly Non-Linear Analysis to the Analysis of Thermoacoustic Combustion Instabilities". In: *Proceedings of the COMSOL Conference 2014* (2014).
- [EC11] Fedina E. and Fureby C. "Combustion LES of CESAR Multi-Burner Annular Combustor". In: *49th AIAA Aerospace Meeting* (2011).

- [Eds15] Lennart Edsberg. *Introduction into Computation and modeling for differential equations*. Wiley-Interscience, 2015.
- [Ehr03] Klaus Ehrenfried. "Vorlesungsskript: Stroemungsakustik I". 2003.
- [ERAEB05] Hesham El-Rewini and Mostafa Abd-El-Barr. *Advanced Computer Architecture and Parallel Processing*. John Wiley & Sons, Inc., 2005.
- [F.08] Durst F. *Fluid Mechanics: An Introduction to the Theory of Fluid Flows*. Springer Berlin Heidelberg, 2008.
- [FF99] Ducros F. and Nicoud F. "Subgrid-Scale Stress Modeling based on the Square of the Velocity Gradient Tensor". In: *Flow, Turbulence and Combustion, Volume 62, Issue 3*, pp 183-200 (1999).
- [FFT] Ducros F., Nicoud F., and Poinso T. "Wall-Adapting Local Eddy-Viscosity models for simulations in complex geometries".
- [FL94] C. Fureby and C. Lofstrom. "Large-eddy simulations of bluff body stabilized flames". In: *Symposium (International) on Combustion 25.1* (1994), pp. 1257–1264. DOI: [10.1016/s0082-0784\(06\)80766-6](https://doi.org/10.1016/s0082-0784(06)80766-6).
- [Flu] "FLUENT 6.3 Users Guide". URL: [https://www.sharcnet.ca/Software/Fluent6/html/ug/main\\_pre.htm](https://www.sharcnet.ca/Software/Fluent6/html/ug/main_pre.htm).
- [FOM86] Steve C. Frautschi, Richard P. Olenick, and Tom M. "The Mechanical Universe: Mechanics and Heat". In: *Camebridge University Press* (1986).
- [FP02] Ferziger and Peric. *Computational Methods for Fluid Dynamics*. Springer-Verlag Berlin Heidelberg NewYork, 2002.
- [Fur00] C. Fureby. "A computational study of combustion instabilities due to vortex shedding". In: *Proceedings of the Combustion Institute 28.1* (2000), pp. 783–791. DOI: [10.1016/s0082-0784\(00\)80281-7](https://doi.org/10.1016/s0082-0784(00)80281-7).
- [Fur17] Christer Fureby. "A Comparative Study of Large Eddy Simulation (LES) Combustion Models applied to the Volvo Validation Rig". In: *55th AIAA Aerospace Sciences Meeting*. American Institute of Aeronautics and Astronautics, 2017. DOI: [10.2514/6.2017-1575](https://doi.org/10.2514/6.2017-1575).
- [GBB04] Eugenio Giacomazzi, Valerio Battaglia, and Claudio Bruno. "The coupling of turbulence and chemistry in a premixed bluff-body flame as studied by LES". In: *Combustion and Flame 138.4* (2004), pp. 320–335. DOI: [10.1016/j.combustflame.2004.06.004](https://doi.org/10.1016/j.combustflame.2004.06.004).
- [GF01] B.J. Geurts and J. Froehlich. "Numerical effects contaminating LES, a mixed story". In: *Modern Stratigies for Turbulent Flow Simulation, chapter 16* (2001).
- [Gha+15] Abdulla Ghani et al. "LES of longitudinal and transverse self-excited combustion instabilities in a bluff-body stabilized turbulent premixed flame". In: *Combustion and Flame 162.11* (2015), pp. 4075–4083. DOI: [10.1016/j.combustflame.2015.08.024](https://doi.org/10.1016/j.combustflame.2015.08.024).

- [Gha15] Abdulla Ghani. "Simulation aux grandes echelles des instabilites de combustion transverses des flammes parfaitement premelangees et swirlees diphasiques". PhD thesis. CERFACS, 2015.
- [GMBS16] A. Ghani, M. Miguel-Brebion, and L. Selles. "Effect of wall heat transfer on screech in a turbulent premixed combustor". In: *Center for Turbulence Research; Proceedings of the Summer Program 2016* (2016).
- [Hep09] Martin Hepperle. "Electric Flight - Potential and Limitations". 2009.
- [HY09] Ying Huang and Vigo Yang. "Dynamics and stability of lean-premixed swirl-stabilized combustion". In: *Progress in Energy and Combustion Science Volume 35, Issue 4* (2009).
- [ISE13] Fraunhofer ISE. "Stromentstehungskosten Erneuerbare Energien, Studie November 2013". 2013.
- [Iss86] R. I. Issa. "Solution of the implicitly discretised fluid flow equations by operator-splitting". In: *Journal of Computational Physics, Vol 62 Issue 1* (1986).
- [Jam14] Antony Jameson. "Transonic Flow Calculations". In: *MAE Report 1651* (2014).
- [JE10] Guillaume Jourdain and Lars-Erik Eriksson. "Analysis of Thermo-Acoustic Properties of Combustors and Afterburners". In: *ASME Turbo Expo 2010: Power for Land, Sea, and Air* (2010).
- [JZA06] S. James, J. Zhu, and M. S. Anand. "Large-Eddy Simulations as a Design Tool for Gas Turbine Combustion Systems". In: *AIAA Journal, Vol. 44, No. 4, April 2006* (2006).
- [Kre12] Harman Krediet. "Prediction of limit cycle pressure oscillations in gas turbine combustion systems using the flame describing function". PhD thesis. University of Twente, 2012.
- [LC89] A. M. Lavardent and S. Candel. "Computation of diffusion and pre-mixed flames rolled up in vortex structures". In: *J. Prop. Power, 5:134-143* (1989).
- [Lee+16] Chin Yik Lee et al. "Nonlinear hydrodynamic and thermoacoustic oscillations of a bluff-body stabilised turbulent premixed flame". In: *Combustion Theory and Modelling* 20.1 (2016), pp. 131–153. DOI: [10.1080/13647830.2015.1118555](https://doi.org/10.1080/13647830.2015.1118555).
- [Li+16] Hua-Guang Li et al. "A Large-Eddy-Simulation Study of Combustion Dynamics of Bluff-Body Stabilized Flames". In: *Combustion Science and Technology* 188.6 (2016), pp. 924–952. DOI: [10.1080/00102202.2015.1136296](https://doi.org/10.1080/00102202.2015.1136296).

- [Lie+01a] T. Lieuwen et al. "A Mechanism for Combustion Instabilities in Premixed Gas Turbine Combustors". In: *Journal of Engineering for Gas Turbines and Power*, Vol. 123, No. 1, 2001, pp 182-190 (2001).
- [Lie+01b] T. Lieuwen et al. "A Mechanism of Combustion Instability in Lean Presmixed Gas Turbine Combustors". In: *J. ENg. Gas Turbines Power* 123(1):182-198,2001 (2001).
- [Lie05] Timothy C. Lieuwen. "Physics of Premixed Combustion-Acoustic Wave Interactions". In: *Combustion Instabilities In Gas Turbine Engines: Operational Experience, Fundamental Mechanisms, and Modeling, Progress in Astronautics and Aeronautics*, pp. 315-366 (2005).
- [Lie12] Tim Lieuwen. *Unsteady Combustor Physics*. Cambridge University Press, 2012.
- [LS13] E. Laurien and J. Stegmeier. *Numerische Stroemungsmechanik*. Springer Fachmedien, Wiesbaden, 2013.
- [Mae+17] Dario Maestro et al. "LES reliability of the Volvo bluff-body stabilized flame dynamics". In: *55th AIAA Aerospace Sciences Meeting*. American Institute of Aeronautics and Astronautics, 2017. DOI: [10.2514/6.2017-1576](https://doi.org/10.2514/6.2017-1576).
- [MD90] M.L. Munjal and A.G. Doige. "The two-microphone method incorporating the effects of mean low and acoustic damping". In: *Journal of Sound and Vibration (1990)* 137(1), 135-138 (1990).
- [MP92] Ulrich Maas and S. B. Pope. "Implementation of simplified chemical kinetics based on intrinsic low-dimensional manifolds". In: *Twenty-Fourth Symposium on Combustion/The Combustion Institute, 1992/pp*. 103-112 (1992).
- [MSD] San Diego Mechanism and University of California at San Diego. "Chemical-Kinetic Mechanisms for Combustion Applications". URL: <http://combustion.ucsd.edu>.
- [Olo92] S. Olovsson. "Combustion calculations on a premixed system with a bluff body flameholder". In: *AIAA-92-3470* (1992).
- [P.+10] Wolf P. et al. "Azimuthal instabilities in annular combustion chambers". In: *Center For Turbulence Research, Proceedings of the Summer Program 2010* (2010).
- [Pet00] N. Peters. *Turbulent Combustion*. Cambridge University Press, 2000.
- [Pit06] Heinz Pitsch. "Large-Eddy Simulation of Turbulent Combustion". In: *Fluid Mech.* 2006.38:453-482 (2006).
- [PK11] N.S. Park and S.C. Ko. "Large eddy simulation of turbulent premixed combustion flow around bluff body". In: *Journal of Mechanical Science and Technology*, 25:2227 (2011).

- [PL92] T. J. Poinso and S. K. Lele. "Boundary Conditions for Direct Simulations of Compressible Viscous Flow". In: *Journal of computational Physics* 101, 104-129 (1992).
- [Poi15] Thierry Poinso. "Computational Turbulent Combustion". In: *Princeton-CEFRS*. 2015.
- [Pop] Stephen B. Pope. *Turbulent Flows*. Cambridge University Press.
- [Por06] Porumbel. "Large Eddy Simulation of Bluff Body Stabilized Premixed Flame". In: *AIAA 2006-152* (2006).
- [PS72] S.V. Patankar and D.B. Spalding. "A calculation procedure for heat, mass and momentum transfer in three-dimensional parabolic flows". In: *nt. J. of Heat and Mass Transfer, Volume 15, Issue 10* (1972).
- [PV05] Thierry Poinso and Denis Veynante. *Theoretical and Numerical Combustion*. 2005.
- [Rah94] Erhard Rahm. *Mehrrechner-Datenbanksysteme - Grundlagen der verteilten und parallelen Datenbankverarbeitung*. Addison-Wesley-Verlag, 1994.
- [Ray78] J. W. Rayleigh. "The explanation of certain acoustic phenomena". In: *Nature*, 18 (455):319-321, 1878 (1878).
- [Rij59] Pieter L. Rijke. "On the vibration of the air in a tube open at both ends". In: *Philosophical Magazine, vol. 17, pages 419-422* (1859).
- [RKH67] Courant R., Friedrichs K., and Lewy H. "On the Partial Difference Equations of Mathematical Physics". In: *IBM J. 11. 215-234* (1967).
- [Roc+17] B. Rochette et al. "Influence of acoustic, chemistry description and wall heat transfer in LES of the Volvo bluff-body stabilized flame dynamics". In: (2017).
- [S.02] Candel S. "Combustion Dynamics and Control: Progress and Challenges". In: *Proceedings of the Combustion Institute, Vol. 29* (2002).
- [SHL09] Santosh Shanbhogue, Sajjad Husain, and Tim Lieuwen. "Lean blowoff of bluff body stabilized flames: Scaling and dynamics". In: 35 (Feb. 2009), pp. 98-120.
- [SHL92] A. Sjunnesson, P. Henrikson, and C. Lofstrom. "CARS measurements and visualization of reacting flows in a bluff body stabilized flame". In: *28th Joint Propulsion Conference and Exhibit*. American Institute of Aeronautics and Astronautics, 1992. DOI: [10.2514/6.1992-3650](https://doi.org/10.2514/6.1992-3650).
- [SK04] H.R. Schwarz and N. Köckler. *Numerische Mathematik*. Teubner, 2004.
- [Smi+] Gregory P. Smith et al. "GRI-Mech 3.0". URL: [http://www.me.berkeley.edu/gri\\_mech/](http://www.me.berkeley.edu/gri_mech/).
- [SNM91] A. Sjunnesson, C. Nelsson, and E. Max. "LDA Measurements of velocities and turbulence in a bluff body stabilized flame". In: *Proceedings of the 4th International Conference on Laser Anemometry* (1991).

- [SOS91] A. Sjunnesson, S. Olovsson, and B. Sjoblom. "Validation Rig - A tool for flame studies". In: *ISABE* (1991).
- [Sta] "StarCCM+ Theory Guide".
- [Toe17] Karl Toepperwien. "Assessment of thermoacoustic instabilities in a Siemens heavy-duty gas turbine combustor using Large Eddy Simulation and application to an analytical approach". MA thesis. RWTH Aachen, 2017.
- [V.L+98] Zimont V.L. et al. "An efficient computational model for premixed turbulent combustion at high reynolds numbers based on a turbulent flame speed closure". In: *ASME J. Eng. Gas Turbines and Power*, 120(3), pp. 526-532 (1998).
- [VM95] H. K. Versteeg and W. Malalasekera. *An introduction to Computational Fluid Dynamics*. Longman Scientific & Technical, 1995.
- [Vor] "Vortex Preservation Test". URL: <http://elearning.cerfacs.fr/numerical/benchmarks/vortex2d/index.php>.
- [Wer+06] Krebs Werner et al. "Thermoacoustic Design Tools and Passive Control: Siemens Power Generation Approaches". In: *Combustion Instabilities in Gas Turbine Engines* (2006).
- [WMD06] J. Warnatz, U. Maas, and R.W. Dibble. *Combustion*. Springer-Verlag Berlin Heidelberg, 2006.
- [ZL05] B.T. Zinn and Tim Lieuwen. "Combustion Instabilities: Basic Concepts". In: 210 (2005), pp. 3–26.
- [ZNB16] N. Zettervall and K. Nordin-Bates. "Large Eddy Simulation of a premixed bluff body stabilized flame using global and skeletal reaction mechanisms". In: *Combustion and Flame* 179. p.1-22 (2016).
- [ZYP14] F. Zhang, R. Yu, and X.S. Bai. "DNS of H<sub>2</sub>/air Combustion in a Constant Volume Enclosure Relevant to HCCI Engines". In: *Energy Procedia*, Vol 61, 2014 P.1536-1539 (2014).
- [Jue16] Juelich Supercomputing Centre. "JURECA: General-purpose supercomputer at Juelich Supercomputing Centre". In: *Journal of large-scale research facilities* 2.A62 (2016). DOI: [10.17815/jlsrf-2-121](https://doi.org/10.17815/jlsrf-2-121). URL: <http://dx.doi.org/10.17815/jlsrf-2-121>.